POLITECNICO DI TORINO

Politecnico di Torino

Master's Degree in Mechanical Engineering

Master's Degree Thesis

A study on non-linear effects during sine vibration testing of large deployable reflector antenna

Supervisors

Prof. Dario ANASTASIO

Prof. Stefano MARCHESIELLO

Dr. Davide PEDERBELLI (Large Space Structures GmbH)

Candidate

Giulio GRILLO

Academic Year 2024/2025 - July 2025

Ringraziamenti

Abstract

The objective of this thesis is to study the nonlinear effects that occur during vibration testing of large, deployable space antennas. Since traditional linear analysis methods are insufficient to describe these complex behaviors, the work focuses on quantifying how the structure's dynamic parameters, such as resonant frequency and damping, change as a function of vibration amplitude.

To achieve this, two advanced system identification techniques were used and compared:

- CONCERTO method
- Modified Dobson method

These methods were first validated on numerical models with known nonlinearities and on simpler experimental structures to verify their reliability.

Subsequently, the techniques were applied to experimental data from a qualification campaign conducted on LEOB (Large Deployable Reflector for Earth Observation). By analyzing the responses to different levels of sinusoidal excitation, it was possible to extract the amplitude-dependent modal parameters

The ultimate goal was to use this data to more accurately predict the frequency and amplitude shifts in the antenna's response. This predictive capability is critical for optimizing vibration tests, particularly "notching" strategies (the reduction of input at critical frequencies), ensuring the structure is tested safely without being damaged.
The predictive capability showed promising results, though with some limitations.

Table of Contents

List of Figures

1 Spaceborne Deployable Reflector Antennas

1.1 Introduction

To explore space, launching satellites with antennas is the first step [1]. Consequently, spaceborne antennas have become essential components in a wide range of satellite missions, for example:

- Communication
- Reconnaissance
- Navigation
- Remote sensing
- Deep-space exploration
- Radio astronomy

They act as the “eyes” and “ears” of satellite systems, playing a fundamental role in the successful execution of satellite operations.
To meet the demanding conditions of space applications, these antennas are generally required to possess four main characteristics:

- High precision to operate effectively at high frequencies
- Large diameter to achieve high signal gain
- Light weight
- High stowage ratio

Depending on their specific function and the current state of technological development in the aerospace industry, deployable antennas are typically categorized into three types:

- Reflector antennas
- Array antennas
- Microelectromechanical antennas

1.2 Status of spaceborne deployable reflector antennas

Reflector antennas are the most commonly employed type across a wide range of satellite applications. Based on the structural configuration of the reflector, these antennas can be further classified into four main categories:

- Rigid reflector antennas
- Inflatable reflector antennas
- Mesh reflector antennas
- Membrane reflector antennas

1.2.1 Rigid reflector antenna

This antenna type is distinguished by a reflective surface composed of a central hub and several rigid, curved panels.
These rigid deployable reflectors are typically fabricated from metal plates or carbon fiber reinforced plastic (CFRP) coated with a metallic reflective layer.

One of the primary advantages of this design lies in the ability to manufacture the panels into an accurate parabolic shape, resulting in a highly precise reflector surface. This high surface accuracy after deployment makes it particularly suitable for applications in the field of microwave remote sensing, such as microwave radiometers and scatterometers.

Nonetheless, this antenna type presents certain limitations, including a heavy structure, high costs and a large stowed volume.
As a result, it is now seldom used for large-diameter satellite antennas.

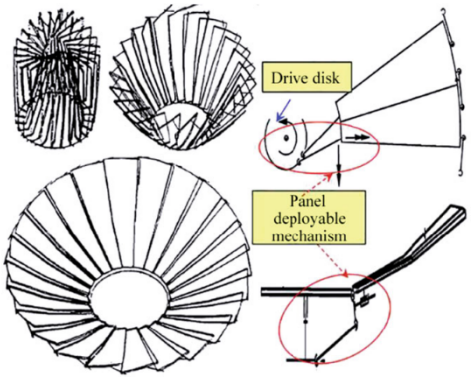

Figure 1.1: Petal type reflector antenna

1.2.2 Inflatable reflector antenna

Inflatable deployable antennas offer key advantages such as a high furled ratio and a large diameter. However, they also present notable drawbacks. The accuracy of the reflector surface is limited because a compressor, which adds to the system's overall areal density, needs to be carried into space. These antennas are typically constructed from flexible materials, such as Kevlar or Mylar membranes treated with chemical resin.

The deployment mechanism of inflatable antennas is similar to that of inflatable membranes employed in civil buildings. The structure is expanded into its intended shape and position through internal pressurization. However, unlike civilian applications, once the antenna is fully deployed, exposure to sunlight triggers a process that hardens the membrane material. This solidification allows the antenna to retain its deployed shape, even if internal pressure decreases due to gas leaks, ensuring the reflector surface maintains its accuracy over time.

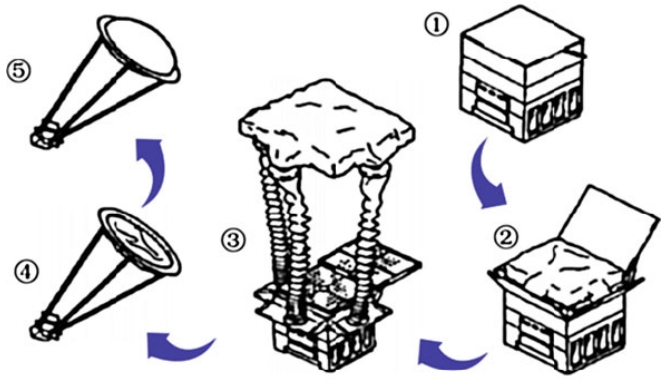

Figure 1.2: Deployment process of inflatable antenna

1.2.3 Mesh reflector antenna

Currently, mesh deployable antennas represent the primary choice for in-orbit large-scale deployable antennas. They are a major research focus of the international aerospace industry, encompassing theoretical studies, methodological development, and experimental validation. The defining feature of this antenna type is its reflector surface, which is made of a flexible wire mesh, classifying it as a flexible-force structure.

The position of the tensioning points and the level of tension applied to the supporting net play a crucial role in determining the mesh reflector's ability to conform to the desired shape, as well as its surface accuracy, smoothness and deployment reliability. Mesh reflectors are extremely lightweight and easy to fold, they have a high furled rate and can achieve large apertures with relative ease. They are also well-suited for integration with different types of deployable support structures. However, they do come with drawbacks, notably their structural complexity and lower performance in terms of precision, reliability, and repeatability of the reflector surface. Depending on the type of support structure used for the mesh and the deployment mechanism, mesh deployable antennas can take a various structural configuration.

1.2.3.1 Loop antenna

The loop antenna is a deployable structure that combines an unfolded truss system with a supporting cable-net. The truss can be arranged along the perimeter, at the center, or extend radially from the hub. This category of antennas includes several variants, such as the peripheral truss type, Harris ring and EGS loop antenna.

Figure 1.3: Loop mesh reflector antenna

1.2.3.2 Radial rib antenna

The radial rib antenna features an umbrella-like configuration, consisting of multiple parabolic carbon fiber tubular ribs extending from a central hub. A reflective mesh surface is stretched between the ribs, forming the antenna’s parabolic reflector.

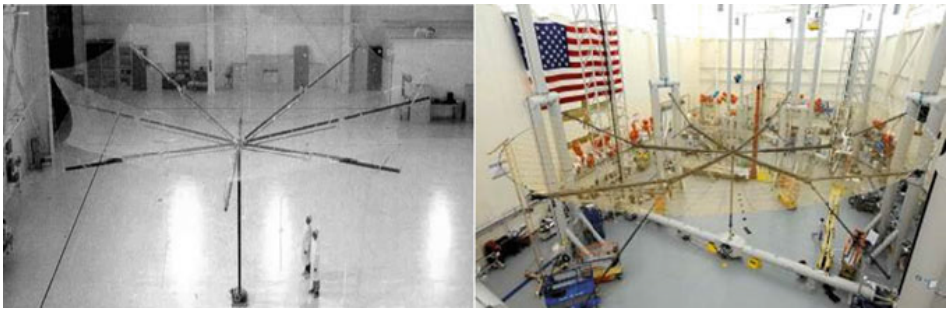

Figure 1.4: Radial rib antenna

1.2.3.3 Frame antenna

This antenna employs a modular design, typically composed of multiple tetrahedral or hexagonal prism-shaped modules. The overall diameter can be adjusted by varying the size and number of these modules, allowing for flexible adaptation to different mission requirements.

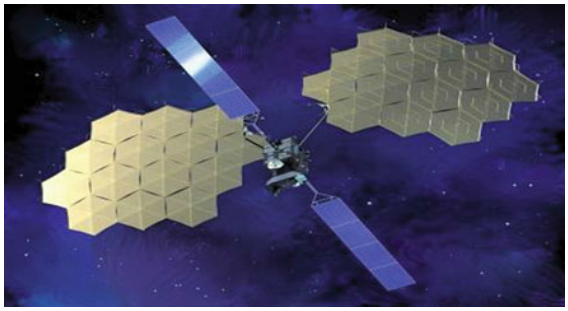

Figure 1.5: ETS-VIII frame antenna

1.2.3.4 Wrapping rib antenna

This antenna is another variation of the umbrella-type design, primarily composed of a central hub, parabolic radial ribs with a lenticular cross-section and a reflective mesh surface stretched across the structure.

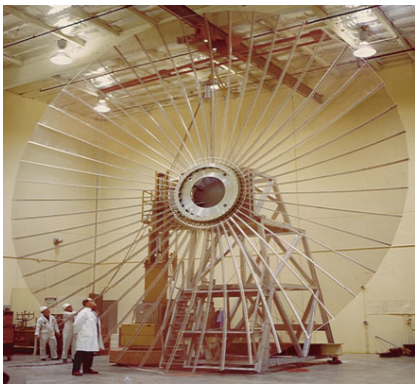

Figure 1.6: ATS-6 wrapping rib antenna

1.2.4 Electrostatic forming membrane reflector antenna

The membrane reflector is a recently developed antenna type.
It utilizes a polyimide membrane coated with a metallic reflective layer to reflect electromagnetic waves. To achieve and maintain the necessary surface precision, this design relies on a combination of skirt cable tension, internal gas pressure and electrostatic forces.

The membrane reflector antenna offers several advantages over traditional reflector designs, including high surface precision, ultra-lightweight construction, small furled volume and ease of folding and deployment.
It has attracted significant interest due to its low areal density and the capability to actively control the reflector shape by adjusting the electrostatic forces.

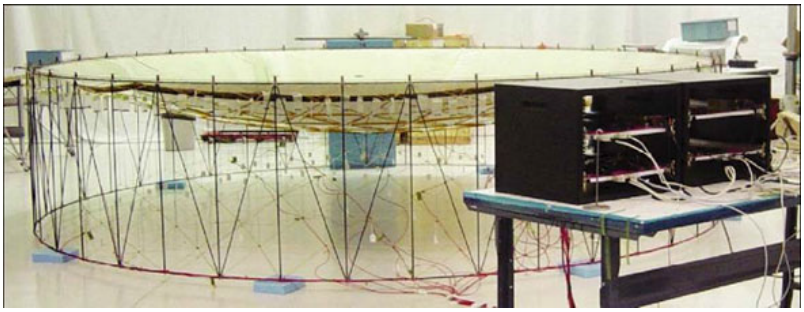

Figure 1.7: Electrostatic forming deployable membrane antenna

To provide a clear overview of the methods and technologies discussed above, the application ranges of the four main types of reflector antennas (rigid, membrane, mesh and inflatable) are illustrated in the Figure 1.8.

It can be seen from Figure 1.8 that the existing reflector antennas are mainly developed toward two goals: a larger scale and a higher precision.

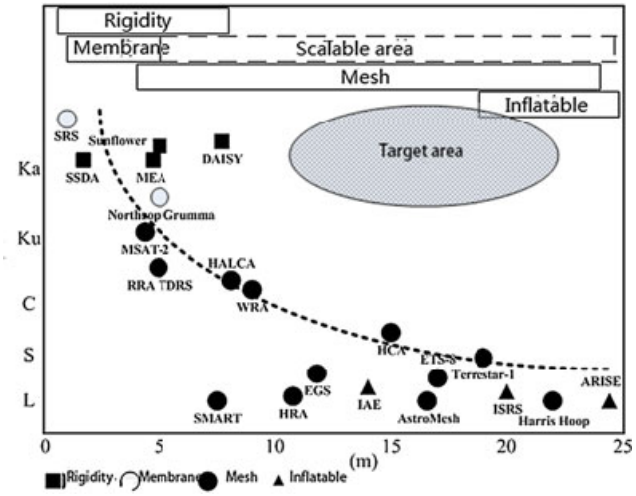

Figure 1.8: Application ranges for four types of reflector antennas

2 Loads analysis process

2.1 Introduction

The analysis of structural loads plays a crucial role in spacecraft development, aiming to ensure that the vehicle can safely endure all mission phases, from launch through in-orbit operation. This process involves identifying all relevant mechanical environments, both deterministic and random, and translating them into design loads.

Because structural loads are influenced by both the external environments and the evolving design of the spacecraft and launch vehicle, their estimation follows an iterative logic known as the "loads cycle" which involves:

- Building mathematical models of the structure
- Defining forcing functions and load factors representing critical environments
- Calculating design loads and displacements throughout all phases
- Assessing results to identify potential design changes or risks
- Updating the design or choosing to accept the associated risks

Spacecraft programs usually perform several load cycles, for: preliminary design, final design and final verification (which uses test correlated models). The main steps of a launch vehicle–payload load cycle analysis are shown in Figure 2.1

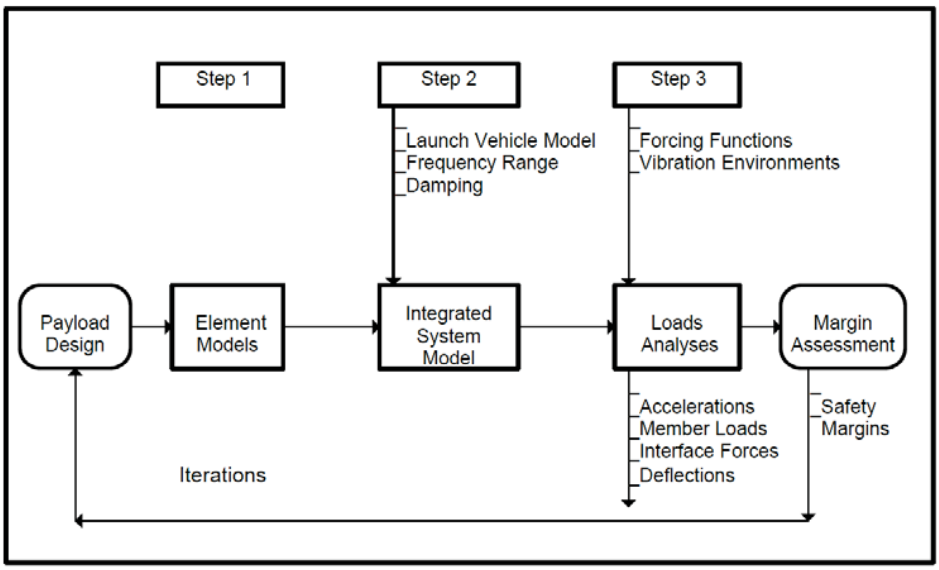

Figure 2.1: The Load Cycle Analysis Process

Since the prediction of dynamic environments and test criteria are influenced by modeling, which always carries a certain degree of inaccuracy, uncertainty factors are applied to the calculated loads.

This process is typically conducted across multiple levels of assembly: each hardware level is usually tested separately to ensure proper performance when integrated. However, the types of dynamic excitations of concern may vary between assembly levels and must be carefully evaluated for each stage. The application of safety factors follows a recursive logic, starting at the system level and cascading down.

2.2 Mechanical loads for design and verification

2.2.1 Spacecraft flight environments and dynamic loads

Launch is composed of multiple events, each involving several independent load sources that act on both the launch vehicle and the payload. The flight environments responsible for generating static and dynamic loads on spaceflight hardware are typically classified as follows:

- Static acceleration from constant or slowly varying external forces
- Low-frequency dynamic response (0–100 Hz, up to 150 Hz for small launchers) due to transient flight events affecting the launch vehicle/payload system
- High-frequency random vibration environment (20 Hz–2000 Hz) transmitted from the launch vehicle to the payload at interfaces between them
- High-frequency acoustic pressure environment (20 Hz–8000 Hz) inside the payload compartment
- Shock events with energy usually concentrated above 500 Hz and measured in the range of 100 Hz to 10 kHz

These loads can occur in combination at various stages throughout the flight. Once in orbit, the spacecraft's structural response to the micro-vibration environment can play a crucial role in verifying mission performance.

2.2.2 Vibration environments and frequency range

One of the main challenges in spacecraft structural analysis is that loads and responses occur across a wide frequency range, from low to high frequencies:

- Low frequency includes static conditions up to the first modes.
- High frequency refers to regions with high modal density and modal overlap.

This distinction is not absolute and depends on the characteristics of the structure. For small, stiff components, low frequency may reach hundreds of Hz, while for large satellites, frequencies above 100 Hz may be considered high.

Currently, no single structural analysis method can fully capture the behavior across the entire frequency range; Finite Element Models (FEM) predict structural behavior well at low frequencies, but accuracy decreases as frequency increases due to:

- Computational reasons: mesh resolution is often too coarse to capture short-wavelength deformations at high frequencies; Additionally, modal truncation introduces further errors
- Physical reasons: the response at high frequencies becomes highly sensitive to structural details, some of which are unavoidable manufacturing and assembly tolerances.

2.2.3 Introduction to analysis and test types

Mechanical environments, such as pressure, vibration, shock and thermal gradients, impose specific design requirements on many structural components, requiring extensive pre-flight testing to ensure hardware survivability. Qualification test environments are typically more severe than any flight condition and may drive the design.

The process starts by defining the maximum expected environments during launch and on-orbit operation and these are then cascaded from system to subsystem and component level to set design and test requirements.

While computational methods help predict dynamic behavior, environmental testing remains essential, especially for small structures where high-frequency effects are harder to model. The objectives of the system level testing are:

- Verify mechanical and electrical connections
- Measure structural responses and ensure that the test levels were adequate
- Ensure protection against unexpected phenomena
- Determine the dynamic contributions to the design inertia loads

Although often grouped with environmental tests, the sine vibration test is technically distinct. Its primary purpose is not to simulate a flight environment directly, but rather to verify structural strength by monitoring responses to controlled inputs, specifically to prevent overloads.

A final point to note is that dynamic environments affecting space vehicle hardware are typically multi-axial. While acoustic tests replicate this naturally, shock and vibration tests are often performed sequentially along single axes, which can be inaccurate.

2.2.4 Sine vibration test

Sine-wave excitations, such as swept-sine vibration tests, are commonly used for the qualification of spacecraft hardware, especially to simulate low-frequency transients. The main goal is to verify the strength of secondary structures and primary structures (if needed). However, this can lead to simultaneous undertest and overtest conditions.

Undertest refers to a situation where the test is not severe enough, potentially underestimating the actual damage the hardware might experience during real operating conditions. This typically happens because only one resonance is excited at a time, unlike real transients that excite multiple modes simultaneously.
Overtest, on the other hand, occurs when the test is too severe, potentially leading to an overestimation of the damage. This is usually caused by an excessive number of stress cycles applied to the hardware during the swept-sine test, a condition that can be mitigated by increasing the sweep rate.

Another source of overtesting is the difference in boundary conditions between test and flight. During a vibration test the item under investigation responds according to its “clamped” natural modes, rather than in the coupled modes that occur during actual flight conditions, since in that case the spacecraft is mounted on a flexible structure.
At certain frequencies, corresponding to the resonance frequencies of the test article when it is mounted on a rigid support (such as a shaker table), the acceleration at the interface between the mounting structure and the test article drops.

This phenomenon is known as the vibration absorber effect and leads to exaggerated amplification of input forces at the resonance frequencies of the test article.

To prevent this, the sine input spectrum must be notched at resonance frequencies. However, the notching criteria must not compromise the spacecraft flightworthiness. There are two types of notching:

- Primary notching: limits forces and moments at the launch vehicle/spacecraft interface to values matching the maximum axial and lateral quasi-static (QS) levels from the launcher manual.
- Secondary notching: limits the acceleration or loads at specific spacecraft locations, typically based on the qualification thresholds of subsystems or units.

2.2.5 Other types of tests

The preliminary structural design of a spacecraft is usually based on load factors provided in the launch vehicle user's manual: the Quasi-Static Loads, which represent the worst-case combinations of static and dynamic accelerations that may occur throughout the mission. Static tests are used to verify the strength of the spacecraft's primary structural elements.

Some load environments are considered random due to unpredictable forces, such as engine oscillations, buffeting, or sound pressure.
Random vibration tests check whether hardware can withstand the broad-band high frequency vibration environment. These tests are performed using shakers and are governed by a control system, which uses feedback from accelerometers to ensure a realistic and non-damaging response.

Acoustic pressure fluctuations under the fairing are caused by engine operation and aerodynamic effects during flight. Structures vibrate randomly in response to acoustics. Lightweight and large-area structures are most affected, while compact and heavy structures are less directly excited but can still vibrate due to coupling with other parts.
These vibrations especially affect electrical and electronic components.
Acoustic testing of spacecraft or major subsystems aims to reproduce the acoustic pressure conditions expected during lift-off and mission phases. Complex components susceptible to acoustic noise are tested prior to system integration in an acoustic chamber with high reverberation where loudspeakers or horns generate the acoustic field.

Shocks are a transient mechanical loading with a very short duration, high frequency content and accelerations, typically occurring during launch and early deployment phases.
Main sources of shock include launcher stages separation, fairing jettisoning, separation of the satellite from the launcher and deployment of appendages.
System level shock tests replicate mission events using actual shock sources or by using sophisticated pyro-shock generating systems. Unit-level shock tests are typically performed using various methods, most commonly by mounting the component on a fixture that is then subjected to an impact.

2.3 Basic principles, criteria and assumptions in structure and loads verification

2.3.1 Equivalence criteria for loads and environments

Acceleration is widely used to define the severity of the mechanical environments due to its direct link to forces and ease of measurement. Loads are typically expressed as:

- Equivalent accelerations at the center of gravity (CoG), for quasi-static loads
- Sine spectra, for low-frequency transients and harmonic loads
- Power spectral densities (PSD), for broad band random vibrations
- Shock response spectra (SRS), for shock loads

Duration is also a key factor as it influences potential damage and structural life.

The topic of equivalence criteria for dynamic environments is highly complex. In most cases the concept of "equivalence" is limited and may present certain drawbacks, therefore enveloping techniques and conservative assumptions are often applied. Determining equivalence between different environments or identifying the most critical one usually requires evaluating and comparing the anticipated structural responses.

2.3.2 Criteria for assessing verification loads

In analytical evaluations, safety margins must be greater than or equal to zero to ensure structural adequacy.

In the context of static or sinusoidal testing, the test loads or stresses are compared to the total predicted loads expected during the mission. This comparison serves as evidence that the applied test loads were sufficiently high, including qualification margins.

For acoustic or random vibration testing, the test environments are compared with random-vibration environments derived from system-level acoustic tests. This demonstrates that the random vibration test levels applied at lower levels of assembly were high enough and included appropriate qualification margins.

In shock testing, test environments are validated against shock environments derived from system-level shock testing, providing evidence that the applied shock levels at lower assembly levels were sufficiently severe, again including qualification margins.

3 System identification

3.1 Introduction

Inferring models from observations and studying their properties is really what science is about. The models may be of more or less formal character, but they have the basic feature that they attempt to link observations together into some pattern. System identification deals with the problem of building mathematical models of dynamical systems based on observed data from the system [2].

In a broad sense, a system is an object excited by external stimuli (inputs), in which variables interact and produce observable signals (outputs). External disturbances such as noise may also be present (measured or unmeasured).

Mathematical models may be developed along two routes:

- Modeling route: it consists in subdividing the system into subsystems whose properties are well understood from previous experience and then mathematically joining them to obtain a model of the complete system.
  The modeling procedure is highly application-dependent and doesn't necessarily involve experimentation on the actual system.
- System identification route (inverse problem): input and output signals from the system are recorded and subjected to data analysis in order to infer a model.

Identified models generally serve different purposes:

- Understanding: in this context, system identification is used as a tool to gain insights into the physical behavior of the system under investigation (white box and grey box models may be used).
- Prediction: the identified model is used to predict the system's behavior beyond the conditions represented in the training dataset, which often involves extrapolating the current understanding of the system to untested scenarios. Such extrapolation can be risky, especially when dealing with nonlinear systems.
- Control: the identified model is integrated into control strategies, usually within feedback loops (black box models are used).

3.2 Inverse problem procedure

The construction of a model from data involves three entities.

1) The data record
   Input and output data are often collected during a dedicated identification experiment, where the user can decide which signals to record as well as select the input signals to apply. The main goal of designing such an experiment is to make these choices in a way that maximizes the information content of the collected data, while also respecting any practical constraints that may exist.
   In other situations, the user might not have control over the experimental conditions and thus must rely on data collected during the normal operation of the system.

2) The set of models or the model structure
   This selection involves defining the collection of candidate models within which the most suitable one will be sought. This step is arguably the most critical and challenging part of the system identification process.
   It is here that prior knowledge, engineering intuition, and expertise must be combined with the formal properties of the models. In some cases, the model set is defined after careful modeling the physical interactions and phenomena of the system (white box). In other situations, standard linear models are used without any reference to the physical background and their parameters are used to fit the data (black box). There are also models that represent a compromise: the parameters remain adjustable but still retain physical meaning (gray box). Generally speaking, the model structure is a parametric mapping that relates past system inputs and outputs to the model output space:

$$\hat{y}(t|\theta) = g(\theta, Z^{t-1}) \tag{3.1}$$

   where θ is the finite-dimensional parameter vector used to parametrize the mapping.
3) Determining the "best" model in the set, guided by the data
   Selecting the most suitable model from the set is known as the identification method. Evaluating the quality; the techniques for this evaluation are generally addressed independently of the specific model structure chosen.

Once the previous three steps have been completed, a specific model is chosen: the one that best fits the data based on the selected criterion. The next step is to validate whether this model is adequate for its intended purpose. This evaluation is known as model validation. Model validation includes various procedures designed to assess how well the model aligns with the observed data, prior knowledge and the model's intended application. It is important to note that a model can never be accepted as the definitive and true representation of the system; at best, it should be considered an adequate description of certain specific aspects that are of particular interest.

As we've seen, the system identification process follows a logical sequence: first, data is collected; then a model set is chosen and finally, the "best" model within that set is selected. If the initial model fails the validation tests, it becomes necessary to revisit and revise the earlier steps of the procedure. There are several reasons why the model may be inadequate:

- The numerical method failed to find the best model according to the criterion.
- The chosen criterion was not appropriate.
- The selected model set was inadequate and did not include any model capable of providing a sufficiently good description of the system.
- The dataset lacked the necessary information to guide the selection of a good model.

A significant part of any identification task is dedicated to tackling these issues, especially the choice of an adequate model set, which is done through an iterative process guided by prior knowledge and the results of previous attempts.

In Figure 3.1 we can see a graphic visualization of this process, known as the system identification loop.

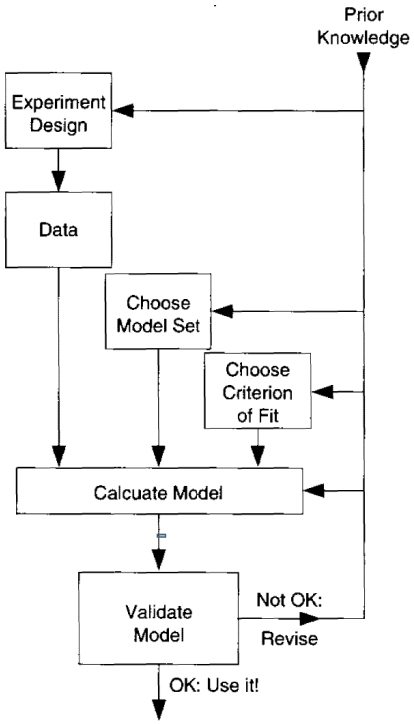

Figure 3.1: The system identification loop

3.3 From linear to nonlinear system identification

As stated in [3], the properties that characterize a linear system are:

- Principle of superposition: it is more than just a property of linear systems; in mathematical terms, it actually defines what is considered linear and what is not. The overall response of a linear structure to multiple simultaneous inputs can be determined by applying each input individually, recording the corresponding output and summing all the individual responses to obtain the total response.
- Homogeneity and invariance of the FRF: homogeneity represents a restricted form of the principle of superposition. It indicates that the system's response is independent of the input signal's magnitude: an input $\alpha x_1(t)$ always produces an output $\alpha y_1(t)$. If we pass to the frequency regime this implies that:

$$H(\omega) = \frac{\alpha Y(\omega)}{\alpha X(\omega)} = \frac{Y(\omega)}{X(\omega)} \tag{3.2}$$

  So, the FRF is invariant under changes of α or effectively of the level of excitation.
- Invariance of the modal parameters: modal parameters such as resonance frequencies, damping ratios, mode shapes are considered invariant, since the principle of superposition ensures that the system's dynamic characteristics remain unchanged with varying input amplitudes.
- Uniqueness of the solution: in a linear system, the response to a given excitation is unique and deterministic.

Many of the assumptions valid for linear structures or systems no longer hold in the presence of nonlinearity. In fact, all engineering structures exhibit some degree of nonlinearity, typically due to factors such as:

- Structural joints with looseness or friction characteristics
- Boundary conditions that impose variable stiffness constraints
- Materials with amplitude dependent properties
- Components such as shock absorbers, vibration isolators, bearings, linkages or actuators whose dynamics are input dependent.

There is no unique approach to dealing with the problem of nonlinearity either analytically or experimentally and thus, several approaches must often be tested to ascertain whether a structure can be classified as linear or nonlinear.

Kerschen et al. in [4] try to give a general overview on the different nonlinear system identification methods.

3.3.1 Modal methods

This section briefly introduces the modal approach, which is described extensively in [5]. The modal approach solves the equations of motion by exploiting the normal modes of a linear structure and the process is carried out in two main steps:

- Eigenvalue Problem: the undamped equations of motion are solved without considering external excitation, yielding the system's normal modes, which consists of eigenvalues and their associated eigenvectors, defined over the internal degrees of freedom.
- Mode Superposition: the complete equations of motion, including both damping and external excitation, are solved by summing the contribution of each mode.

Essentially, the modal approach projects the system's motion onto a basis of normal modes that are orthogonal, which imply implies that the equations of motion become uncoupled, allowing each mode to behave as an independent single degree of freedom system contributing individually to the total response.

This technique is a fundamental tool for structural dynamicists and remains unmatched for the analysis of linear systems. Unfortunately, the "linear" qualifier is significant [3]. Modal analysis is the quintessential linear theory, fundamentally dependent on the principle of superposition. However, this reliance poses a major limitation in today's context, where nonlinear effects are increasingly acknowledged as key contributors to the dynamic behaviour of systems and structures.

In general, the presence of nonlinearity has a rather destructive impact on modal analysis. All the system properties typically considered invariant in a linear system, such as resonant frequencies, damping ratios, mode shapes, and frequency response functions (FRFs), become dependent on the excitation level used during testing.

Since the fundamental aim of modal analysis is to describe systems based on these invariants, the best result achievable in the nonlinear case is a model that represents a linearization of the system, valid only for the specific level of excitation applied. Such a model, however, cannot accurately predict behavior under different excitation levels and therefore has limited practical value. Additionally, other properties unique to linear systems, such as reciprocity, are also lost in general nonlinear systems.

Another fundamental principle of modal analysis is decoupling or dimension reduction. By transforming the system from physical coordinates to normal or modal coordinates, a linear system with n degrees of freedom is converted into n independent Single-Degree-of-Freedom (SDOF) systems. However, this decoupling property no longer holds in the case of general nonlinear systems.

When faced with these limitations, a structural dynamicist has three primary approaches:

1) Preserve the philosophy and fundamental principles of modal analysis, while developing methods to characterize nonlinear systems by understanding how and where amplitude invariance breaks down.
2) Maintain the modal analysis framework but broaden the theory to include objects which are amplitude invariants of nonlinear systems.
3) Abandon the modal analysis approach entirely and instead pursue theoretical models specifically designed to handle nonlinear behavior directly.

4 Selected identification methods

This chapter focuses on selected methods for extracting equivalent modal parameters, namely natural frequency, damping ratio and modal constants, from Frequency Response Functions (FRFs) of weakly-nonlinear systems, which can be either transmissibilities or receptances.

These methods are based on the assumption that at a given response amplitude, the nonlinear system can be linearized, allowing for frequency-domain modal estimation techniques to be applied iteratively across different amplitude levels. This approach yields amplitude-dependent modal parameters, which can be useful for modeling and predicting the dynamic behavior of nonlinear structures.

Modal parameters could be extracted through level-controlled sinusoidal tests, where the excitation input is adjusted to maintain a constant response amplitude and then a linear modal analysis method can process the transfer functions. This procedure is repeated for various amplitude levels. However, implementing this approach can be quite challenging due to the difficulty in precisely controlling the input force to achieve a constant response amplitude. Moreover, it requires conducting a large number of tests. The identification techniques proposed here are based on different linearization strategies.

4.1 CONCERTO Method

COde for Nonlinear identifiCation from mEasured Response To vibratiOn (CONCERTO), described in [6], belongs to the class of Single-Degree-of-Freedom (SDOF) modal analysis methods, which can be applied either to SDOF systems or MDOF systems characterized by well - separated resonance peaks. In these cases the system's behavior near a resonance peak can be approximated by the mode corresponding to that resonance, while contributions from other modes are neglected. Therefore, physical coordinates and forces can be used instead of modal coordinates and forces.

No assumption is made regarding the types of nonlinearities involved. However, the nonlinearities must be weak enough to ensure the system's response remains synchronous with the input.

Since the system is assumed to behave linearly at a given displacement response amplitude, the modal parameters are further considered to be amplitude-dependent functions of the displacement response.

4.1.1 Receptance case

In a frequency range close to the resonance peak, the system can be approximated as a SDOF system with modal properties m_r, c_r, k_r, that represents modal mass, damping and stiffness, respectively. The modal mass is assumed to remain constant, while modal damping and stiffness are assumed to be function of the displacement amplitude $|X|$, thus yielding: $c_r = c_r(|X|), k_r = k_r(|X|)$.

A schematic representation of the system is shown in Figure 4.1.

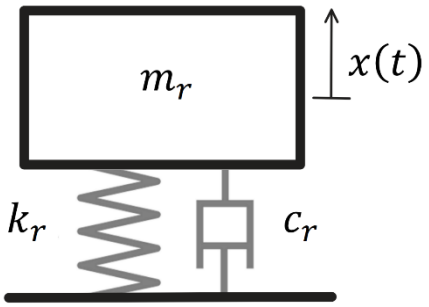

Figure 4.1: Scheme of the system - Receptance

The equation of motion of the system is:

$$m_r\ddot{x} + c_r(|X|)\dot{x} + k_r(|X|)x = F(t) \tag{4.1}$$

The exciting force is assumed to be sinusoidal:

$$F(t) = Fsin(\omega t) \tag{4.2}$$

The steady-state response is assumed to be harmonic at the same frequency ω:

$$x(t) = |X|sin(\omega t + \phi) = Xsin(\omega t) \tag{4.3}$$

This is an approximation, since in the case of nonlinear vibrations the response of the system could also contain harmonics and/or subharmonics of the excitation frequency.

Utilizing a complex notation, we can rewrite equations (4.2) and (4.3) as:

$$\begin{gathered} x(t) = Xe^{j\omega t}, \textit{ where: } X = |X|e^{j\phi} \\ F(t) = Fe^{j\omega t}, \textit{ where: } F = |F| \end{gathered} \tag{4.4}$$

Substituting (4.4) into (4.1), we obtain:

$$[-m_r\omega^2 + k_r(|X|) + jc_r(|X|)\omega]Xe^{j\omega t} = Fe^{j\omega t} \tag{4.5}$$

It is possible to define the receptance as:

$$H(\omega) = \frac{X}{F} = \frac{1}{-m_r\omega^2 + k_r(|X|) + jc_r(|X|)\omega} = \frac{1/m_r}{-\omega^2 + \frac{k_r(|X|)}{m_r} + \frac{jc_r(|X|)}{m_r}\omega} \tag{4.6}$$

We can rewrite $H(\omega)$ in terms of the amplitude-dependent natural frequency $\omega_r(|X|)$ and modal loss factor $\eta_r(|X|)$ or damping ratio $\zeta_r(|X|)$, which are defined as:

$$\begin{gathered} \omega_r^2(|X|) = \frac{k_r(|X|)}{m_r} \\ \frac{c_r(|X|)}{m_r} = 2\zeta_r(|X|)\omega_r(|X|) = \eta_r(|X|)\frac{\omega_r^2(|X|)}{\omega} \end{gathered} \tag{4.7}$$

Substituting (4.7) in (4.6), we get the following formulations for receptance:

– For the hysteretic damping model:

$$H(\omega) = \frac{1/m_r}{-\omega^2 + \omega_r^2(|X|) + j\eta_r(|X|)\omega_r^2(|X|)} \tag{4.8}$$

– For the viscous damping model:

$$H(\omega) = \frac{1/m_r}{-\omega^2 + \omega_r^2(|X|) + j2\zeta_r(|X|)\omega_r(|X|)\omega} \tag{4.9}$$

The natural frequency $\omega_r(|X|)$ and modal loss factor $\eta_r(|X|)$ or damping ratio $\zeta_r(|X|)$ relative to a particular vibration amplitude are extracted with the following procedure.

The key idea is to pick two frequency points ω_1 and ω_2 located on either side of the resonance peak, such that the system exhibits the same response amplitude $|X|$ at both frequencies.
In practice, the measured data points typically do not exhibit identical response amplitudes and therefore it is necessary to interpolate the response curve in order to obtain a set of frequency points on either side of the resonance with equal amplitude.

4.1.1.1 Hysteretic damping case

If we consider the receptance at two points with the same $|X|$:

$$\begin{aligned} H(\omega_1) &= \frac{1/m_r}{\omega_r^2 - \omega_1^2 + j\eta_r\omega_r^2} = R_1 + jI_1 \\ H(\omega_2) &= \frac{1/m_r}{\omega_r^2 - \omega_2^2 + j\eta_r\omega_r^2} = R_2 + jI_2 \end{aligned} \tag{4.10}$$

The selected points can be visualized in the Figure 4.2:

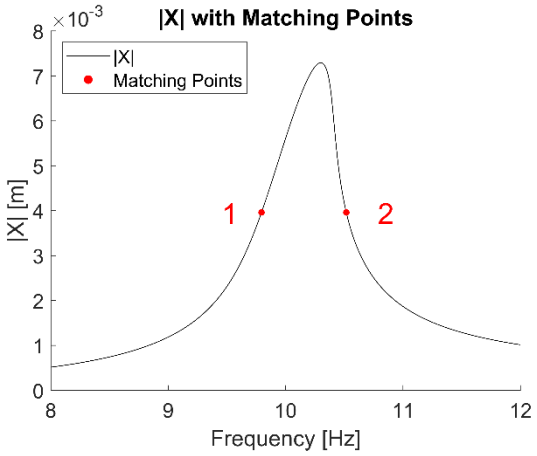

Figure 4.2: Equal displacement amplitude points

By equating the numerators of (4.10), we obtain:

$$(R_1 + jI_1)(\omega_r^2 - \omega_1^2 + j\eta_r\omega_r^2) = (R_2 + jI_2)(\omega_r^2 - \omega_2^2 + j\eta_r\omega_r^2) \tag{4.11}$$

Expanding the products of (4.11):

$$[R_1(\omega_r^2 - \omega_1^2) - I_1\eta_r\omega_r^2] + j[R_1\eta_r\omega_r^2 + I_1(\omega_r^2 - \omega_1^2)] = \\ [R_2(\omega_r^2 - \omega_2^2) - I_2\eta_r\omega_r^2] + j[R_2\eta_r\omega_r^2 + I_2(\omega_r^2 - \omega_2^2)] \quad (4.12)$$

By equating the real part and imaginary parts of (4.12):

$$\begin{cases} R_1(\omega_r^2 - \omega_1^2) - I_1\eta_r\omega_r^2 = R_2(\omega_r^2 - \omega_2^2) - I_2\eta_r\omega_r^2 \\ R_1\eta_r\omega_r^2 + I_1(\omega_r^2 - \omega_1^2) = R_2\eta_r\omega_r^2 + I_2(\omega_r^2 - \omega_2^2) \end{cases} \quad (4.13)$$

Rewriting (4.13):

$$\begin{cases} R_1(\omega_r^2 - \omega_1^2) - R_2(\omega_r^2 - \omega_2^2) = (I_1 - I_2)\eta_r\omega_r^2 \\ (R_1 - R_2)\eta_r\omega_r^2 = I_2(\omega_r^2 - \omega_2^2) - I_1(\omega_r^2 - \omega_1^2) \end{cases} \quad (4.14)$$

Solving for the term $\eta_r\omega_r^2$:

$$\eta_r\omega_r^2 = \frac{R_1(\omega_r^2 - \omega_1^2) - R_2(\omega_r^2 - \omega_2^2)}{I_1 - I_2} = \frac{I_2(\omega_r^2 - \omega_2^2) - I_1(\omega_r^2 - \omega_1^2)}{R_1 - R_2} \quad (4.15)$$

By reworking (4.15):

$$[R_1(\omega_r^2 - \omega_1^2) - R_2(\omega_r^2 - \omega_2^2)](R_1 - R_2) = [I_2(\omega_r^2 - \omega_2^2) - I_1(\omega_r^2 - \omega_1^2)](I_1 - I_2) \quad (4.16)$$

Expanding the products of (4.16):

$$R_1^2(\omega_r^2 - \omega_1^2) - R_1R_2(\omega_r^2 - \omega_2^2) - R_1R_2(\omega_r^2 - \omega_1^2) + R_2^2(\omega_r^2 - \omega_2^2) = \\ I_1I_2(\omega_r^2 - \omega_2^2) - I_1^2(\omega_r^2 - \omega_1^2) - I_2^2(\omega_r^2 - \omega_2^2) + I_1I_2(\omega_r^2 - \omega_1^2) \quad (4.17)$$

Bringing all the terms to the left-hand side:

$$(R_1^2 - R_1R_2 + I_1^2 - I_1I_2)(\omega_r^2 - \omega_1^2) + (R_2^2 - R_1R_2 + I_2^2 - I_1I_2)(\omega_r^2 - \omega_2^2) = 0 \quad (4.18)$$

Leaving only the terms related to ω_r^2 to the left-hand side:

$$(R_1^2 + I_1^2 + R_2^2 + I_2^2 - 2R_1R_2 - 2I_1I_2)\omega_r^2 = \\ = (R_1^2 - R_1R_2 + I_1^2 - I_1I_2)\omega_1^2 + (R_2^2 - R_1R_2 + I_2^2 - I_1I_2)\omega_2^2 \quad (4.19)$$

Solving for ω_r^2:

$$\omega_r^2 = \frac{(R_1^2 - R_1R_2 + I_1^2 - I_1I_2)\omega_1^2 + (R_2^2 - R_1R_2 + I_2^2 - I_1I_2)\omega_2^2}{(R_1^2 + I_1^2 + R_2^2 + I_2^2 - 2R_1R_2 - 2I_1I_2)} \quad (4.20)$$

Rewriting the denominator of (4.20):

$$(R_1^2 + I_1^2 + R_2^2 + I_2^2 - 2R_1R_2 - 2I_1I_2) = (R_2 - R_1)^2 + (I_2 - I_1)^2 \quad (4.21)$$

Rewriting the numerator of (4.20):

$$(R_1^2 - R_1R_2 + I_1^2 - I_1I_2)\omega_1^2 + (R_2^2 - R_1R_2 + I_2^2 - I_1I_2)\omega_2^2 = \\ = (R_2 - R_1)(R_2\omega_2^2 - R_1\omega_1^2) + (I_2 - I_1)(I_2\omega_2^2 - I_1\omega_1^2) \quad (4.22)$$

We finally get the expression of ω_r^2:

$$\omega_r^2(|X|) = \frac{(R_2 - R_1)(R_2\omega_2^2 - R_1\omega_1^2) + (I_2 - I_1)(I_2\omega_2^2 - I_1\omega_1^2)}{(R_2 - R_1)^2 + (I_2 - I_1)^2} \tag{4.23}$$

Recalling the equation (4.15), we can write:

$$\eta_r\omega_r^2(I_1 - I_2) = R_1(\omega_r^2 - \omega_1^2) - R_2(\omega_r^2 - \omega_2^2) \tag{4.24}$$

By reworking (4.24):

$$\eta_r\omega_r^2(I_1 - I_2) = R_2\omega_2^2 - R_1\omega_1^2 - (R_2 - R_1)\omega_r^2 \tag{4.25}$$

By substituting in (4.25) the expression (4.23):

$$\eta_r\omega_r^2(I_1 - I_2) = R_2\omega_2^2 - R_1\omega_1^2 - \frac{(R_2-R_1)^2(R_2\omega_2^2-R_1\omega_1^2)+(R_2-R_1)(I_2-I_1)(I_2\omega_2^2-I_1\omega_1^2)}{(R_2-R_1)^2+(I_2-I_1)^2} \tag{4.26}$$

By reworking (4.26):

$$\eta_r\omega_r^2 = \frac{-(I_2 - I_1)(R_2\omega_2^2 - R_1\omega_1^2) + (R_2 - R_1)(I_2\omega_2^2 - I_1\omega_1^2)}{(R_2 - R_1)^2 + (I_2 - I_1)^2} \tag{4.27}$$

We finally obtain the expression η_r:

$$\eta_r(|X|) = \frac{-(I_2 - I_1)(R_2\omega_2^2 - R_1\omega_1^2) + (R_2 - R_1)(I_2\omega_2^2 - I_1\omega_1^2)}{\omega_r^2[(R_2 - R_1)^2 + (I_2 - I_1)^2]} \tag{4.28}$$

4.1.1.2 Viscous damping case

If we consider the receptance at two points with the same $|X|$:

$$\begin{aligned} H(\omega_1) &= \frac{1/m_r}{\omega_r^2 - \omega_1^2 + j2\zeta_r\omega_r\omega} = R_1 + jI_1 \\ H(\omega_2) &= \frac{1/m_r}{\omega_r^2 - \omega_2^2 + j2\zeta_r\omega_r\omega} = R_2 + jI_2 \end{aligned} \tag{4.29}$$

By equating the numerators of (4.29), we obtain:

$$(R_1 + jI_1)(\omega_r^2 - \omega_1^2 + j2\zeta_r\omega_1\omega_r) = (R_2 + jI_2)(\omega_r^2 - \omega_2^2 + j2\zeta_r\omega_2\omega_r) \tag{4.30}$$

Expanding the products of (4.30):

$$\begin{aligned} &[R_1(\omega_r^2 - \omega_1^2) - I_1 2\zeta_r\omega_1\omega_r] + j[R_1 2\zeta_r\omega_2\omega_r + I_1(\omega_r^2 - \omega_1^2)] = \\ &[R_2(\omega_r^2 - \omega_2^2) - I_2 2\zeta_r\omega_2\omega_r] + j[R_2 2\zeta_r\omega_2\omega_r + I_2(\omega_r^2 - \omega_2^2)] \end{aligned} \tag{4.31}$$

By equating the real part and imaginary parts of (4.31):

$$\begin{cases} R_1(\omega_r^2 - \omega_1^2) - I_1 2\zeta_r\omega_1\omega_r = R_2(\omega_r^2 - \omega_2^2) - I_2 2\zeta_r\omega_2\omega_r \\ R_1 2\zeta_r\omega_1\omega_r + I_1(\omega_r^2 - \omega_1^2) = R_2 2\zeta_r\omega_2\omega_r + I_2(\omega_r^2 - \omega_2^2) \end{cases} \tag{4.32}$$

Rewriting (4.32):

$$\begin{cases} R_1(\omega_r^2 - \omega_1^2) - R_2(\omega_r^2 - \omega_2^2) = (I_1\omega_1 - I_2\omega_2)2\zeta_r\omega_r \\ (R_1\omega_1 - R_2\omega_2)2\zeta_r\omega_r = I_2(\omega_r^2 - \omega_2^2) - I_1(\omega_r^2 - \omega_1^2) \end{cases} \tag{4.33}$$

Solving for the term $2\zeta_r\omega_r$:

$$2\zeta_r\omega_r = \frac{R_1(\omega_r^2 - \omega_1^2) - R_2(\omega_r^2 - \omega_2^2)}{I_1\omega_1 - I_2\omega_2} = \frac{I_2(\omega_r^2 - \omega_2^2) - I_1(\omega_r^2 - \omega_1^2)}{R_1\omega_1 - R_2\omega_2} \tag{4.34}$$

By reworking (4.34):

$$\begin{gathered} [R_1(\omega_r^2 - \omega_1^2) - R_2(\omega_r^2 - \omega_2^2)](R_1\omega_1 - R_2\omega_2) = \\ = [I_2(\omega_r^2 - \omega_2^2) - I_1(\omega_r^2 - \omega_1^2)](I_1\omega_1 - I_2\omega_2) \end{gathered} \tag{4.35}$$

Expanding the products of (4.35):

$$\begin{gathered} R_1^2\omega_1(\omega_r^2 - \omega_1^2) - R_1R_2\omega_1(\omega_r^2 - \omega_2^2) - R_1R_2\omega_2(\omega_r^2 - \omega_1^2) + R_2^2\omega_2(\omega_r^2 - \omega_2^2) = \\ = I_1I_2\omega_1(\omega_r^2 - \omega_2^2) - I_1^2\omega_1(\omega_r^2 - \omega_1^2) - I_2^2\omega_2(\omega_r^2 - \omega_2^2) + I_1I_2\omega_2(\omega_r^2 - \omega_1^2) \end{gathered} \tag{4.36}$$

Bringing all the terms to the left-hand side:

$$\begin{gathered} (R_1^2\omega_1 - R_1R_2\omega_2 + I_1^2\omega_1 - I_1I_2\omega_2)(\omega_r^2 - \omega_1^2) + \\ +(R_2^2\omega_2 - R_1R_2\omega_1 + I_2^2\omega_2 - I_1I_2\omega_1)(\omega_r^2 - \omega_2^2) = 0 \end{gathered} \tag{4.37}$$

Leving only the terms related to ω_r^2 to the left-hand side:

$$\begin{gathered} (R_1^2\omega_1 + I_1^2\omega_1 + R_2^2\omega_2 + I_2^2\omega_2 - R_1R_2\omega_1 - R_1R_2\omega_2 - I_1I_2\omega_1 - I_1I_2\omega_2)\omega_r^2 = \\ = (R_1^2\omega_1 - R_1R_2\omega_2 + I_1^2\omega_1 - I_1I_2\omega_2)\omega_1^2 + (R_2^2\omega_2 - R_1R_2\omega_1 + I_2^2\omega_2 - I_1I_2\omega_1)\omega_2^2 \end{gathered} \tag{4.38}$$

Solving for ω_r^2:

$$\omega_r^2(|X|) = \frac{(R_1^2\omega_1 - R_1R_2\omega_2 + I_1^2\omega_1 - I_1I_2\omega_2)\omega_1^2 + (R_2^2\omega_2 - R_1R_2\omega_1 + I_2^2\omega_2 - I_1I_2\omega_1)\omega_2^2}{R_1^2\omega_1 + I_1^2\omega_1 + R_2^2\omega_2 + I_2^2\omega_2 - R_1R_2(\omega_1 + \omega_2) - I_1I_2(\omega_1 + \omega_2)} \tag{4.39}$$

Rewriting the denominator of (4.39)

$$\begin{gathered} R_1^2\omega_1 + I_1^2\omega_1 + R_2^2\omega_2 + I_2^2\omega_2 - R_1R_2(\omega_1 + \omega_2) - I_1I_2(\omega_1 + \omega_2) = \\ = (R_1^2 - R_1R_2 + I_1^2 - I_1I_2)\omega_1 + (R_2^2 - R_1R_2 + I_2^2 - I_1I_2)\omega_2 \end{gathered} \tag{4.40}$$

We finally get the expression of ω_r^2:

$$\omega_r^2(|X|) = \frac{(R_1^2\omega_1 - R_1R_2\omega_2 + I_1^2\omega_1 - I_1I_2\omega_2)\omega_1^2 + (R_2^2\omega_2 - R_1R_2\omega_1 + I_2^2\omega_2 - I_1I_2\omega_1)\omega_2^2}{(R_1^2 - R_1R_2 + I_1^2 - I_1I_2)\omega_1 + (R_2^2 - R_1R_2 + I_2^2 - I_1I_2)\omega_2} \tag{4.41}$$

Recalling the equation (4.34):

$$2\zeta_r\omega_r = \frac{R_1(\omega_r^2 - \omega_1^2) - R_2(\omega_r^2 - \omega_2^2)}{I_1\omega_1 - I_2\omega_2} \tag{4.42}$$

We finally obtain the expression ζ_r:

$$\zeta_r(|X|) = \frac{R_1(\omega_r^2 - \omega_1^2) - R_2(\omega_r^2 - \omega_2^2)}{2\omega_r(I_1\omega_1 - I_2\omega_2)} \tag{4.43}$$

The modal parameters $\omega_r^2(|X|)$ and $\eta(|X|)$ or $\zeta(|X|)$ can be converted into modal stiffness $k(|X|)$ and modal damping $c(|X|)$ functions, using:

- The modal mass, which is calculated interpolating the real part of the inverse of the receptance function with a second degree polynomial:

$$H^{-1}(\omega) = k_r - m_r\omega^2 + jc_r\omega \tag{4.44}$$

- The relationships between the modal stiffness, modal damping, the natural frequency and the loss factor (or damping ratio):

$$\begin{aligned} k_r(|X|) &= \omega_r^2(|X|)m_r \\ c_r(|X|) &= 2\zeta_r(|X|)m_r\omega_r(|X|) \\ c_r(|X|) &= \eta_r(|X|)m_r\frac{\omega_r^2(|X|)}{\omega} \simeq \eta_r(|X|)m\omega_r(|X|) \end{aligned} \tag{4.45}$$

4.1.2 Transmissibility case

In many practical applications, structures are tested through base excitation, which leads to the measurement of transmissibilities instead of receptances. If the transmissibility of the system is known instead of its receptance, the CONCERTO method can still be applied, with some modifications as described in [7].

Compared to the receptance case, the main limitation is that the modal mass cannot be determined, as it cannot be computed from the inverse of the transmissibility. As a consequence, the modal stiffness and modal damping cannot be evaluated. Only the modal frequency and the modal loss factor (or modal damping ratio) can be extracted.

In [6] and [7], the adopted approach is based on a SDOF approximation. Under this assumption, the transmissibility can be expressed as:

$$T(\omega) = \frac{\omega_r^2 + j\eta_r\omega_r^2}{\omega_r^2 - \omega^2 + j\eta_r\omega_r^2} \tag{4.46}$$

One of the objectives of this work was to predict the system response in terms of transmissibility under different loading conditions, by employing a method (described later) to reconstruct the nonlinear transmissibility. In this context, it is essential to extract not only the modal frequency and modal damping, but also the modal constant.

In the case of SDOF approximation, the modal constant is given by:

$$A_r + iB_r = \omega_r^2 + j\eta_r\omega_r^2 \tag{4.47}$$

So, the modal constant depends only on the modal properties.

It is evident that applying this method to a more complex system would result in a rough approximation of the modal constant, as the influence of the mode shapes is neglected. For this reason, a more general formulation is required.

To begin, we examine the behavior of a two degree of freedom (2DOF) system subjected to base excitation.

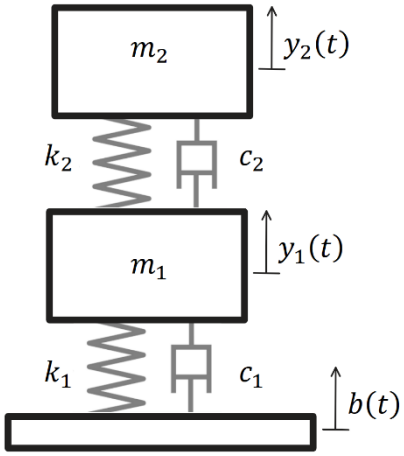

Figure 4.3: Scheme of a 2DOFs system - Transmissibility

Using either a Newtonian or energy-based approach, the equations of motion for the system can be derived as:

$$\begin{bmatrix} m_1 & 0 \\ 0 & m_2 \end{bmatrix}\begin{pmatrix} \ddot{y}_1 \\ \ddot{y}_2 \end{pmatrix} + \begin{bmatrix} c_1 + c_2 & -c_2 \\ -c_2 & c_2 \end{bmatrix}\begin{pmatrix} \dot{y}_1 \\ \dot{y}_2 \end{pmatrix} + \begin{bmatrix} k_1 + k_2 & -k_2 \\ -k_2 & k_2 \end{bmatrix}\begin{pmatrix} y_1 \\ y_2 \end{pmatrix} = \begin{pmatrix} c_1\dot{b} + k_1 b \\ 0 \end{pmatrix} \quad (4.48)$$

In a more compact form, (4.48) can be written as:

$$[m](\ddot{y}) + [c](\dot{y}) + [k](y) = \begin{pmatrix} c_1\dot{b} + k_1 b \\ 0 \end{pmatrix} \quad (4.49)$$

Applying the modal transformation and pre-multiplying (4.49) by the modal matrix yields:

$$[\Psi]^T[m][\Psi](\ddot{\eta}) + [\Psi]^T[c][\Psi](\dot{\eta}) + [\Psi]^T[k]\Psi](\eta) = [\Psi]^T\begin{pmatrix} c_1\dot{b} + k_1 b \\ 0 \end{pmatrix} \quad (4.50)$$

Equation (4.50) leads to the following expression:

$$[M_r](\ddot{\eta}) + [C_r](\dot{\eta}) + [K_r](\eta) = [\Psi]^T\begin{pmatrix} c_1\dot{b} + k_1 b \\ 0 \end{pmatrix} \quad (4.51)$$

Given that the system is subjected to base excitation with a sinusoidal input:

$$\begin{aligned} (b) &= (B_0)e^{i\omega t} \\ (\eta) &= (\eta_0)e^{i\omega t} \end{aligned} \quad (4.52)$$

By substituting (4.52) in the (4.51), we obtain

$$(-\omega^2[M_r] + i\omega[C_r] + [K_r])(\eta_0) = [\Psi]^T\begin{pmatrix} c_1 i\omega B_0 + k_1 B_0 \\ 0 \end{pmatrix} = [\Psi]^T\begin{pmatrix} c_1 i\omega + k_1 \\ 0 \end{pmatrix} B_0 \quad (4.53)$$

Returning to physical coordinates:

$$(Y_0) = \sum_{r=1}^{n} \frac{(\psi_r)^T \begin{pmatrix} c_1 i\omega + k_1 \\ 0 \end{pmatrix} B_0 (\psi_r)}{k_r - \omega^2 m_r + i\omega c_r} \tag{4.54}$$

Expanding the modal vectors explicitly

$$(Y_0) = \sum_{r=1}^{n} \frac{(\psi_{1r}\ \psi_{2r})^T \begin{pmatrix} c_1 i\omega + k_1 \\ 0 \end{pmatrix} B_0 \begin{pmatrix} \psi_{1r} \\ \psi_{2r} \end{pmatrix}}{k_r - \omega^2 m_r + i\omega c_r} \tag{4.55}$$

Carrying out the calculations:

$$(Y_0) = \sum_{r=1}^{n} \frac{B_0 \begin{pmatrix} \psi_{1r}(c_1 i\omega + k_1)\psi_{1r} \\ \psi_{1r}(c_1 i\omega + k_1)\psi_{2r} \end{pmatrix}}{k_r - \omega^2 m_r + i\omega c_r} \tag{4.56}$$

Expressing the individual components explicitly:

$$\begin{aligned} Y_{10} &= \sum_{r=1}^{n} \frac{B_0 \psi_{1r}(c_1 i\omega + k_1)\psi_{1r}}{k_r - \omega^2 m_r + i\omega c_r} \\ Y_{20} &= \sum_{r=1}^{n} \frac{B_0 \psi_{1r}(c_1 i\omega + k_1)\psi_{2r}}{k_r - \omega^2 m_r + i\omega c_r} \end{aligned} \tag{4.57}$$

The transmissibilities related to the two DOFs can be written as:

$$\begin{aligned} T_1(\omega) &= \frac{Y_{10}}{B_0} = \sum_{r=1}^{n} \frac{\psi_{1r}(c_1 i\omega + k_1)\psi_{1r}}{k_r - \omega^2 m_r + i\omega c_r} = \sum_{r=1}^{n} \frac{\phi_{1r}(c_1 i\omega + k_1)\phi_{1r}}{\omega_r^2 - \omega^2 + \frac{i\omega c_r}{m_r}} \\ T_2(\omega) &= \frac{Y_{20}}{B_0} = \sum_{r=1}^{n} \frac{\psi_{1r}(c_1 i\omega + k_1)\psi_{2r}}{k_r - \omega^2 m_r + i\omega c_r} = \sum_{r=1}^{n} \frac{\phi_{1r}(c_1 i\omega + k_1)\phi_{2r}}{\omega_r^2 - \omega^2 + \frac{i\omega c_r}{m_r}} \end{aligned} \tag{4.58}$$

Where c_1 can be expressed as:

- For the hysteretic damping model:

$$c_1 = \frac{\eta_1 k_1}{\omega} \tag{4.59}$$

  In this case, the term $c_1\omega$ is constant
- For the viscous damping model:

$$c_1 = 2\zeta_1 m \omega_r \tag{4.60}$$

  In this case, the term $c_1\omega$ is dependent by ω

If we consider a generic multi degree of freedom (MDOF) nonlinear system and neglect the contributions from all modes except the dominant one, the transmissibility for a generic DOF with respect to the base motion can be expressed as:

– For the hysteretic damping model:

$$T(\omega) = \frac{A_r(|Y-B|) + iB_r(|Y-B|)}{\omega_r^2(|Y-B|) - \omega^2 + i\eta_r(|Y-B|)\omega_r^2(|Y-B|)} \tag{4.61}$$

– For the viscous damping model:

$$T(\omega) = \frac{A_r(|Y-B|) + iB_{r,n}(|Y-B|)\omega}{\omega_r^2(|Y-B|) - \omega^2 + i2\zeta_r(|Y-B|)\omega_r(|Y-B|)\omega} \tag{4.62}$$

Where $B_{r,n}$ is the imaginary part of the modal constant normalized by the frequency.

The resulting formulations are more general than the one presented in [7]. While only a single mode is still considered, the modal constant is not directly computed from the modal properties.

4.1.2.1 Hysteretic damping case

If we consider the transmissibility at two points with the same $|Y-B|$:

$$\begin{aligned} T(\omega_1) &= \frac{A_r + iB_r}{\omega_r^2 - \omega_1^2 + j\eta_r\omega_r^2} = R_1 + jI_1 \\ T(\omega_2) &= \frac{A_r + iB_r}{\omega_r^2 - \omega_2^2 + j\eta_r\omega_r^2} = R_2 + jI_2 \end{aligned} \tag{4.63}$$

The selected points can be visualized in the Figure 4.4.

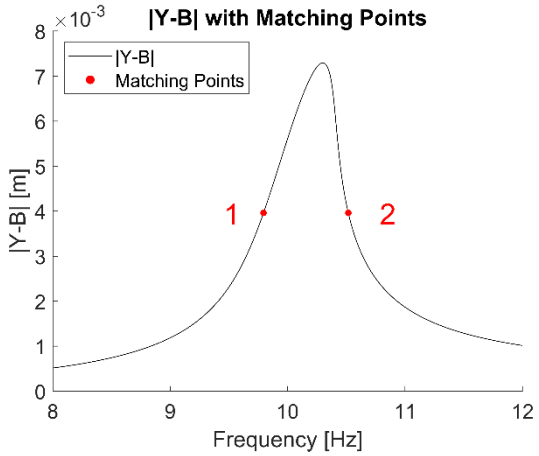

Figure 4.4: Equal displacement amplitude points

By equating the numerators of (4.63), we obtain:

$$(R_1 + jI_1)(\omega_r^2 - \omega_1^2 + j\eta_r\omega_r^2) = (R_2 + jI_2)(\omega_r^2 - \omega_2^2 + j\eta_r\omega_r^2) \tag{4.64}$$

From this point onward, the derivation follows the same steps as in the receptance case. The resulting formulations are identical, with the only difference being that R and I now refer to the real and imaginary parts of the transmissibility.

We therefore obtain:

$$\omega_r^2(|Y-B|) = \frac{(R_2-R_1)(R_2\omega_2^2 - R_1\omega_1^2) + (I_2-I_1)(I_2\omega_2^2 - I_1\omega_1^2)}{(R_2-R_1)^2 + (I_2-I_1)^2}$$
$$\eta_r(|Y-B|) = \frac{-(I_2-I_1)(R_2\omega_2^2 - R_1\omega_1^2) + (R_2-R_1)(I_2\omega_2^2 - I_1\omega_1^2)}{\omega_r^2[(R_2-R_1)^2 + (I_2-I_1)^2]} \quad (4.65)$$
$$A_r(|Y-B|) = R_1(\omega_r^2 - \omega_1^2) - I_1\eta_r\omega_r^2 = R_2(\omega_r^2 - \omega_2^2) - I_2\eta_r\omega_r^2$$
$$B_r(|Y-B|) = I_1(\omega_r^2 - \omega_1^2) + R_1\eta_r\omega_r^2 = I_2(\omega_r^2 - \omega_2^2) + R_2\eta_r\omega_r^2$$

4.1.2.2 Viscous damping case

If we consider the transmissibility at two points with the same $|Y-B|$:

$$T(\omega_1) = \frac{A_r + iB_{r,n}\omega_1}{\omega_r^2 - \omega_1^2 + j2\zeta_r\omega_r\omega_1} = R_1 + jI_1$$
$$T(\omega_2) = \frac{A_r + iB_{r,n}\omega_2}{\omega_r^2 - \omega_2^2 + j2\zeta_r\omega_r\omega_2} = R_2 + jI_2 \quad (4.66)$$

By multiplying the denominators of (4.66) with the complex value of the transmissibilities:

$$A_r + iB_{r,n}\omega_1 = (R_1 + jI_1)(\omega_r^2 - \omega_1^2 + j2\zeta_r\omega_r\omega_1)$$
$$A_r + iB_{r,n}\omega_2 = (R_2 + jI_2)(\omega_r^2 - \omega_2^2 + j2\zeta_r\omega_r\omega_2) \quad (4.67)$$

We get the expression of A_r and $B_{r,n}$:

$$A_r(|Y-B|) = R_1(\omega_r^2 - \omega_1^2) - I_1 2\zeta_r\omega_1\omega_r = R_2(\omega_r^2 - \omega_2^2) - I_2 2\zeta_r\omega_2\omega_r$$
$$B_{r,n}(|Y-B|) = \frac{R_1 2\zeta_r\omega_1\omega_r + I_1(\omega_r^2 - \omega_1^2)}{\omega_1} = \frac{R_2 2\zeta_r\omega_2\omega_r + I_2(\omega_r^2 - \omega_2^2)}{\omega_2} \quad (4.68)$$

By equating the different expressions of A_r and $B_{r,n}$:

$$\begin{cases} R_1(\omega_r^2 - \omega_1^2) - I_1 2\zeta_r\omega_1\omega_r = R_2(\omega_r^2 - \omega_2^2) - I_2 2\zeta_r\omega_2\omega_r \\ R_1\dfrac{\omega_2}{\omega_1}2\zeta_r\omega_1\omega_r + I_1\dfrac{\omega_2}{\omega_1}(\omega_r^2 - \omega_1^2) = R_2 2\zeta_r\omega_2\omega_r + I_2(\omega_r^2 - \omega_2^2) \end{cases} \quad (4.69)$$

Rewriting the expressions:

$$\begin{cases} R_1(\omega_r^2 - \omega_1^2) - R_2(\omega_r^2 - \omega_2^2) = (I_1\omega_1 - I_2\omega_2)2\zeta_r\omega_r \\ \left(R_1\dfrac{\omega_2}{\omega_1}\omega_1 - R_2\omega_2\right)2\zeta_r\omega_r = I_2(\omega_r^2 - \omega_2^2) - I_1\dfrac{\omega_2}{\omega_1}(\omega_r^2 - \omega_1^2) \end{cases} \quad (4.70)$$

Solving for the $2\zeta_r\omega_r$:

$$2\zeta_r\omega_r = \frac{R_1(\omega_r^2 - \omega_1^2) - R_2(\omega_r^2 - \omega_2^2)}{I_1\omega_1 - I_2\omega_2} = \frac{I_2(\omega_r^2 - \omega_2^2) - I_1\frac{\omega_2}{\omega_1}(\omega_r^2 - \omega_1^2)}{R_1\frac{\omega_2}{\omega_1}\omega_1 - R_2\omega_2} \quad (4.71)$$

Reworking (4.71):

$$\begin{aligned}&[R_1(\omega_r^2-\omega_1^2)-R_2(\omega_r^2-\omega_2^2)](R_1\omega_2-R_2\omega_2)=\\&=\left[I_2(\omega_r^2-\omega_2^2)-I_1\frac{\omega_2}{\omega_1}(\omega_r^2-\omega_1^2)\right](I_1\omega_1-I_2\omega_2)\end{aligned}\tag{4.72}$$

Expanding the products of (4.72):

$$\begin{aligned}&R_1^2\omega_2(\omega_r^2-\omega_1^2)-R_1\omega_2R_2(\omega_r^2-\omega_2^2)-R_1R_2\omega_2(\omega_r^2-\omega_1^2)+R_2^2\omega_2(\omega_r^2-\omega_2^2)\\&=I_1I_2\omega_1(\omega_r^2-\omega_2^2)-I_1^2\omega_2(\omega_r^2-\omega_1^2)-I_2^2\omega_2(\omega_r^2-\omega_2^2)+I_1I_2\frac{\omega_2^2}{\omega_1}(\omega_r^2-\omega_1^2)\end{aligned}\tag{4.73}$$

Bringing all the terms to the left-hand side:

$$\begin{aligned}&\left(R_1^2\omega_2-R_1R_2\omega_2+I_1^2\omega_2-I_1I_2\frac{\omega_2^2}{\omega_1}\right)(\omega_r^2-\omega_1^2)\\&+(R_2^2\omega_2-R_1\omega_2R_2+I_2^2\omega_2-I_1I_2\omega_1)(\omega_r^2-\omega_2^2)=0\end{aligned}\tag{4.74}$$

Leaving only the terms related to ω_r^2 to the left-hand side:

$$\begin{aligned}&\left(R_1^2\omega_2+I_1^2\omega_2+R_2^2\omega_2+I_2^2\omega_2-R_1\omega_2R_2-R_1R_2\omega_2-I_1I_2\omega_1-I_1I_2\frac{\omega_2^2}{\omega_1}\right)\omega_r^2=\\&\left(R_1^2\omega_2-R_1R_2\omega_2+I_1^2\omega_2-I_1I_2\frac{\omega_2^2}{\omega_1}\right)\omega_1^2+(R_2^2\omega_2-R_1\omega_2R_2+I_2^2\omega_2-I_1I_2\omega_1)\omega_2^2\end{aligned}\tag{4.75}$$

We finally obtain the expression of ω_r^2:

$$\omega_r^2(|Y-B|)=\frac{\left(R_1^2\omega_2-R_1R_2\omega_2+I_1^2\omega_2-I_1I_2\frac{\omega_2^2}{\omega_1}\right)\omega_1^2+(R_2^2\omega_2-R_1R_2\omega_2+I_2^2\omega_2-I_1I_2\omega_1)\omega_2^2}{R_1^2\omega_2+I_1^2\omega_2+R_2^2\omega_2+I_2^2\omega_2-2R_1R_2\omega_2-I_1I_2\omega_1-I_1I_2\frac{\omega_2^2}{\omega_1}}\tag{4.76}$$

Recalling the equation (4.71):

$$2\zeta_r\omega_r=\frac{R_1(\omega_r^2-\omega_1^2)-R_2(\omega_r^2-\omega_2^2)}{I_1\omega_1-I_2\omega_2}\tag{4.77}$$

We finally obtain the expression of ζ_r:

$$\zeta_r(|Y-B|)=\frac{R_1(\omega_r^2-\omega_1^2)-R_2(\omega_r^2-\omega_2^2)}{2\omega_r(I_1\omega_1-I_2\omega_2)}\tag{4.78}$$

4.2 Modified-Dobson method

The extraction method described in [8] falls within the category of Single-Degree-of-Freedom (SDOF) modal analysis techniques. It is based on the line-fit method using Dobson's formulation, originally developed for linear systems.

A Frequency Response Function (FRF), either transmissibility or receptance, can be represented either as the sum of contributions from N modes or, alternatively, as a single dominant mode r with an added constant residual term.
In the case of hysteretic damping, the FRF can be expressed as:

$$FRF(\omega) = \sum_{r=1}^{N} \frac{rA_{ij}}{\omega_r^2 - \omega^2 + i\eta_r\omega_r^2} = \frac{rA_{ij}}{\omega_r^2 - \omega^2 + i\eta_r\omega_r^2} + residual \tag{4.79}$$

$$rA_{ij} = A_r + iB_r$$

The Dobson method introduces a new parameter: the pseudo drive frequency Ω, which is used to create a pseudo frequency response function $FRF_{ij}(\Omega)$ near the resonance. To isolate the contribution of mode r and account for the residual effects on the response, two transfer functions are subtracted, resulting in:

$$FRF(\omega) - FRF(\Omega) = \frac{A_r + iB_r}{\omega_r^2 - \omega^2 + i\eta_r\omega_r^2} - \frac{A_r + iB_r}{\omega_r^2 - \Omega^2 + i\eta_r\omega_r^2} \tag{4.80}$$

Equation (4.80) can be rewritten as:

$$FRF(\omega) - FRF(\Omega) = (A_r + iB_r)\left[\frac{\omega^2 - \Omega^2}{(\omega_r^2 - \omega^2)(\omega_r^2 - \Omega^2) - \eta_r^2\omega_r^4 + i\eta_r\omega_r^2(2\omega_r^2 - \omega^2 - \Omega^2)}\right] \tag{4.81}$$

We can define the delta function as:

$$\Delta(\omega) = \frac{\omega^2 - \Omega^2}{FRF(\omega) - FRF(\Omega)} \tag{4.82}$$

By working on equation (4.82), we obtain:

$$\Delta(\omega) = \frac{A_r - iB_r}{A_r^2 + B_r^2}[(\omega_r^2 - \omega^2)(\omega_r^2 - \Omega^2) - \eta_r^2\omega_r^4 + i\eta_r\omega_r^2(2\omega_r^2 - \omega^2 - \Omega^2)] \tag{4.83}$$

The "fixing" frequency Ω is swept across the entire drive frequency vector ω, generating a square matrix $[\Delta]$ of values, where zeroes on the diagonal must be excluded.

The next step involves separating the real and imaginary parts of the delta function and plotting them against the squared frequency ω^2 as described by the following equations:

$$\begin{aligned} Re(\Delta) &= \frac{A_r}{A_r^2 + B_r^2}[(\omega_r^2 - \omega^2)(\omega_r^2 - \Omega^2) - \eta_r^2\omega_r^4] + \frac{B_r}{A_r^2 + B_r^2}[\eta_r\omega_r^2(2\omega_r^2 - \omega^2 - \Omega^2)] \\ Im(\Delta) &= \frac{A_r}{A_r^2 + B_r^2}[\eta_r\omega_r^2(2\omega_r^2 - \omega^2 - \Omega^2)] - \frac{B_r}{A_r^2 + B_r^2}[(\omega_r^2 - \omega^2)(\omega_r^2 - \Omega^2) - \eta_r^2\omega_r^4] \end{aligned} \tag{4.84}$$

The real and imaginary components of $\Delta(\omega)$ can be expressed as quadratic functions of ω:

$$\begin{aligned} Re\big(\Delta(\omega)\big) &= m_R\omega^2 + c_R \\ Im\big(\Delta(\omega)\big) &= m_I\omega^2 + c_I \end{aligned} \tag{4.85}$$

To obtain the coefficients m_R and m_I, (4.84) and (4.85) are equated:

$$\begin{aligned} m_R &= -\frac{1}{A_r^2 + B_r^2}[A_r(\omega_r^2 - \Omega^2) + B_r\eta_r\omega_r^2] \\ m_I &= \frac{1}{A_r^2 + B_r^2}[B_r(\omega_r^2 - \Omega^2) - A_r\eta_r\omega_r^2] \end{aligned} \tag{4.86}$$

The coefficients m_R and m_I in (4.86) can be expressed as quadratic functions of Ω:

$$\begin{aligned} m_R &= n_R\Omega^2 + d_R \\ m_I &= n_I\Omega^2 + d_I \end{aligned} \tag{4.87}$$

The obtain coefficients in (4.87) are obtained by equating (4.86) and (4.87):

$$\begin{aligned} n_R &= \frac{A_r}{A_r^2 + B_r^2} \\ d_R &= -\frac{(A_r + B_r\eta_r)\omega_r^2}{A_r^2 + B_r^2} \\ n_I &= -\frac{B_r}{A_r^2 + B_r^2} \\ d_I &= -\frac{(A_r\eta_r - B_r)\omega_r^2}{A_r^2 + B_r^2} \end{aligned} \tag{4.88}$$

Finally, the constants derived from (4.88) can be used to extract the four modal parameters: $\omega_r^2, \eta_r, A_r, B_r$. As previously discussed, these modal parameters are a function of the displacement amplitude $|Z|$, where:

- $|Z| = |X|$ in the case of receptances
- $|Z| = |Y - B|$ in the case of trasmissibilities

From the first and third equations of (4.88), we obtain:

$$A_r^2 + B_r^2 = \frac{1}{n_R^2 + n_I^2} \tag{4.89}$$

By substituting Equation (4.89) into the first equation of (4.88), we derive:

$$A_r(|Z|) = \frac{n_R}{n_R^2 + n_I^2} \tag{4.90}$$

By substituting Equation (4.89) into the third equation of (4.88), we obtain:

$$B_r(|Z|) = -\frac{n_I}{n_R^2 + n_I^2} \tag{4.91}$$

Using the second and fourth equations of (4.88), we derive:

$$\eta_r = \frac{d_I A_r + d_R B_r}{d_R A_r - d_I B_r} \tag{4.92}$$

By substituting (4.90) and (4.91) into (4.92), we obtain:

$$\eta_r(|Z|) = \frac{d_I n_R - d_R n_I}{d_R n_R + d_I n_I} \tag{4.92}$$

Finally, substituting (4.92) into either the second or fourth equation of (4.88), we derive:

$$\omega_r^2(|Z|) = -\frac{d_R n_R + d_I n_I}{n_R^2 + n_I^2} \tag{4.93}$$

If we want to obtain the damping ratio, we can use the following approximation:

$$\zeta(|Z|) \approx \frac{\eta}{2} \tag{4.94}$$

The discussion now transitions to the Modified-Dobson method, which extends the applicability of the Dobson method to nonlinear systems.

One can think of a nonlinear FRF that originates from an underlying linear response, becoming increasingly nonlinear as the Nyquist circle is swept and then progressively more linear again as the origin is approached.

Two frequency points, referred to as fixers, are selected at the lowest amplitude of the FRF, where the system response can be assumed to be linear. A third point, known as the sweeper, is chosen at a desired amplitude of the receptance, forming a triplet of frequency points. This triplet defines a Nyquist circle that represents an equivalent linear system for the selected receptance amplitude, as illustrated in Figure 4.5.

By applying the Dobson method to the triplet, the four modal parameters $\omega_r^2, \eta_r, A_r, B_r$ can be extracted. By sweeping the third frequency between the two reference points of the FRF, it's possible to track how the modal parameters transition from linear to nonlinear vibrations. Essentially, this process deconstructs a nonlinear FRF into a sequence of linear ones, each associated with different amplitude levels. In Figure 4.5 we can see the transmissibility of a linearized system corresponding to a certain displacement amplitude.

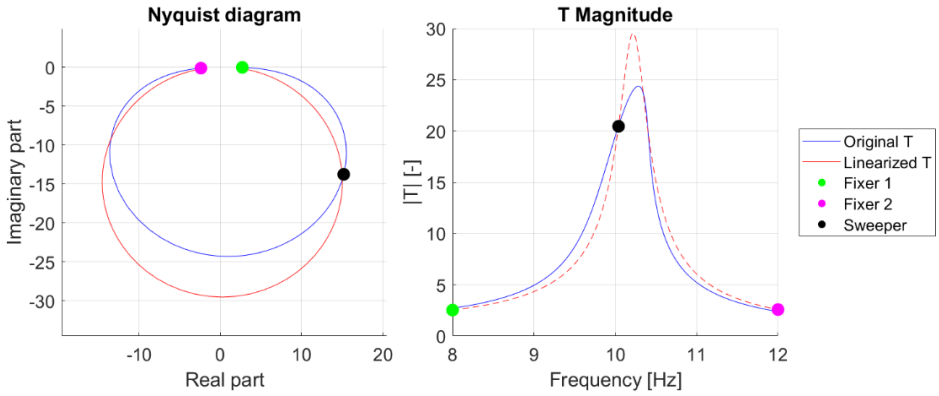

Figure 4.5: Nyquist Diagram and T magnitude of the equivalent linear system

The Modified-Dobson method is effective for resonances that are well-separated, as (4.80) eliminates residuals from neighbouring modes. However, it becomes less reliable as modes converge, due to two primary challenges. First, the fixers are chosen at an amplitude associated with linear vibrations, but as the modes get closer, the likelihood of including nonlinear residuals at the reference points increases. Second, the sweeper traverses the frequency range between the fixers, thus incorporating varying residuals with each iteration.

5 Validation

This chapter focuses on verifying the proposed methods by applying them to both simulated and experimental reference systems, before proceeding to the deployable reflector data. Initial tests are carried out on single and two-degree-of-freedom systems with known types of nonlinearities to evaluate consistency and accuracy. Experimental validation follows.

To this end, two approaches are employed:

- Analytical expressions for equivalent stiffness and damping are compared with the values extracted from the numerical systems.
- The New Method (NM) is used to reconstruct the nonlinear FRFs and compare them with the original ones. This approach is applied in the case of experimental systems.

5.1 Analytical stiffness and damping functions

The goal is to derive expressions for the parameters $k_{r,eq}$ and $c_{r,eq}$, which represent equivalent stiffness and damping coefficients that account for both linear and nonlinear contributions. These parameters appear in the equation of motion as follows:

$$m\ddot{x} + c_{eq}(|X|)\dot{x} + k_{eq}(|X|)x = Fsin(\omega t) \tag{5.1}$$

In this formulation, the system is excited by an external force. If, instead, the excitation is applied at the base, the proposed expressions remain valid, but the absolute coordinate must be replaced with the relative one.

The parameters are derived using the first-order approximation of the Harmonic Balance (HB) method.

5.1.1 Cubic stiffness and quadratic damping case

We consider an SDOF system governed by the following equation of motion:

$$m\ddot{x} + c\dot{x} + c_{nl}|\dot{x}|\dot{x} + kx + k_{nl}x^3 = Fsin(\omega t) \tag{5.2}$$

We assume the response to be harmonic at the excitation frequency ω:

$$x = |X|sin(\omega t + \phi) = Xsin(\omega t) \tag{5.3}$$

This leads to:

$$x^3 = \big(|X|sin(\omega t + \phi)\big)^3 = |X|^3 sin^3(\omega t + \phi) \tag{5.4}$$

Using the trigonometric identity:

$$sin^3(\omega t + \phi) = \frac{3}{4}sin(\omega t + \phi) - \frac{1}{4}sin\big(3(\omega t + \phi)\big) \tag{5.5}$$

Substituting (5.5) into (5.4) and approximating to the first harmonic, we obtain:

$$x^3 = |X|^3\left[\frac{3}{4}sin(\omega t + \phi) - \frac{1}{4}sin\big(3(\omega t + \phi)\big)\right] \cong \frac{3}{4}|X|^3 sin(\omega t + \phi) \tag{5.6}$$

The cubic stiffness term then becomes:

$$k_{nl}x^3 \cong k_{nl}\frac{3}{4}|X|^3 sin(\omega t+\phi) = \left(\frac{3}{4}k_{nl}|X|^2\right)x \tag{5.7}$$

Therefore, the total stiffness contribution is:

$$kx + k_{nl}x^3 \cong kx + \left(\frac{3}{4}k_{nl}|X|^2\right)x \cong \left(k + \frac{3}{4}k_{nl}|X|^2\right)x \tag{5.8}$$

Recalling (5.1), we finally obtain:

$$k_{eq}(|X|) \cong k + \frac{3}{4}k_{nl}|X|^2 \tag{5.9}$$

We can express the velocity as:

$$\dot{x} = |X|\omega cos(\omega t+\phi) \tag{5.10}$$

This leads to:

$$|\dot{x}|\dot{x} = |X|^2\omega^2|cos(\omega t+\phi)|cos(\omega t+\phi) \tag{5.11}$$

Expanding the product $|cos(\omega t+\phi)|cos(\omega t+\phi)$ into a Fourier series:

$$|cos(\omega t+\phi)|cos(\omega t+\phi) = \sum_{n=0}^{\infty}[a_n\, cos(n\theta) + b_n sin(n\theta)] \tag{5.12}$$

Approximating the product with its first harmonic:

$$|cos(\omega t+\phi)|cos(\omega t+\phi) \cong \frac{8}{3\pi}cos(\omega t+\phi) \tag{5.13}$$

Substituting (5.13) into (5.11), we obtain:

$$|\dot{x}|\dot{x} \cong |X|^2\omega^2\left(\frac{8}{3\pi}cos(\omega t)\right) \tag{5.14}$$

The quadratic damping term then becomes:

$$c_{nl}|\dot{x}|\dot{x} \cong c_{nl}|X|X\omega^2\left(\frac{8}{3\pi}cos(\omega t)\right) = \frac{8}{3\pi}c_{nl}|X|\omega\dot{x} \tag{5.15}$$

Therefore, the total damping contribution is:

$$c\dot{x} + c_{nl}|\dot{x}|\dot{x} \cong c\dot{x} + \frac{8}{3\pi}c_{nl}|X|\omega\dot{x} \cong \left(c + \frac{8}{3\pi}c_{nl}|X|\omega\right)\dot{x} \tag{5.16}$$

Recalling (5.1), we finally obtain:

$$c_{eq}(|X|) \cong c + \frac{8}{3\pi}c_{nl}|X|\omega \cong c + \frac{8}{3\pi}c_{nl}|X|\omega_r \tag{5.17}$$

5.1.2 Coulomb damping case

We consider an SDOF system governed by the following equation of motion:

$$m\ddot{x} + c\dot{x} + F_f sign(\dot{x}) + kx = Fsin(\omega t) \tag{5.18}$$

To derive c_{eq}, we equate the energy dissipated per cycle by the Coulomb friction force to the energy dissipated per cycle by an equivalent viscous damping force.

The energy dissipated per cycle due to Coulomb damping is given by:

$$E_{F_f} = F_f \int_0^T |\dot{x}| dt \tag{5.19}$$

We know that:

$$|\dot{x}| = |X|\omega|cos(\omega t + \phi)| \tag{5.20}$$

Substituting (5.20) into (5.19), we obtain:

$$E_{F_f} = F_f|X|\omega \int_0^T |cos(\omega t + \phi)| dt = F_f|X|\omega \frac{4}{\omega} = 4F_f|X| \tag{5.21}$$

The energy dissipated per cycle by the equivalent viscous damping force is given by:

$$E_d = c_{eq} \int_0^T \dot{x}(t)^2 dt \tag{5.22}$$

We know that:

$$\dot{x}(t)^2 = |X|^2\omega^2\, cos^2(\omega t + \phi) \tag{5.23}$$

Substituting (5.23) into (5.22), we obtain:

$$E_d = c_{eq}|X|^2\omega^2 \int_0^T cos^2(\omega t + \phi)\, dt = c_{eq}|X|^2\omega^2 \frac{\pi}{\omega} = c_{eq}|X|^2\omega\pi \tag{5.24}$$

Equating (5.21) and (5.24) yields:

$$4F_f|X| = c_{eq}|X|^2\omega\pi \tag{5.25}$$

Solving for $c_{r,eq}\dot{x}$:

$$c_{eq}\dot{x} = \frac{4F_f}{|X|\omega\pi}\dot{x} \tag{5.26}$$

Including the linear damping term, we get the final expression:

$$c_{eq} = c + \frac{4F_f}{|X|\omega\pi} \cong c + \frac{4F_f}{|X|\omega_r\pi} \tag{5.27}$$

5.2 New Method (NM)

This method, described in [8], can be used to generate a nonlinear FRF from a series of linear FRFs, each characterized by a specific displacement amplitude $|Z|$:

- $|Z| = |X|$ in the case of receptances
- $|Z| = |Y - B|$ in the case of transmissibilities

Once the modal parameters have been evaluated as a function of the displacement amplitude $|Z|$, they can be fitted using a polynomial function.

$$\begin{aligned} \omega_r(|Z|) &= \omega_n|Z|^n + \cdots + \omega_1|Z| + \omega_0 \\ \eta_r(|Z|) &= \eta_n|Z|^n + \cdots + \eta_1|Z| + \eta_0 \\ A_r(|Z|) &= A_n|Z|^n + \cdots + A_1|Z| + A_0 \\ B_r(|Z|) &= B_n|Z|^n + \cdots + B_1|Z| + B_0 \end{aligned} \tag{5.28}$$

The subscript r refers to the r-th mode, which is the predominant mode at the frequency span considered in the analysis.
The degree of the polynomial functions n should be chosen appropriately.

These functions can be used to generate the experimental nonlinear Frequency Response Surface (FRS), which can be expressed as:

$$FRF(\omega, |Z|) = \frac{A_r(|Z|) + iB_r(|Z|)}{\omega_r^2(|Z|) - \omega^2 + i\eta_r(|Z|)\omega_r^2(|Z|)} \tag{5.29}$$

The nonlinear FRF is obtained by intersecting the FRS with:

- A force plane relative to the input force if the case of receptances
- A displacement plane relative to the input displacement at the base if the case of transmissibilities

An example in the case of transmissibilities is shown in Figure 5.1.

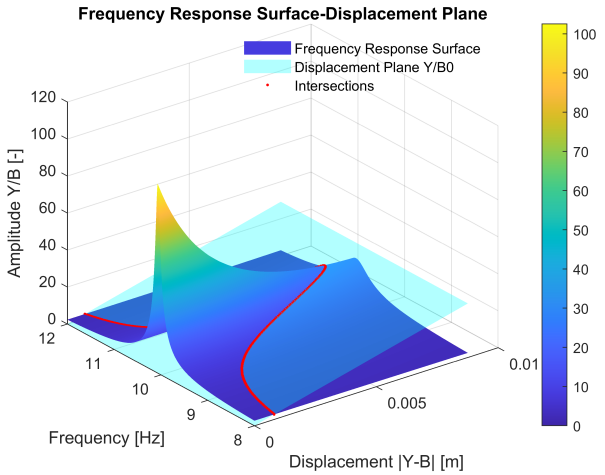

Figure 5.1: Intersection between the FRS and the Displacement Plane

5.3 Validation with numerical data

To assess the effectiveness of the nonlinear identification methods, CONCERTO and Modified Dobson, they are applied to numerical data generated from simulated systems. These systems are designed to exhibit distinct types of structural nonlinearities commonly encountered in practice. Specifically, the following cases are analyzed:

- Cubic stiffness nonlinearity
- Quadratic damping nonlinearity
- Coulomb damping

For each configuration, frequency response data is computed numerically and analyzed using both identification methods. The results obtained are subsequently compared to reference solutions computed analytically using the Harmonic Balance (HB) method. This comparison provides a benchmark to validate the accuracy and robustness of the proposed identification approach in the presence of different nonlinear effects.

It is important to note that, although transmissibilities were used instead of receptances in this validation phase, it was still possible to extract the equivalent stiffness and damping functions since the mass of the system is known a priori in the numerical simulations. As a result, the nonlinear stiffness and damping functions can be extracted and compared to the analytical reference solutions.

To further validate their applicability in realistic scenarios, additive noise was introduced into the time-domain simulation data.
This allowed the assessment of the robustness of both methods when processing noisy signals, reflecting conditions similar to those encountered in experimental measurements.

5.3.1 SDOF - Cubic stiffness and quadratic damping – Results

The system under investigation is a Single-Degree-of-Freedom (SDOF) system with base excitation, governed by the following equation of motion:

$$m\ddot{y} + c(\dot{y} - \dot{b}) + c_{nl}(\dot{y} - \dot{b})|\dot{y} - \dot{b}| + k(y - b) + k_{nl}(y - b)^3 = 0 \qquad (5.30)$$

Where y represents the absolute displacement, while b represents the base motion. Figure 5.2 presents the results obtained using CONCERTO, comparing them with the corresponding analytical values.
The comparison confirms the high accuracy of the method overall; however, the damping function shows a higher relative error at lower displacement levels.

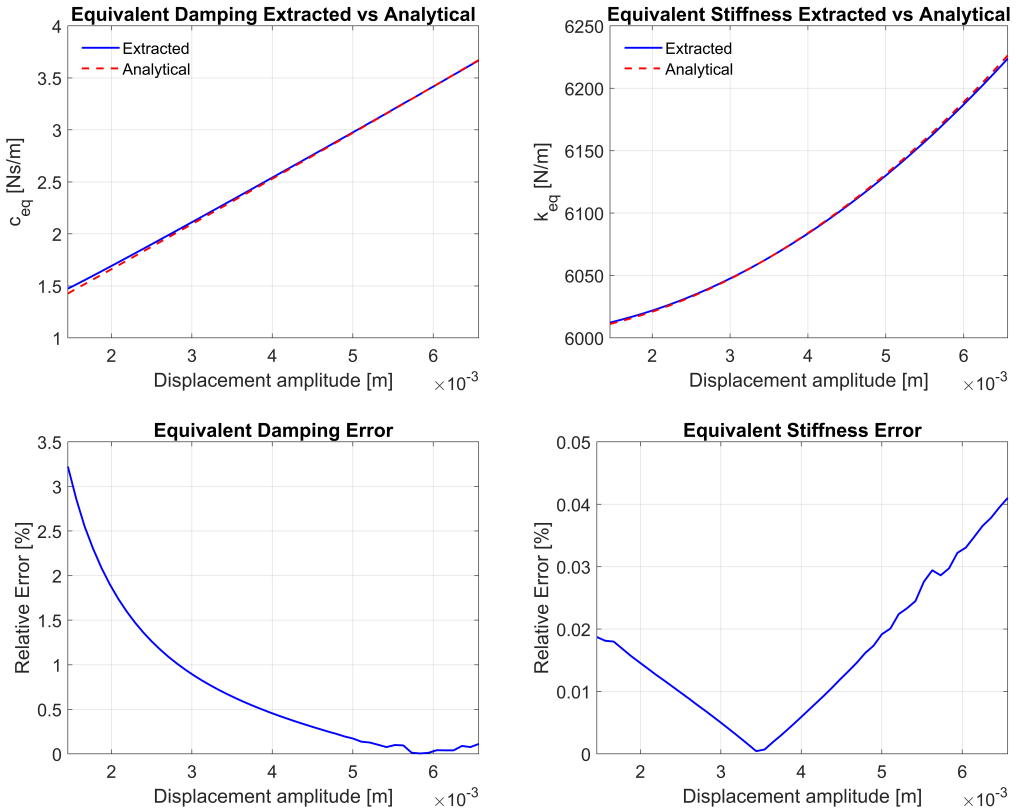

Figure 5.2: SDOF - Cubic stiffness and quadratic damping - CONCERTO

To evaluate the method's robustness to noise, artificial noise was added to the time-domain response of the system. Since the noise was introduced randomly, the identification procedure was repeated on multiple datasets for each noise level. The root mean square (RMS) of the identification error was then computed to quantify the impact of noise. The results are summarized below.

Noise level	Stiffness RMS error (95% CI)	Damping RMS error (95% CI)
10%	$(2.91 \cdot 10^{-2} \pm 3.07 \cdot 10^{-4})\%$	$(3.60 \pm 1.05 \cdot 10^{-2})\%$
8%	$(2.89 \cdot 10^{-2} \pm 2.07 \cdot 10^{-4})\%$	$(3.60 \pm 5.92 \cdot 10^{-3})\%$
6%	$(2.89 \cdot 10^{-2} \pm 1.17 \cdot 10^{-4})\%$	$(3.60 \pm 4.26 \cdot 10^{-3})\%$

Figure 5.3 presents the results obtained using Modified Dobson, comparing them with the corresponding analytical values.
The comparison confirms the high accuracy of the method overall; however, the damping function shows a higher relative error at higher displacement levels.

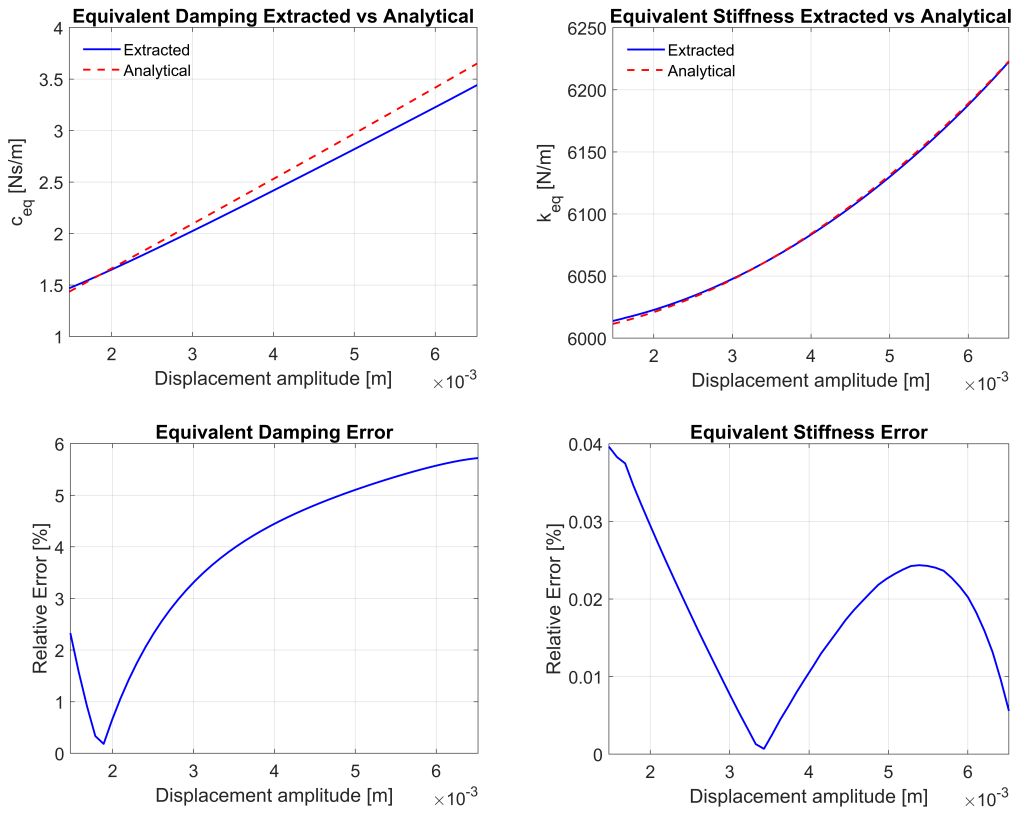

Figure 5.3: SDOF - Cubic stiffness and quadratic damping - Modified Dobson

To evaluate the method's robustness to noise, artificial noise was added to the time-domain response of the system. Since the noise was introduced randomly, the identification procedure was repeated on multiple datasets for each noise level.
The root mean square (RMS) of the identification error was then computed to quantify the impact of noise. The results are summarized below.

Noise level	Stiffness RMS error (95% CI)	Damping RMS error (95% CI)
10%	$(1.22 \cdot 10^{-1} \pm 1.23 \cdot 10^{-3})\%$	$(7.93 \pm 8.35 \cdot 10^{-2})\%$
8%	$(1.24 \cdot 10^{-1} \pm 1.29 \cdot 10^{-3})\%$	$(7.95 \pm 6.34 \cdot 10^{-2})\%$
6%	$(1.23 \cdot 10^{-1} \pm 1.21 \cdot 10^{-3})\%$	$(7.81 \pm 7.99 \cdot 10^{-2})\%$

5.3.2 SDOF - Coulomb damping - Results

The system under investigation is a Single-Degree-of-Freedom (SDOF) system with base excitation, governed by the following equation of motion:

$$m\ddot{y} + F_f sign(\dot{y} - \dot{b}) + c(\dot{y} - \dot{b}) + k(y - b) = 0 \tag{5.31}$$

In this case only the damping contribution is analyzed, as the stiffness term is purely linear.

Figure 5.4 presents the results obtained using CONCERTO, comparing them with the corresponding analytical values.
The comparison confirms the high accuracy of the method, showing excellent agreement with the analytical solution, with a low relative error.

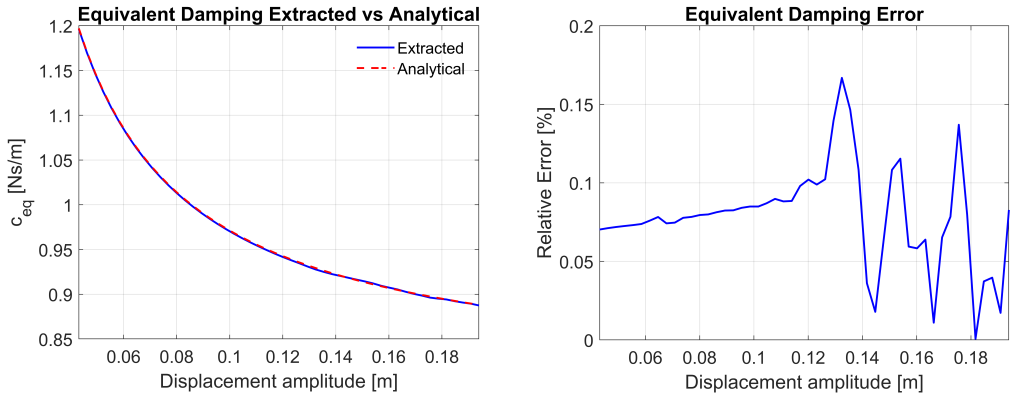

Figure 5.4: SDOF- Coulomb damping - CONCERTO

To evaluate the method's robustness to noise, artificial noise was added to the time-domain response of the system. Since the noise was introduced randomly, the identification procedure was repeated on multiple datasets for each noise level.
The root mean square (RMS) of the identification error was then computed to quantify the impact of noise. The results are summarized below.

Noise level	Damping RMS error (95% CI)
10%	$(1.01 \cdot 10^{-1} \pm 1.05 \cdot 10^{-2})\%$
8%	$(9.50 \cdot 10^{-2} \pm 4.81 \cdot 10^{-3})\%$
6%	$(9.12 \cdot 10^{-2} \pm 3.56 \cdot 10^{-3})\%$

Figure 5.5 presents the results obtained using Modified Dobson, comparing them with the corresponding analytical values.
The comparison shows an agreement with the analytical solution, although the associated errors are higher compared to those observed with the CONCERTO method.

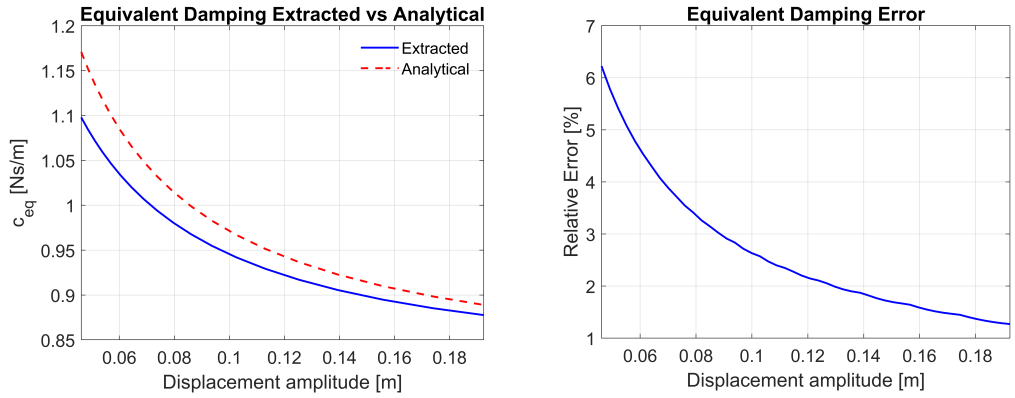

Figure 5.5: SDOF - Coulomb damping - Modified Dobson

To evaluate the method's robustness to noise, artificial noise was added to the time-domain response of the system. Since the noise was introduced randomly, the identification procedure was repeated on multiple datasets for each noise level.
The root mean square (RMS) of the identification error was then computed to quantify the impact of noise. The results are summarized below:

Noise level	Damping RMS error (95% CI)
10%	$(3.83 \pm 3.38 \cdot 10^{-2})\%$
8%	$(3.85 \pm 3.69 \cdot 10^{-2})\%$
6%	$(3.85 \pm 2.77 \cdot 10^{-2})\%$

5.3.3 2DOFs - Cubic stiffness and quadratic damping - Results

To evaluate the CONCERTO method's reliability in the presence of multiple vibration modes, we consider a two-degree-of-freedom (2DOFs) system subjected to base excitation, as illustrated in Figure 5.6. In this configuration, the elements k_1 and c_1 exhibit nonlinear behavior (cubic stiffness and quadratic damping), while k_2 and c_2 are linear.

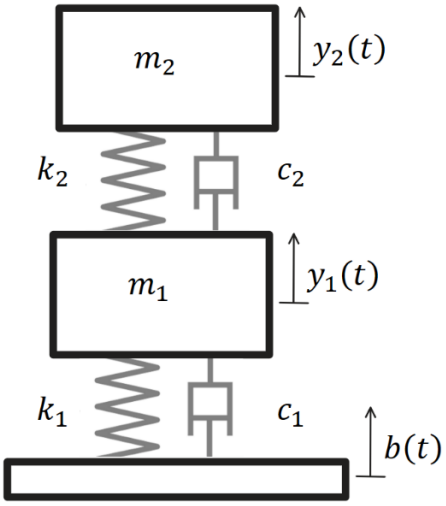

Figure 5.6: Scheme of a 2DOF system

The dynamic response of the system is governed by the following set of coupled differential equations:

$$\begin{cases} m_1\ddot{y}_1 + c_1(\dot{y}_1 - \dot{b}) + c_{nl,1}(\dot{y}_1 - \dot{b})|\dot{y}_1 - \dot{b}| - c_2(\dot{y}_2 - \dot{y}_1) + \\ \quad +k_1(y_1 - b) + k_{nl,1}(y_1 - b)^3 - k_2(y_2 - y_1) = 0 \\ \quad m_2\ddot{y}_2 + c_2(\dot{y}_2 - \dot{y}_1) + k_2(y_2 - y_1) = 0 \end{cases} \tag{5.32}$$

By substituting the analytical expressions for the equivalent stiffness and damping functions, derived using the first-order harmonic balance approximation, (5.32) becomes:

$$\begin{cases} m_1\ddot{y}_1 + \left(c_1 + \frac{8}{3\pi}c_{nl}|Y_1 - B|\omega_r\right)(\dot{y}_1 - \dot{b}) - c_2(\dot{y}_2 - \dot{y}_1) + \\ \quad + \left(k_1 + \frac{3}{4}k_{nl,1}|Y_1 - B|^2\right)(y_1 - b) - k_2(y_2 - y_1) = 0 \\ \quad m_2\ddot{y}_2 + c_2(\dot{y}_2 - \dot{y}_1) + k_2(y_2 - y_1) = 0 \end{cases} \tag{5.33}$$

We can express (5.33) in compact matrix form as:

$$\begin{bmatrix} m_1 & 0 \\ 0 & m_2 \end{bmatrix}\begin{pmatrix} \ddot{y}_1 \\ \ddot{y}_2 \end{pmatrix} + \begin{bmatrix} c_1 + \frac{8}{3\pi}c_{nl}|Y_1 - B|\omega_r + c_2 & -c_2 \\ -c_2 & c_2 \end{bmatrix}\begin{pmatrix} \dot{y}_1 \\ \dot{y}_2 \end{pmatrix} + \begin{bmatrix} k_1 + \frac{3}{4}k_{nl,1}|Y_1 - B|^2 + k_2 & -k_2 \\ -k_2 & k_2 \end{bmatrix}\begin{pmatrix} y_1 \\ y_2 \end{pmatrix} = \begin{pmatrix} \left(c_1 + \frac{8}{3\pi}c_{nl}|Y_1 - B|\omega_r\right)\dot{b} + \left(k_1 + \frac{3}{4}k_{nl,1}|Y_1 - B|^2\right)b \\ 0 \end{pmatrix} \tag{5.34}$$

From (5.34), we can identify the system matrices:

$$[K] = \begin{bmatrix} k_1 + \frac{3}{4}k_{nl,1}|Y_1 - B|^2 + k_2 & -k_2 \\ -k_2 & k_2 \end{bmatrix}$$
$$[C] = \begin{bmatrix} c_1 + \frac{8}{3\pi}c_{nl}|Y_1 - B|\omega_r + c_2 & -c_2 \\ -c_2 & c_2 \end{bmatrix} \quad [M] = \begin{bmatrix} m_1 & 0 \\ 0 & m_2 \end{bmatrix} \tag{5.35}$$

By solving the eigenvalue problem (EVP), we obtain the diagonal matrix $[\Lambda]$, containing the squared natural frequencies and the modal matrix $[\Phi]$. This allows us to compute the analytical modal mass, stiffness, and damping matrices as:

$$\begin{aligned} diag(m_r) &= [\Phi]^T[M][\Phi] \\ diag(k_r) &= [\Phi]^T[K][\Phi] \\ diag(c_r) &= [\Phi]^T[C][\Phi] \end{aligned} \tag{5.36}$$

Repeating the procedure for different values of $|Y_1 - B|$ yields the analytical trends of modal stiffness and damping over the displacement range selected.

To evaluate the robustness of the method, a parametric analysis was conducted by varying the values of k_2 and m_2, keeping the remaining parameters unchanged. The extracted modal parameters were subsequently validated against analytical values.

If $k_2 = 10\ k_1$ and $m_2 = m_1$, the natural frequencies of the linear system are:

$$\begin{cases} \omega_1 = 7.03\ Hz \\ \omega_2 = 45.59\ Hz \end{cases} \rightarrow \omega_2 - \omega_1 = 38.56\ Hz$$

This gives us a measure of the distance between the two modes.

Figure 5.7 presents the results obtained by applying the CONCERTO method, showing a comparison between the extracted parameters and the analytical reference values.

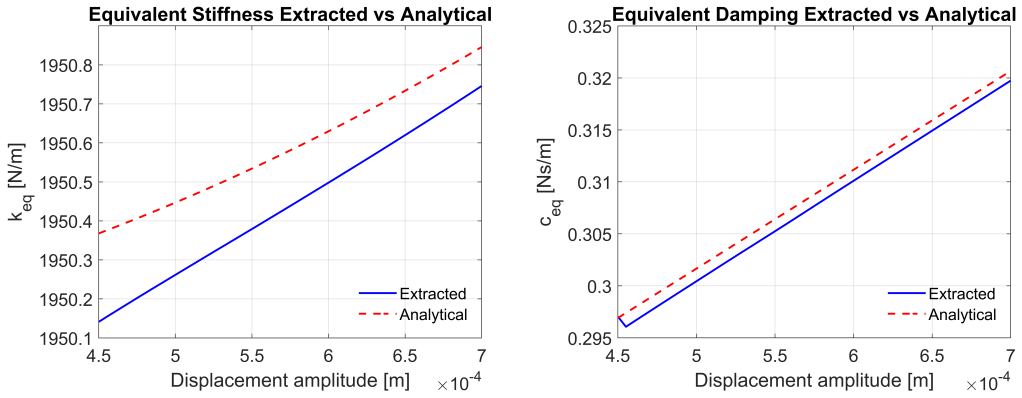

Figure 5.7: 2DOFs - $k_2 = 10\ k_1$, $m_2 = m_1$

The plots confirm the accuracy of the method in identifying both equivalent stiffness and damping functions. Quantitatively, the root mean square (RMS) errors are:

- Stiffness RMS error: $7.90 \cdot 10^{-3}$ %
- Damping RMS error: $3.58 \cdot 10^{-1}$ %

If $k_2 = 0.5\ k_1$ and $m_2 = 0.5\ m_1$, the natural frequencies of the linear system are:

$$\begin{cases} \omega_1 = 7.12\ Hz \\ \omega_2 = 14.24\ Hz \end{cases} \rightarrow \omega_2 - \omega_1 = 7.12\ Hz$$

Figure 5.8 presents the results obtained by applying the CONCERTO method, showing a comparison between the extracted parameters and the analytical reference values.

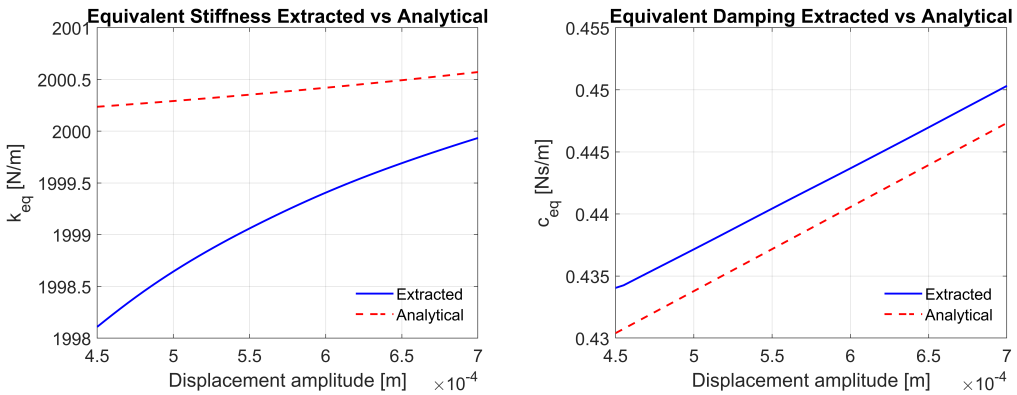

Figure 5.8: 2DOFs - $k_2 = 0.5\ k_1$, $m_2 = 0.5\ m_1$

The plots confirm the accuracy of the method in identifying both equivalent stiffness and damping functions. Quantitatively, the root mean square (RMS) errors are:

- Stiffness RMS error: $6.49 \cdot 10^{-2}$ %
- Damping RMS error: $7.33 \cdot 10^{-1}$ %

If $k_2 = 0.2\ k_1$ and $m_2 = 0.2 m_1$, the natural frequencies of the linear system are:

$$\begin{cases} \omega_1 = 8.06\ Hz \\ \omega_2 = 12.57\ Hz \end{cases} \rightarrow \omega_2 - \omega_1 = 4.50\ Hz$$

Figure 5.9 presents the results obtained by applying the CONCERTO method, showing a comparison between the extracted parameters and the analytical reference values.

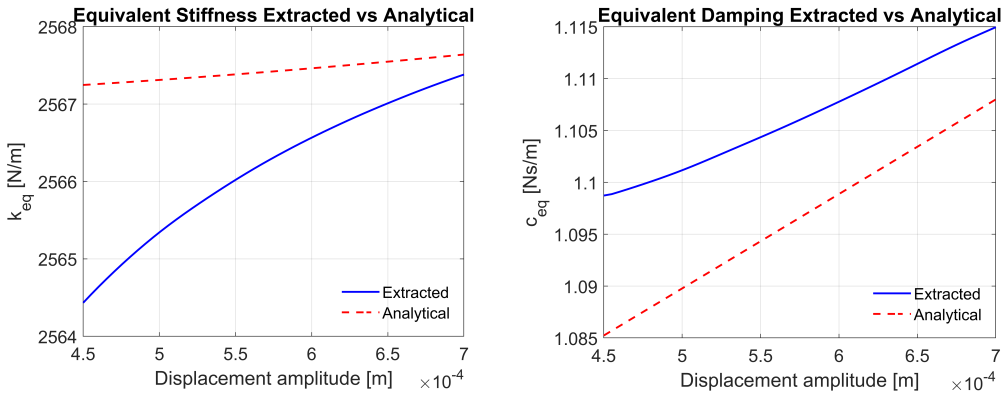

Figure 5.9: 2DOFs - $k_2 = 0.2\ k_1$, $m_2 = 0.2\ m_1$

The plots confirm the accuracy of the method in identifying both equivalent stiffness and damping functions. Quantitatively, the root mean square (RMS) errors are:

- Stiffness RMS error: $5.63 \cdot 10^{-2}$ %
- Damping RMS error: 1.16 %

These results confirm the reliability of the CONCERTO method in identifying nonlinear modal parameters, even in systems with multiple degrees of freedom. Furthermore, it is observed that as the two vibration modes approach each other in frequency, the root mean square (RMS) error increases accordingly, indicating a reduced identifiability due to modal interaction.

5.4 Validation with experimental data

In this section, the CONCERTO and Modified Dobson methods are applied to experimental data in order to evaluate their effectiveness in identifying nonlinear dynamic characteristics in real-world systems.
The aim is to assess the practical applicability of these two frequency-domain identification techniques under realistic conditions, including measurement noise and non-ideal excitation.

Starting from the measured responses, the modal parameter functions (modal frequency, modal damping ratio and modal constants) are extracted using each method. These amplitude-dependent parameters are then used to reconstruct the nonlinear Frequency Response Function (FRF) of the system using the New Method (NM).

The reconstructed FRFs are compared to those directly obtained from experimental measurements, allowing for a detailed assessment of the accuracy, consistency and robustness of each method.

It is important to note that the two experimental systems considered differ not only in configuration but also in the type of frequency response data available:

- In Experimental System 1, the structure is excited at the base and the measured quantity is the transmissibility
- In Experimental System 2 the input force and output acceleration are both measured, thus allowing access to the receptance

5.4.1 Experimental System - 1

The first experimental case involves a mechanical system subjected to base excitation through a sine sweep with increasing frequency.

Three excitation levels are considered, corresponding to increasing RMS values of the base acceleration. These different levels of excitation are the following:

- Level 1: Base acceleration RMS: $0.34\ m/s^2$
- Level 2: Base acceleration RMS: $1.40\ m/s^2$
- Level 3: Base acceleration RMS: $3.10\ m/s^2$

For each level, modal parameters are extracted using both the CONCERTO and Modified Dobson methods. These parameters are subsequently used to reconstruct the nonlinear transmissibility function, which is then compared to the reference curve obtained directly from experimental measurements. In this case the modal parameters are evaluated as a function of the displacement amplitude $|Y - B|$.

5.4.1.1 CONCERTO Results

The following figures report the modal parameters extracted using the CONCERTO method for Experimental System−1 under increasing excitation levels. Each figure displays the evolution of the natural frequency and the modal damping ratio as a function of the response displacement amplitude.

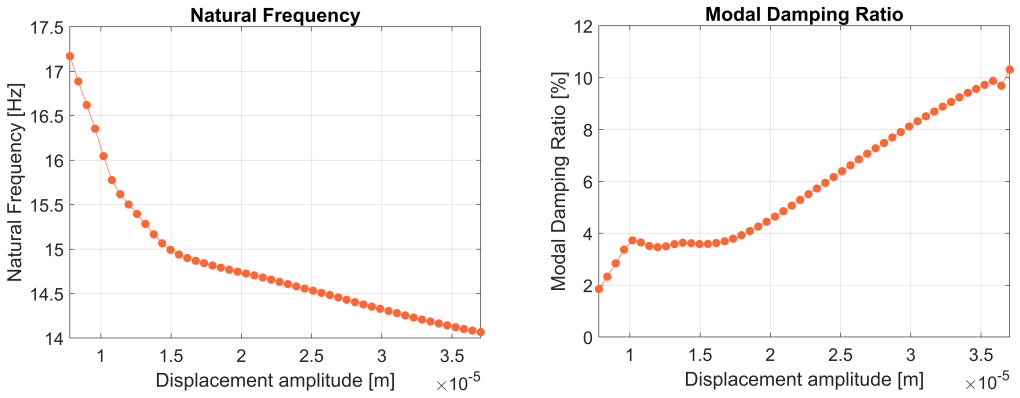

Figure 5.10: Experimental MDOF 1 - Level 1 - Modal parameters - CONCERTO

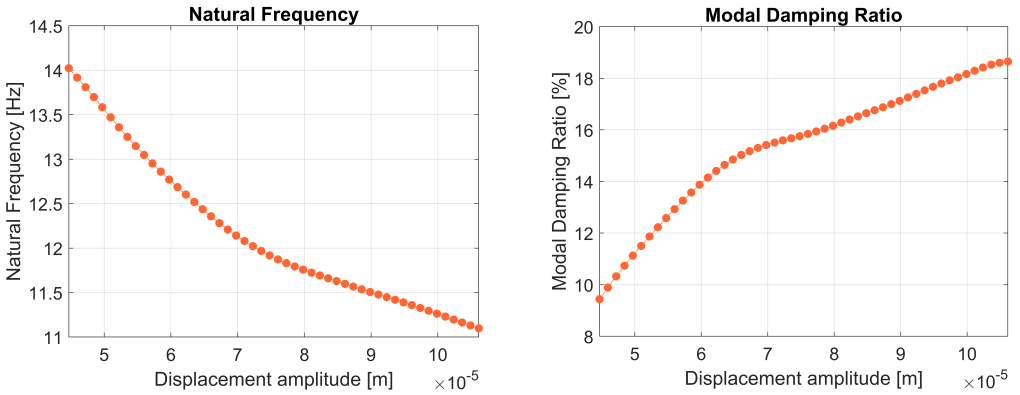

Figure 5.11: Experimental MDOF 1 - Level 2 - Modal parameters - CONCERTO

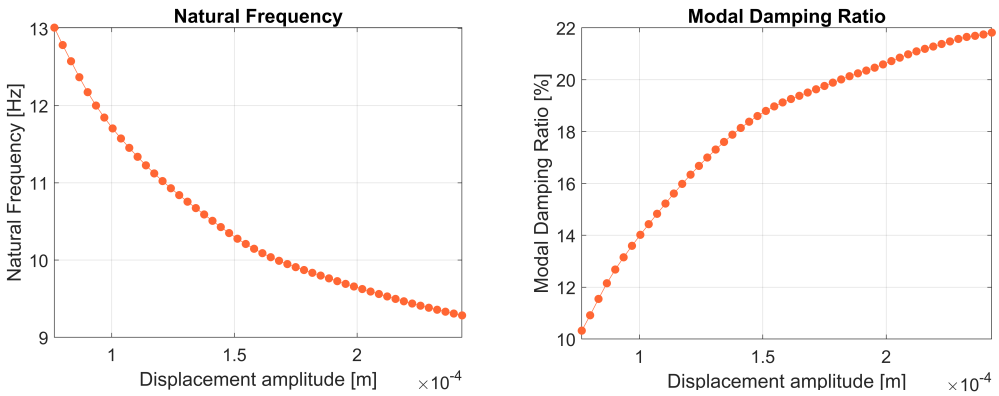

Figure 5.12: Experimental MDOF 1- Level 3 - Modal parameters - CONCERTO

The natural frequency systematically decreases with increasing displacement amplitude, revealing a robust and repeatable softening stiffness behavior. The modal damping ratio shows a consistent growth with displacement amplitude.

The following figures present the comparison between the nonlinear FRFs reconstructed using the CONCERTO method and the original experimental FRFs for the three excitation levels tested on the Experimental MDOF−1 system.

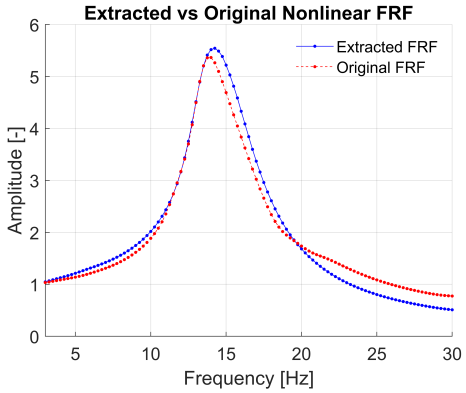

Figure 5.13: Experimental MDOF 1 - Level 1 - FRF comparison - CONCERTO

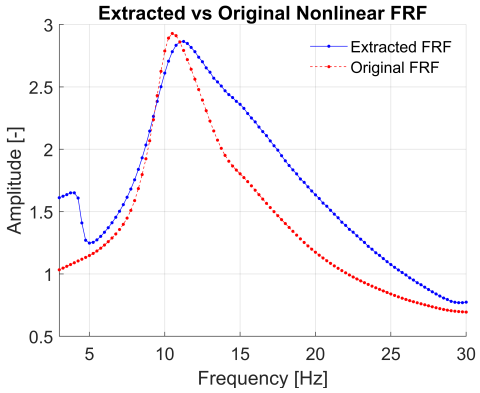

Figure 5.14: Experimental MDOF 1 - Level 2 - FRF comparison - CONCERTO

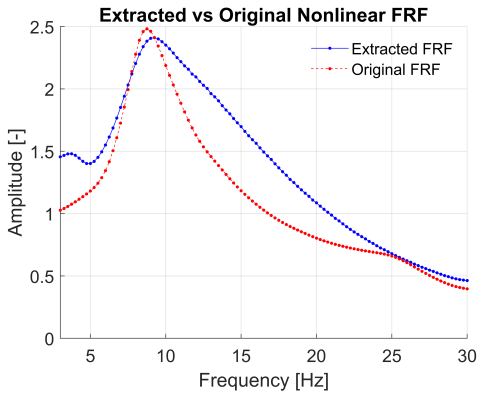

Figure 5.15: Experimental MDOF 1 - Level 3 - FRF comparison - CONCERTO

As the excitation level increases, some discrepancies become more noticeable:

- At Level 1: the match between the two curves is good, both in amplitude and shape, indicating a high degree of accuracy in identifying weakly nonlinear behavior.
- At Level 2: a slight divergence begins to appear, particularly in the post-resonant region, where the reconstructed FRF tends to overestimate the response amplitude.
- At Level 3: the discrepancy becomes more pronounced.

These trends suggest that while the CONCERTO method remains effective across all levels, its accuracy slightly deteriorates as the nonlinearities become more significant. Such behavior is typical in nonlinear identification problems, where stronger nonlinear effects tend to challenge the precision of the estimation process. Nonetheless, the results confirm the robustness of the method and its overall suitability for nonlinear modal identification, particularly under low-to-moderate excitation conditions.

Figure 5.16 presents the results obtained from the CONCERTO method at all three excitation levels. The plots are shown together to illustrate the global system behavior, highlighting how the natural frequency and damping ratio evolve as functions of displacement amplitude.

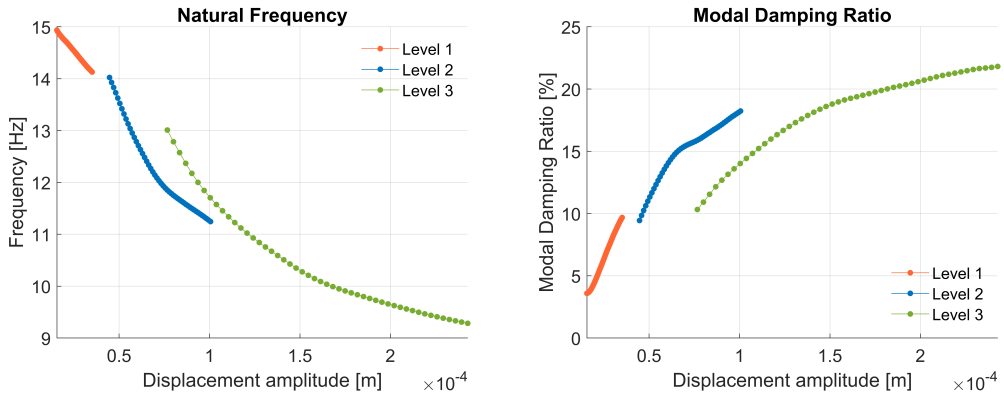

Figure 5.16: Experimental MDOF 1 - Levels combined - CONCERTO

The trends observed across the different excitation levels exhibit a consistent qualitative behavior: the natural frequency decreases, while the damping ratio increases with growing displacement amplitude. This confirms the presence of softening stiffness and amplitude-dependent damping in the system.

However, despite this consistent evolution, the absolute values of the identified parameters reveal some discrepancies across the different excitation levels, particularly in the overlapping displacement regions. These mismatches may be attributed to the influence of strong nonlinearities, especially at higher excitation levels, which could violate the assumptions underlying the identification method.

Further investigation is required to understand whether these differences are due to modeling limitations, measurement uncertainty or additional unmodeled nonlinear effects.

5.4.1.2 Modified Dobson Results

The following figures report the modal parameters extracted using the Modified Dobson method for Experimental System−1 under increasing excitation levels. Each figure displays the evolution of the natural frequency and the modal damping ratio as a function of the response displacement amplitude.

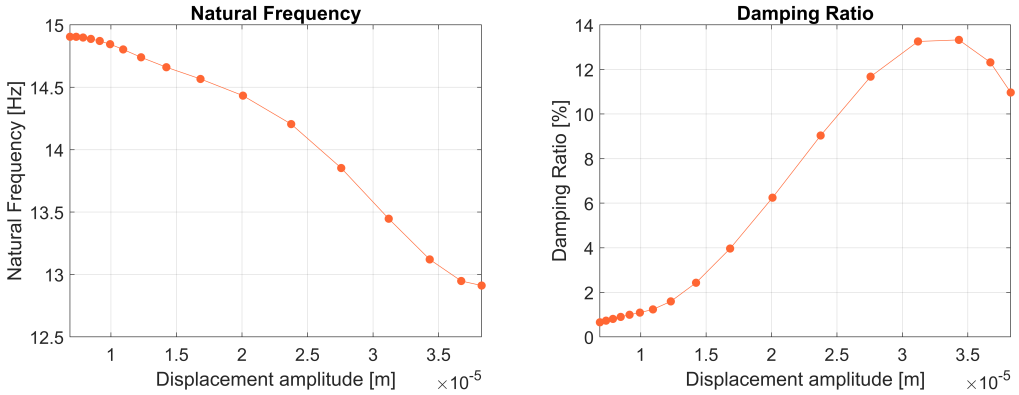

Figure 5.17: Experimental MDOF 1 - Level 1 - Modal parameters - Modified Dobson

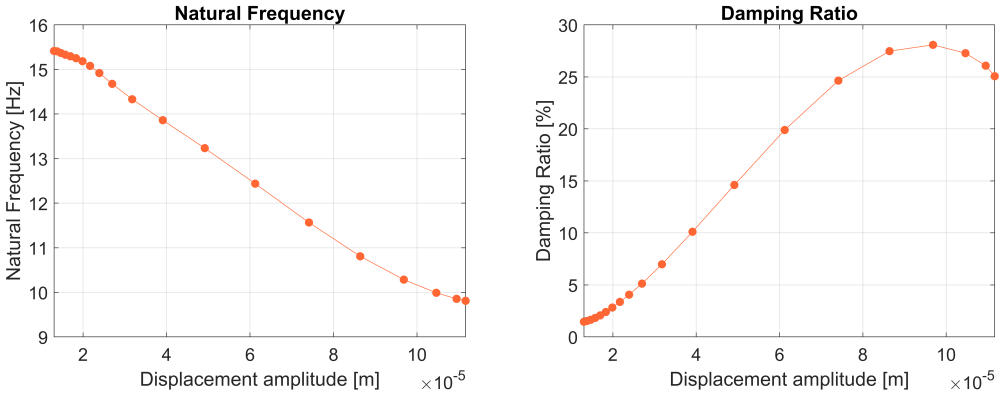

Figure 5.18: Experimental MDOF 1 - Level 2 - Modal parameters - Modified Dobson

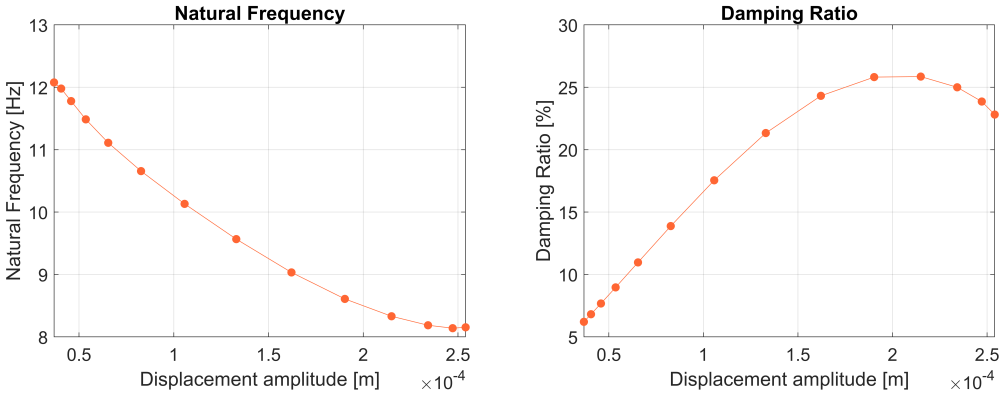

Figure 5.19: Experimental MDOF 1- Level 3 - Modal parameters - Modified Dobson

The natural frequency systematically decreases with increasing displacement, revealing a robust and repeatable softening stiffness behavior. The modal damping ratio shows a consistent growth with displacement amplitude.

The following figures present the comparison between the nonlinear FRFs reconstructed using the Modified Dobson method and the original experimental FRFs for the three excitation levels tested on the Experimental MDOF−1 system.

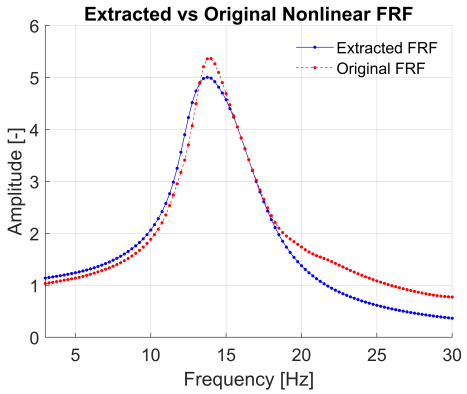

Figure 5.20: Experimental MDOF 1 - Level 1 - FRF comparison - Modified Dobson

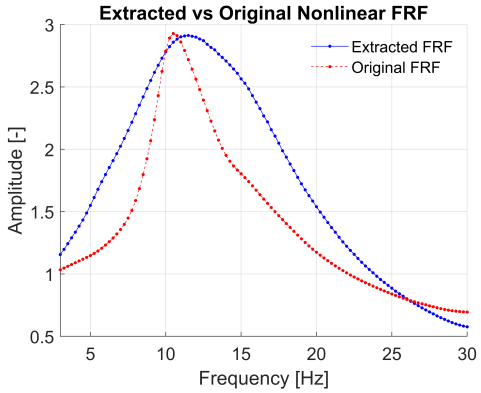

Figure 5.21: Experimental MDOF 1 - Level 2 - FRF comparison - Modified Dobson

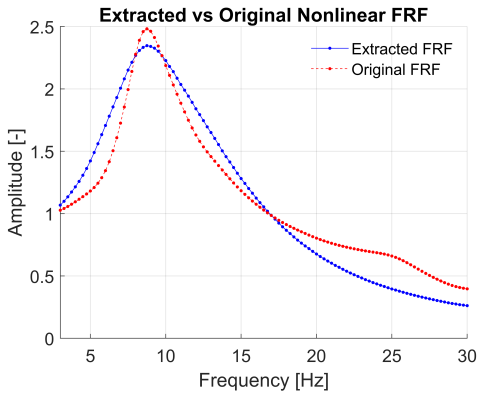

Figure 5.22: Experimental MDOF 1 - Level 3 - FRF comparison - Modified Dobson

As the excitation level increases, some discrepancies become more noticeable:

- At Level 1: the agreement is good, especially near the peak, with minor deviations observed in the tails of the curve.
- At Level 2: characterized by evident discrepancies.
- At Level 3: the differences become less pronounced.

These trends suggest that while the Modified Dobson method remains effective across all levels, its accuracy slightly deteriorates as the nonlinearities become more significant. Such behavior is typical in nonlinear identification problems, where stronger nonlinear effects tend to challenge the precision of the estimation process. Nonetheless, the results confirm the robustness of the method and its overall suitability for nonlinear modal identification, particularly under low-to-moderate excitation conditions.

Figure 5.23 presents the results obtained from the Modified Dobson method at all three excitation levels. The plots are shown together to illustrate the global system behavior, highlighting how the natural frequency and damping ratio evolve as functions of displacement amplitude.

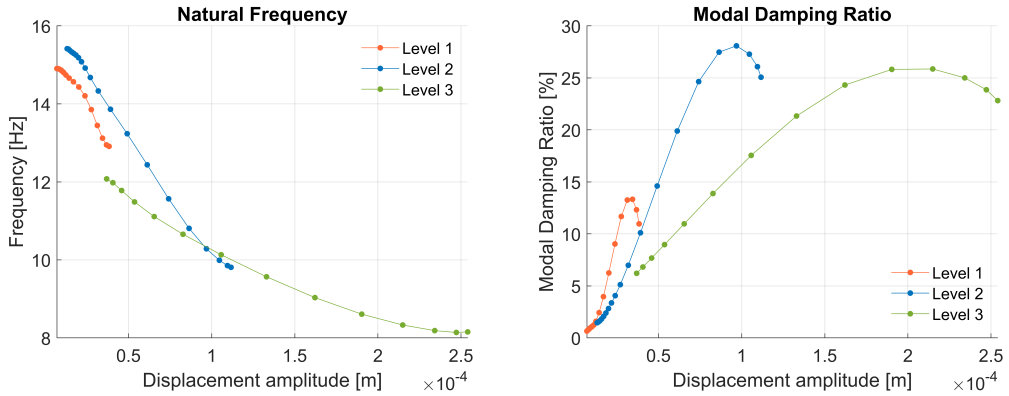

Figure 5.23: Experimental MDOF 1 - Levels combined - Modified Dobson

The trends observed across the different excitation levels exhibit a consistent qualitative behavior: the natural frequency decreases, while the damping ratio increases with growing displacement amplitude. This confirms the presence of softening stiffness and amplitude-dependent damping in the system.

However, despite this consistent evolution, the absolute values of the identified parameters reveal some discrepancies across the different excitation levels, particularly in the overlapping displacement regions. These mismatches may be attributed to the influence of strong nonlinearities, especially at higher excitation levels, which could violate the assumptions underlying the identification method.

Further investigation is required to understand whether these differences are due to modeling limitations, measurement uncertainty or additional unmodeled nonlinear effects.

5.4.2 Experimental system - 2

In this second experimental setup, the system is excited directly by a force input and the receptance is measured. This configuration differs from Experimental System 1, in which the measured quantity was the transmissibility under base excitation.

Three different excitation levels are considered, each characterized by a distinct RMS value of the excitation force These different levels are used to evaluate the sensitivity of the methods to amplitude-dependent nonlinear effects:

- Level 1: excitation force RMS $= 1\ mN$
- Level 2: excitation force RMS $= 2\ mN$
- Level 3: excitation force RMS $= 2.7\ mN$

For each level, modal parameters are extracted using both the CONCERTO and Modified Dobson methods. These parameters are subsequently used to reconstruct the nonlinear receptance function, which is then compared to the reference curve obtained directly from experimental measurements. In this case the modal parameters are evaluated as a function of the displacement amplitude X.

5.4.2.1 CONCERTO Results

The following figures report the modal parameters extracted using the CONCERTO method for Experimental System−2 under increasing excitation levels. Each figure displays the evolution of the natural frequency and the modal damping ratio as a function of the response displacement amplitude.

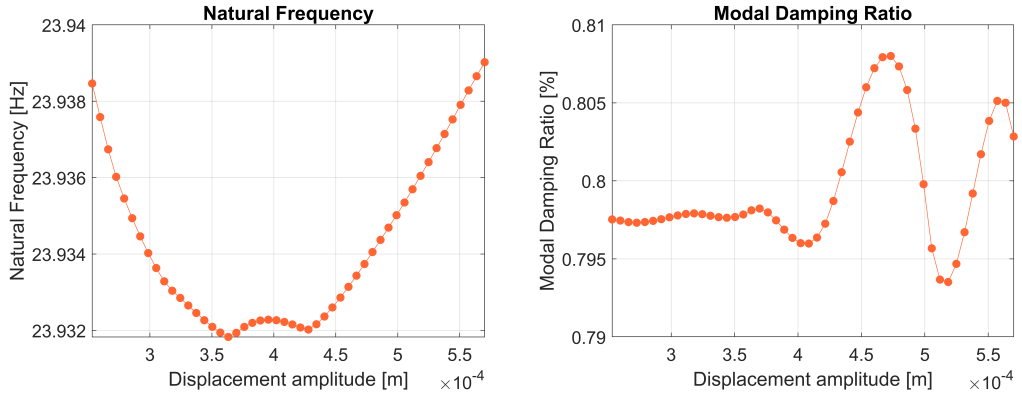

Figure 5.24: Experimental MDOF 2 - Level 1 - Modal parameters - CONCERTO

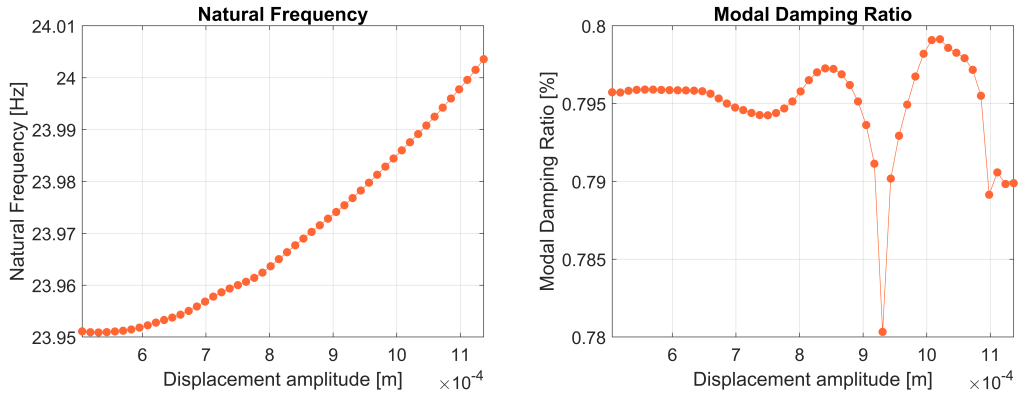

Figure 5.25: Experimental MDOF 2 - Level 2 - Modal parameters - CONCERTO

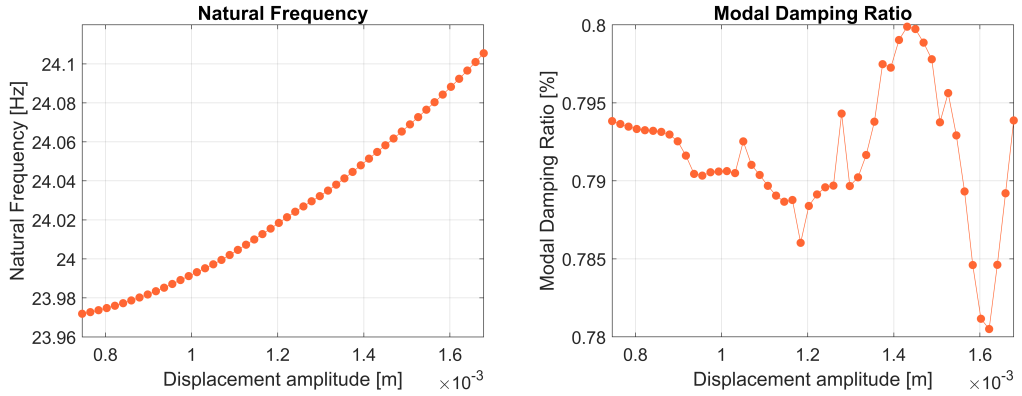

Figure 5.26: Experimental MDOF 2 - Level 3 - Modal parameters - CONCERTO

Except for the Level 1, the natural frequency exhibits an increasing trend with the growth of displacement amplitude, suggesting a typical hardening behavior.
The damping ratio shows more variability across all levels: the values fluctuate significantly, especially at higher amplitudes.

The following figures present the comparison between the nonlinear FRFs reconstructed using the CONCERTO method and the original experimental FRFs for the three excitation levels tested on the Experimental MDOF−2 system.

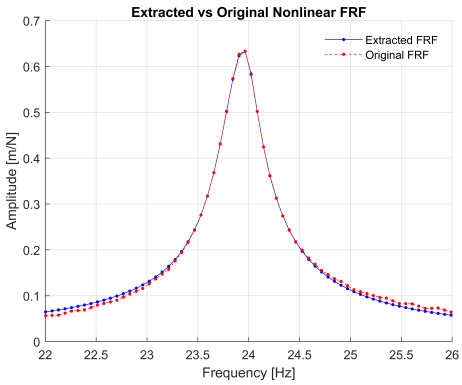

Figure 5.27: Experimental MDOF 2 -Level 1 - FRF comparison - CONCERTO

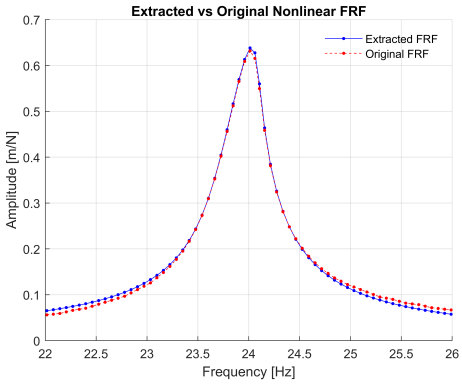

Figure 5.28: Experimental MDOF 2- Level 2 - FRF comparison - CONCERTO

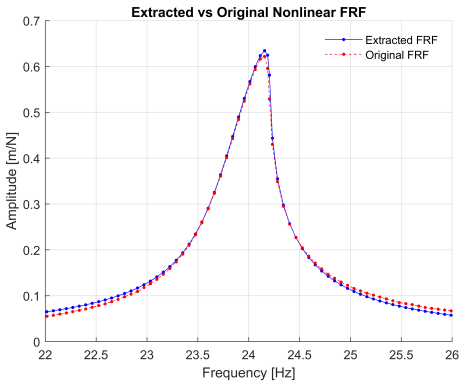

Figure 5.29: Experimental MDOF 2 - Level 3 - FRF comparison - CONCERTO

In all cases, the reconstructed curves align remarkably well with the experimental data. The overlap is especially tight near the resonance peak, indicating that the method accurately captures the dynamic behavior of the system in presence of nonlinearities.

Figure 5.30. presents the results obtained from the CONCERTO method at all three excitation levels. The plots are shown together to illustrate the global system behavior, highlighting how the natural frequency and damping ratio evolve as functions of displacement amplitude.

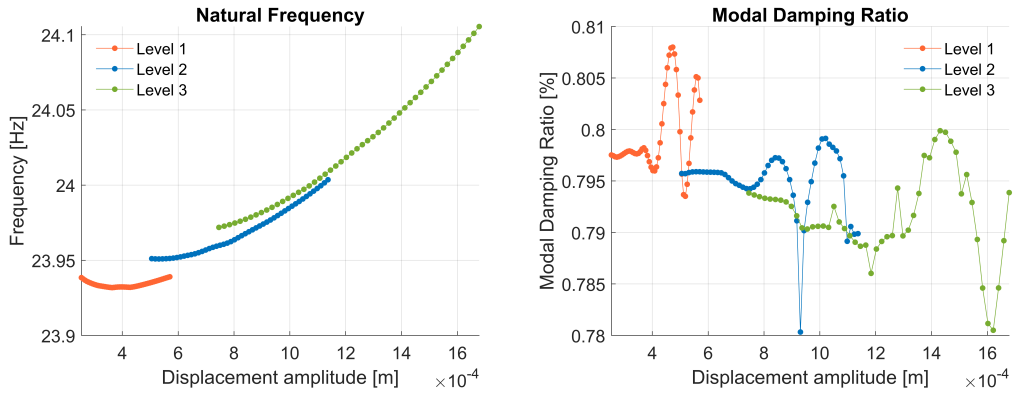

Figure 5.30: Experimental MDOF 2 - Levels combined - CONCERTO

The trends observed across the different excitation levels exhibit a consistent qualitative behavior: the natural frequency increase with growing displacement amplitude, while the damping ratio plot reveals a more irregular pattern.

The absolute values of the identified parameters reveal some discrepancies across the different excitation levels, particularly in the overlapping displacement regions. Further investigation is required to understand whether these differences are due to modeling limitations, measurement uncertainty or additional unmodeled nonlinear effects.

5.4.2.2 Modified Dobson Results

The following figures report the modal parameters extracted using the Modified Dobson method for Experimental System−2 under increasing excitation levels. Each figure displays the evolution of the natural frequency and the modal damping ratio as a function of the response displacement amplitude.

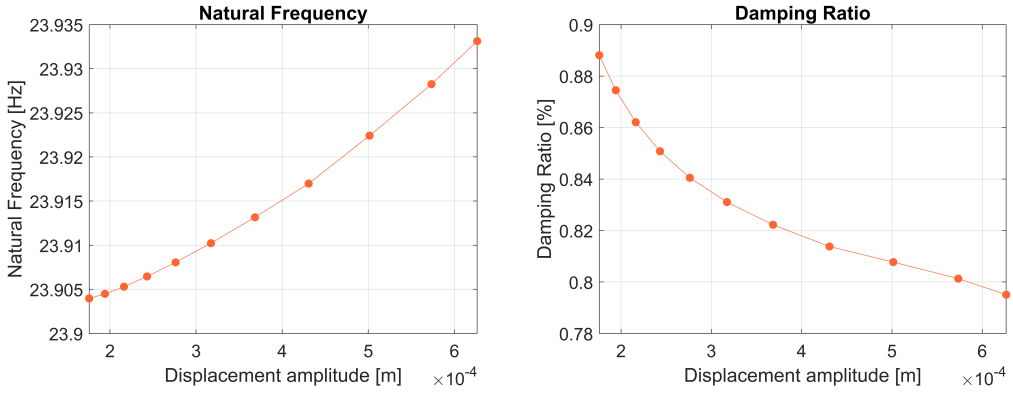

Figure 5.31: Experimental MDOF 2 - Level 1 - Modal parameters - Modified Dobson

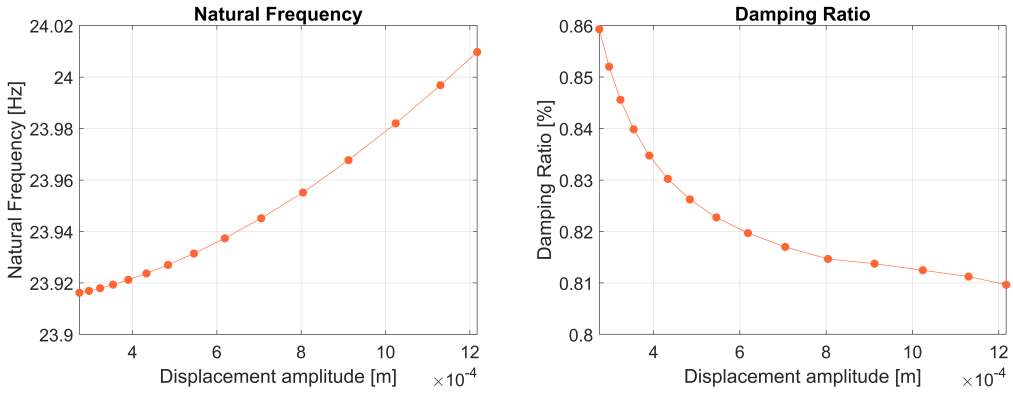

Figure 5.32: Experimental MDOF 2 - Level 2 - Modal parameters - Modified Dobson

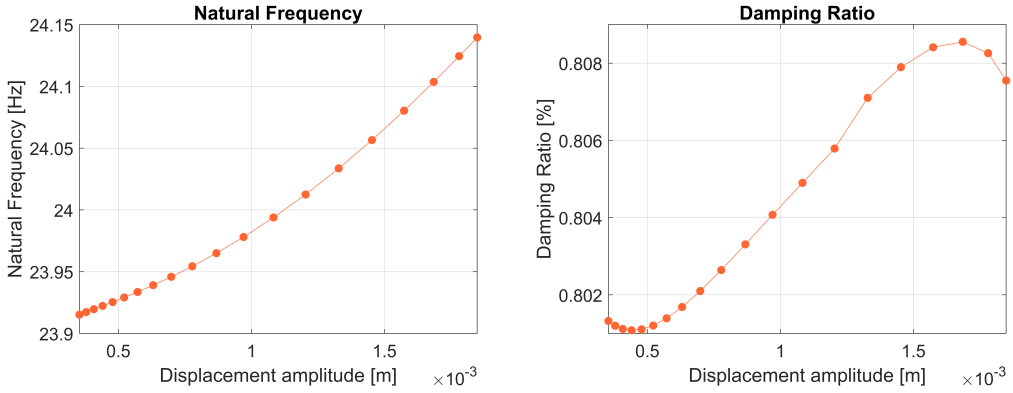

Figure 5.33: Experimental MDOF 2 - Level 3 - Modal parameters - Modified Dobson

The natural frequency systematically increases with increasing displacement, revealing a robust and repeatable hardening stiffness behavior.
The modal damping ratio shows a decrease with displacement amplitude in the first two levels, while it shows an increase in the highest level.

The following figures present the comparison between the nonlinear FRFs reconstructed using the Modified Dobson method and the original experimental FRFs for the three excitation levels tested on the Experimental MDOF−2 system.

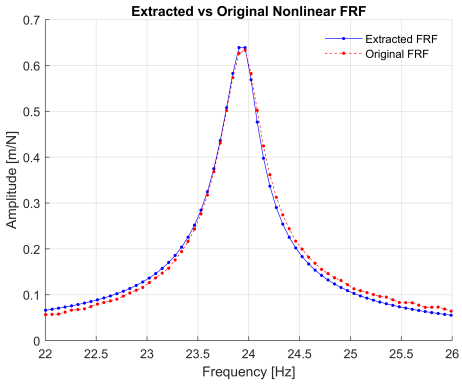

Figure 5.34: Experimental MDOF 2 - Level 1 - FRF comparison - Modified Dobson

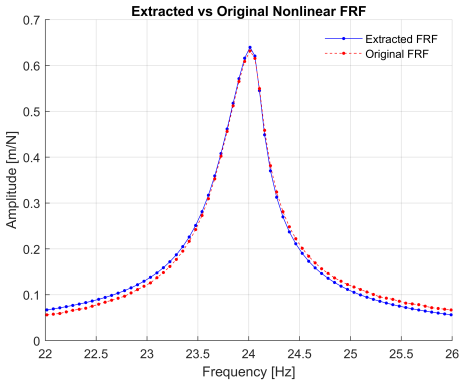

Figure 5.35: Experimental MDOF 2 - Level 2 - FRF comparison - Modified Dobson

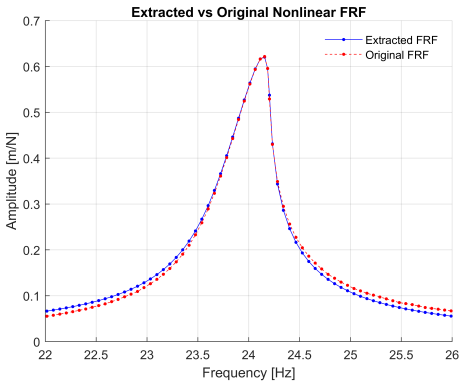

Figure 5.36: Experimental MDOF 2 - Level 3 - FRF comparison - Modified Dobson

In all cases, the reconstructed curves align remarkably well with the experimental data. The overlap is especially tight near the resonance peak, indicating that the method accurately captures the dynamic behavior of the system in presence of nonlinearities.

Figure 5.37 presents the results obtained from the Modified Dobson method at all three excitation levels. The plots are shown together to illustrate the global system behavior, highlighting how the natural frequency and damping ratio evolve as functions of displacement amplitude.

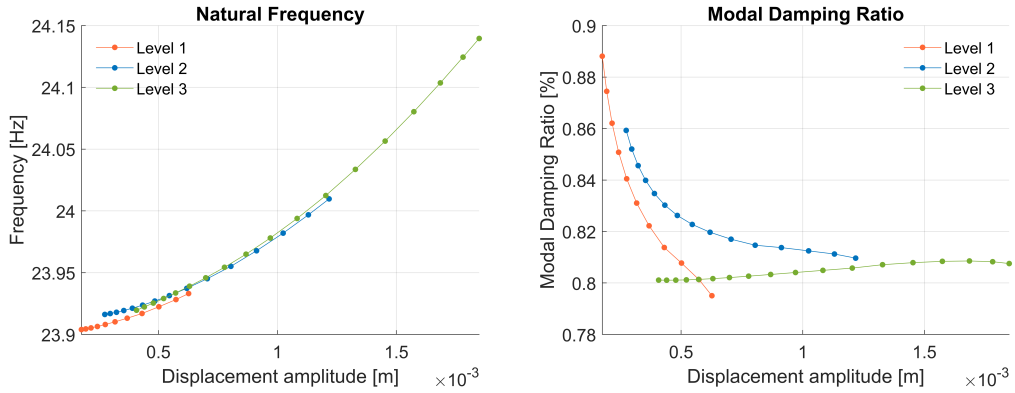

Figure 5.37: Experimental MDOF 2 - Levels combined - Modified Dobson

The trends observed across the different excitation levels exhibit a consistent qualitative behavior: the natural frequency increase with growing displacement amplitude, while the damping ratio plot reveals a more irregular pattern.

The absolute values of the identified parameters reveal some discrepancies across the different excitation levels, particularly in the overlapping displacement regions. Further investigation is required to understand whether these differences are due to modeling limitations, measurement uncertainty or additional unmodeled nonlinear effects.

5.5 Comparison between the two methods

This section compares the two parameter extraction methods (CONCERTO and Modified Dobson) by analyzing the evolution of the modal parameters as functions of displacement amplitude for both experimental systems.

For Experimental MDOF System 1, Figure 5.38 shows the trends of natural frequency and modal damping ratio across the three excitation levels for both methods.

Overall, both methods exhibit a consistent decreasing trend in natural frequency as displacement increases, which is indicative of softening behavior. Similarly, both methods capture a general increase in modal damping ratio with displacement amplitude, highlighting the presence of amplitude-dependent damping effects.

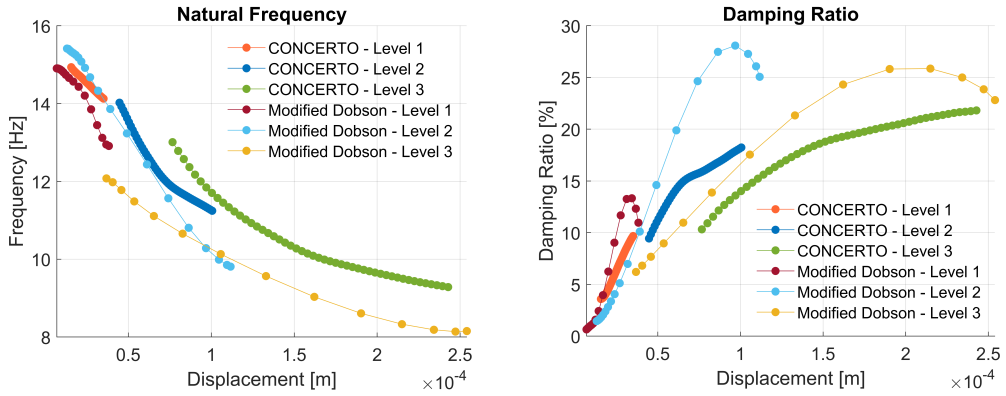

Figure 5.38: Experimental MDOF 1 – Comparison between methods

For Experimental MDOF System 2, as illustrated in Figure 5.39, both identification methods capture a consistent increasing trend in natural frequency with growing displacement amplitude, which is indicative of a hardening-type nonlinear behavior. In contrast, the damping ratio does not exhibit a clearly defined pattern, suggesting a more complex or irregular dependence on displacement, possibly influenced by measurement noise or unmodeled nonlinear effects.

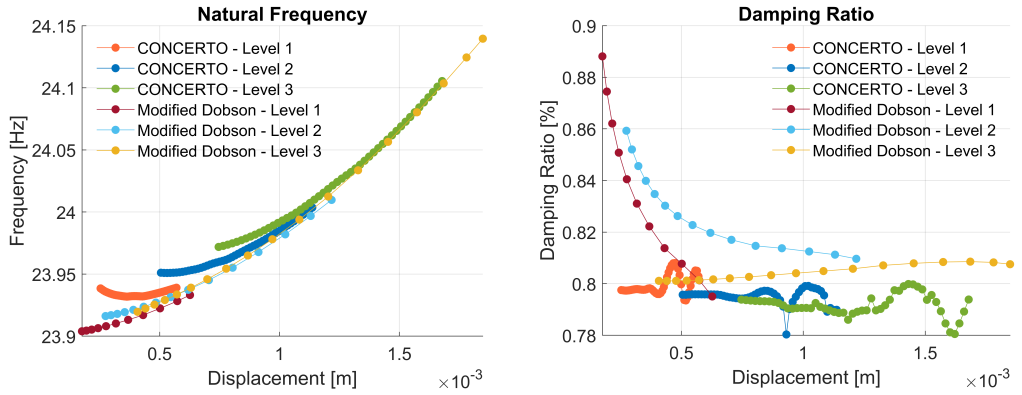

Figure 5.39: Experimental MDOF 2 – Comparison between methods

6 LEOB

The data analyzed in this section refers to the structure under investigation: the Large Deployable Reflector for Earth Observation (LEOB).
This structure exhibits complex mechanical behavior due to its lightweight construction, large dimensions, and a deployable architecture involving mechanical joints.
The presence of joints and potential contact interfaces introduces significant nonlinearities that complicate both numerical modeling and experimental testing.

6.1 LEOB Testing

The data analyzed originates from a qualification vibration test campaign, whose primary objective is to verify that the hardware can withstand the specified vibration environment, which is considered as one of the critical functions.
All three axes were tested in both the vertical and horizontal configurations of the shaker.
In particular, the system was excited by a sine vibration induced by two electrodynamics shakers working together in the push-pull mode for vertical and horizontal configuration.

Figure 6.1 represents a schematic sketch of LEOB test configuration where the coordinate system is defined.

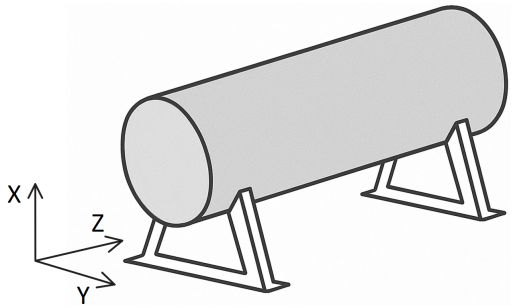

Figure 6.1: LEOB Stylized sketch

X axis tests have been performed in vertical configuration of shaker with head expander, while Y and Z axes tests have been performed in horizontal slip table configuration of the shaker.

The sensors employed are accelerometers and their scope is twofold:

- Control and monitor the vibration levels and input spectrum (pilots)
- Measure the acceleration response (nonpilots)

The system was subjected to four sine test types, characterized by different frequency range and levels:

- resonance search,
- low-level sine,
- intermediate-level sine,
- full-level sine.

The Resonance Search is a sinusoidal excitation that is conducted at the beginning of the test sequence and after every sine to check the integrity of the structure.

We can see the definition of the different types in the Table 6.1 and Table 6.2.

Excitation type	Frequency [Hz]	Acceleration or Displacement	Sweep Rate
Resonance Search	5 – 2000	0.5g	2 oct./min
Low-level sine	5 – 10.2	± 10 mm	2 oct./min
(35% of full level)	10.2 – 120	4.2 g	
Intermediate-level sine	5 – 14.4	± 10 mm	2 oct./min
(70% of full level)	14.4 – 120	8.4 g	
Full-level sine	5 – 17.3	± 10 mm	2 oct./min
	17.3 – 120	12 g	

Table 6.1 – Test for Z axis

Excitation type	Frequency [Hz]	Acceleration or Displacement	Sweep Rate
Resonance Search	5 – 2000	0.5g	2 oct./min
Low-level sine	5 – 9.3	± 10 mm	2 oct./min
(35% of full level)	9.3 – 120	3.5 g	
Intermediate -level sine	5 – 13.2	± 10 mm	2 oct./min
(70% of full level)	13.2 – 120	7 g	
Full -level sine	5 – 15.8	± 10 mm	2 oct./min
	15.8 – 120	10 g	

Table 6.2 – Test for X and Y axes

The input spectrum is not constant across the frequency range, but it's notched; in Table 6.3 we can see some characteristics of the notched input.

	X axis		Y axis		Z axis	
Excitation type	Frequency range	Lowest level	Frequency range	Lowest level	Frequency range	Lowest level
Low-level sine	35.2 – 120	1	38.1 – 120	1	33.1 – 120	0.6
Intermediate-level sine	34.8 – 120	2.1	38.0 – 120	2	33 – 120	1.2
High-Level sine	35.2-120	3	30-120	2.9	28-120	1.8

Table 6.3 – Notched input

6.1.1 Data analysis

The structure was instrumented with several triaxial sensors and was excited sequentially along all three axes. As a result, the total number of recorded responses (including auto and cross responses) was quite large.

A limited set of responses was selected for analysis, focusing on those that exhibited the most significant shifts in modal frequency and amplitude. This selection was based on plots comparing the transmissibilities obtained under different excitation types.

The selected responses are:

- Sine Z excitation: S4Z, S8Y, S12X
- Sine Y excitation: S15X, S18Y
- Sine X excitation: S14X

For each of these responses, the modal frequency, damping ratio and modal constant were calculated across the four test conditions.

To validate the extracted parameters, the nonlinear transmissibilities were reconstructed for each test type.

6.1.2 Sine Z – S4Z

6.1.2.1 CONCERTO Results

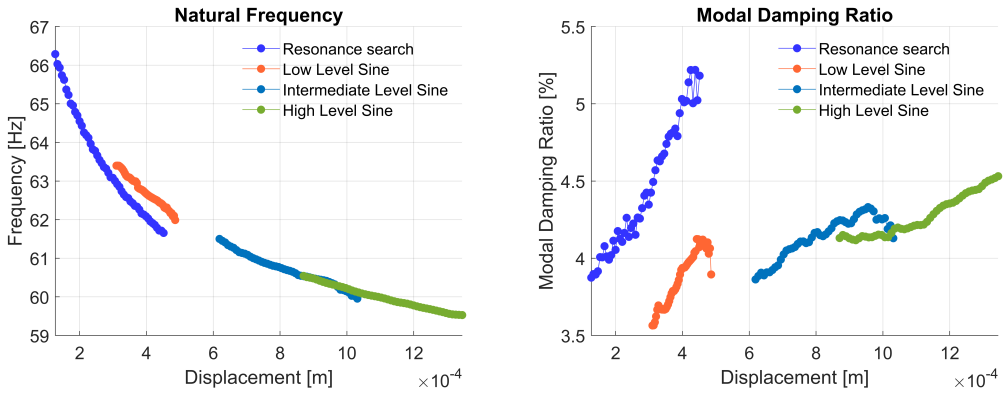

Figure 6.2: S4Z Modal parameters CONCERTO

The natural frequency remains consistent across the four excitation levels. The modal damping ratio is relatively consistent for the three sine excitation levels but shows higher values for the resonance search.

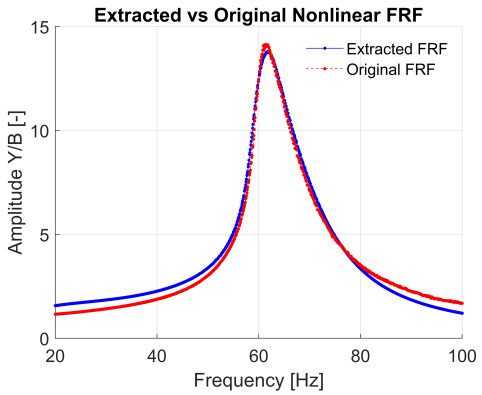

Figure 6.3: S4Z FRFs RS CONCERTO

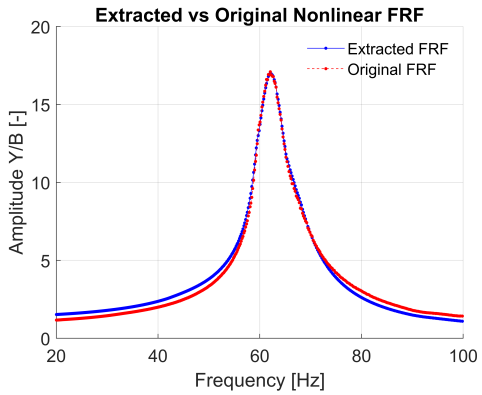

Figure 6.4: S4Z FRFs LL CONCERTO

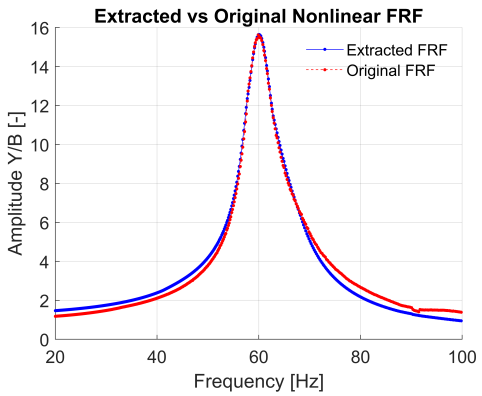

Figure 6.5: S4Z FRFs IL CONCERTO

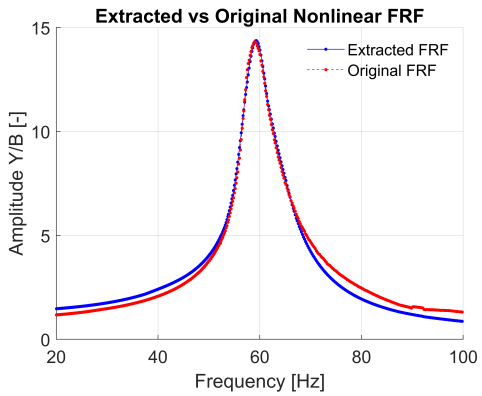

Figure 6.6: S4Z FRFs HL CONCERTO

There is an excellent agreement between the original and the reconstructed nonlinear FRFs across all four excitation levels.

6.1.2.2 Modified Dobson Results

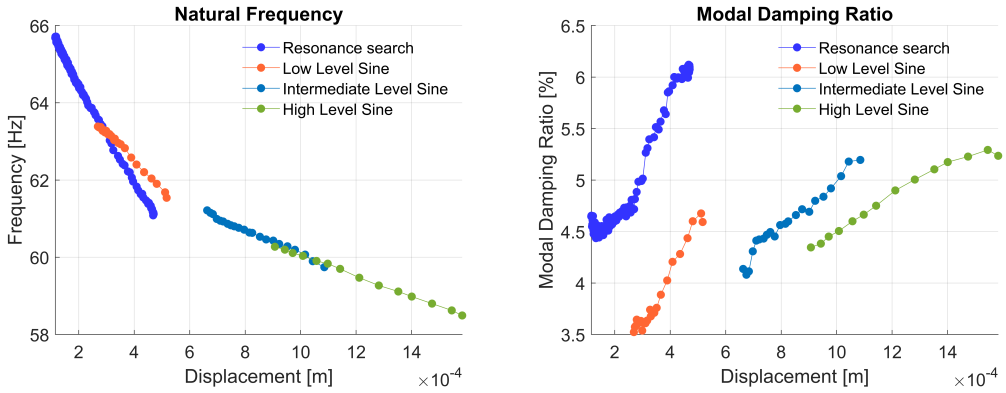

Figure 6.7: S4Z Modal parameters Modified Dobson

The natural frequency remains consistent across the three sine excitation levels but shows a mismatch between the resonance search and the low level sine. The modal damping ratio is relatively consistent for the three sine excitation levels but shows higher values for the resonance search.

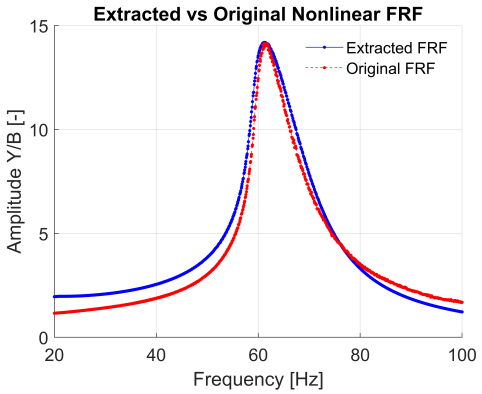

Figure 6.8: S4Z FRFs RS Modified Dobson

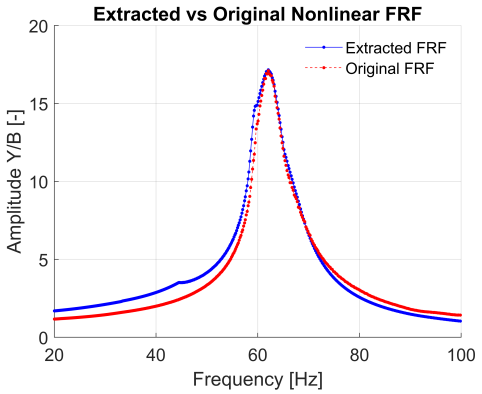

Figure 6.9: S4Z FRFs LL Modified Dobson

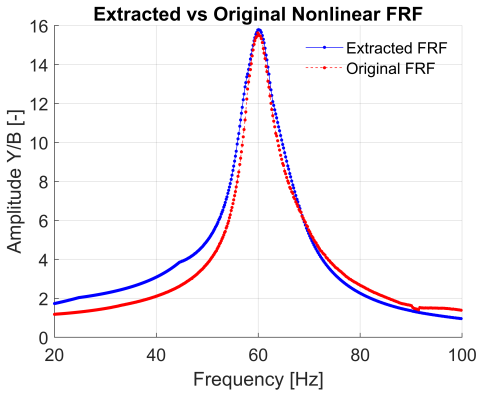

Figure 6.10: S4Z FRFs IL Modified Dobson

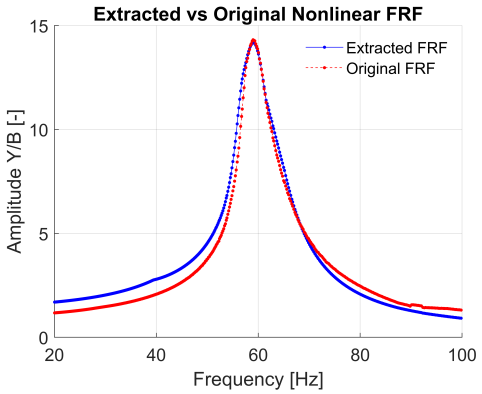

Figure 6.11: S4Z FRFs HL Modified Dobson

There is a strong agreement between the original and the reconstructed nonlinear FRFs across all four excitation levels.

6.1.3 Sine Z – S8Y

6.1.3.1 CONCERTO Results

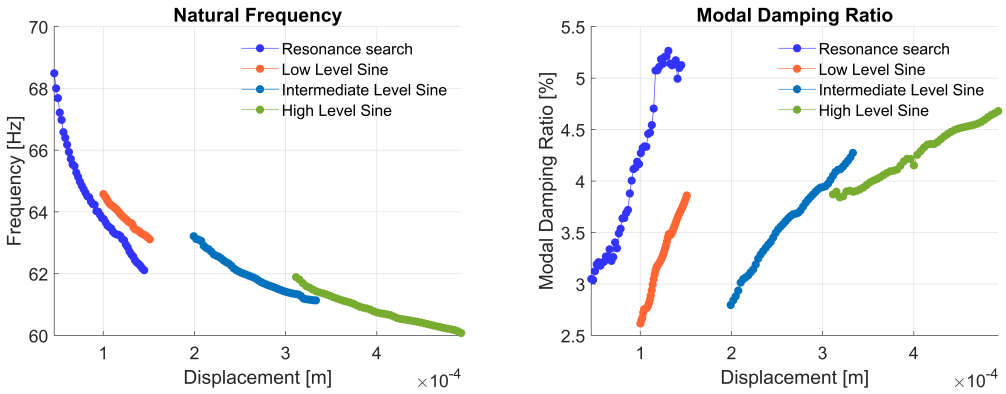

Figure 6.12: S8Y Modal parameters CONCERTO

The natural frequency remains fairly consistent across the three sine excitation levels but shows a mismatch between the resonance search and the low level sine. As for the modal damping ratio, the overall trend appears similar across the different excitation levels, though the slope varies.

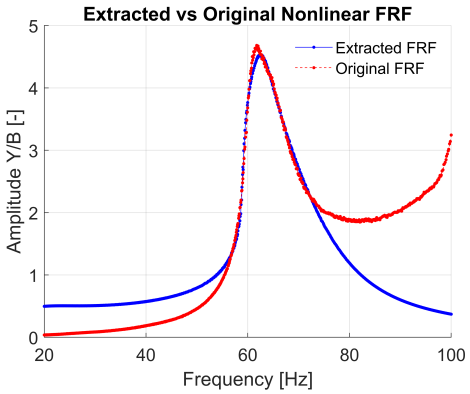

Figure 6.13: S8Y FRFs RS CONCERTO

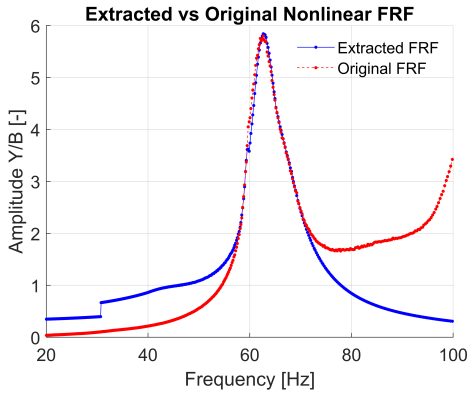

Figure 6.14: S8Y FRFs LL CONCERTO

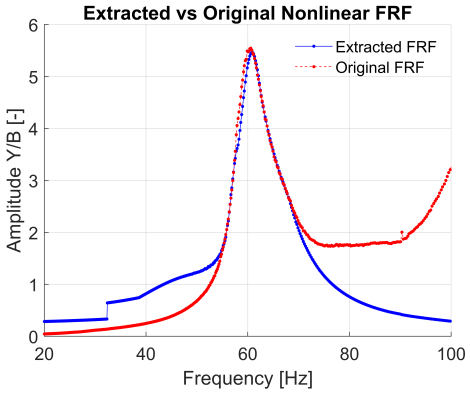

Figure 6.15: S8Y FRFs IL CONCERTO

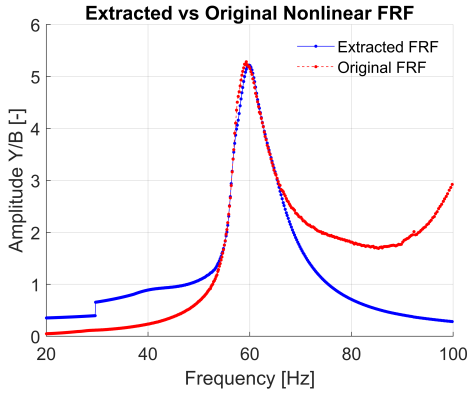

Figure 6.16: S8Y FRFs HL CONCERTO

Near the resonance peak, there is a strong correlation between the original and the reconstructed nonlinear FRFs across all four excitation levels.

6.1.3.2 Modified Dobson Results

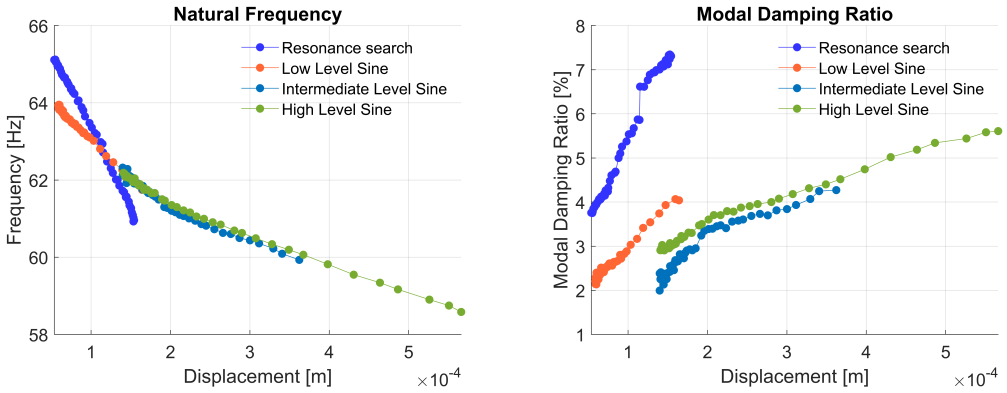

Figure 6.17: S8Y Modal parameters Modified Dobson

The natural frequency remains consistent across the three sine excitation levels but shows a mismatch between the resonance search and the low level sine. The modal damping ratio is relatively consistent for the three sine excitation levels but shows higher values for the resonance search.

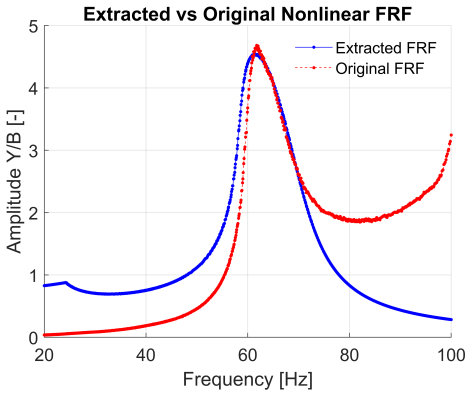

Figure 6.18: S8Y FRFs RS Modified Dobson

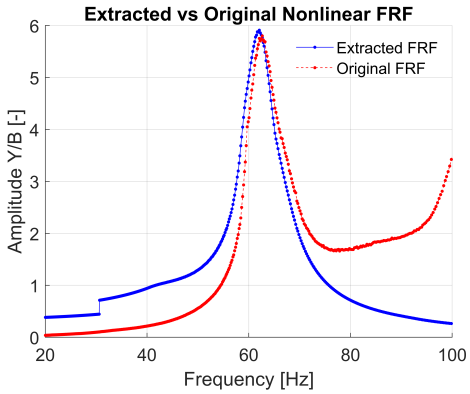

Figure 6.19: S8Y FRFs LL Modified Dobson

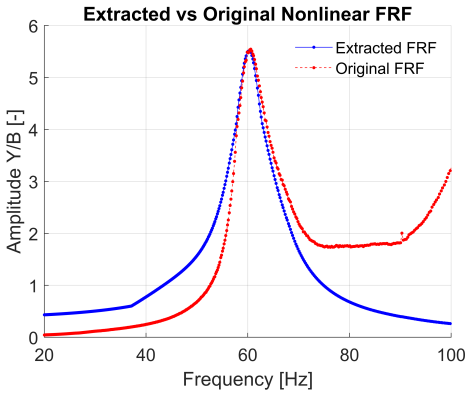

Figure 6.20: S8Y FRFs IL Modified Dobson

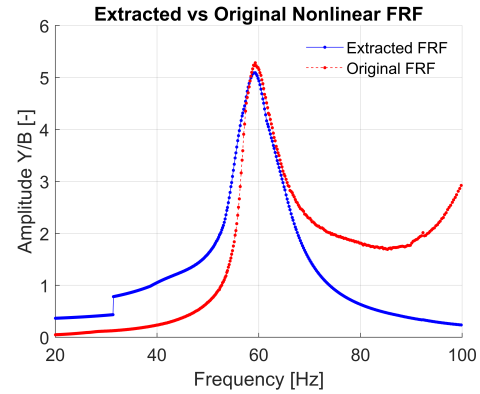

Figure 6.21: S8Y FRFs HL Modified Dobson

Near the resonance peak, there is a fairly good correlation between the original and the reconstructed nonlinear FRFs across all four excitation levels.

6.1.4 Sine Z – S12X

6.1.4.1 CONCERTO Results

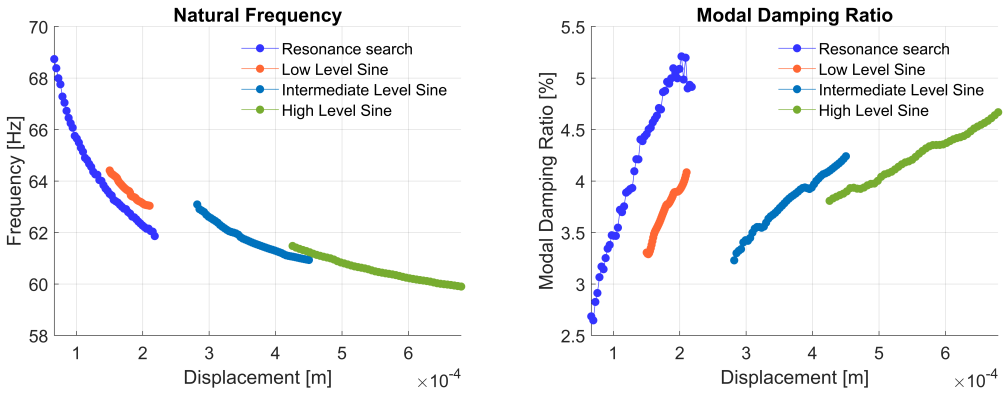

Figure 6.22: S12X Modal parameters CONCERTO

The natural frequency remains consistent across the three sine excitation levels but shows a mismatch between the resonance search and the low level sine. As for the modal damping ratio, the overall trend appears similar across the different excitation levels, though the slope varies.

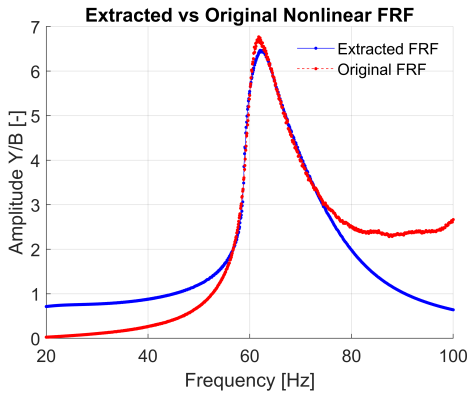

Figure 6.23: S12X FRFs RS CONCERTO

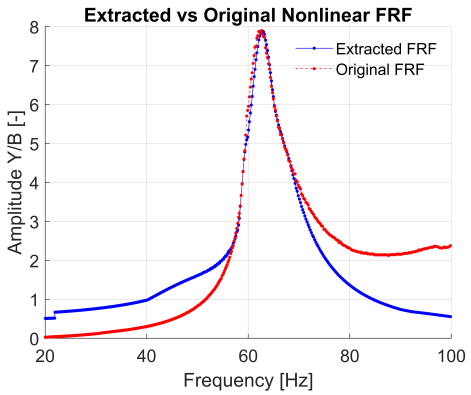

Figure 6.24: S12X FRFs LL CONCERTO

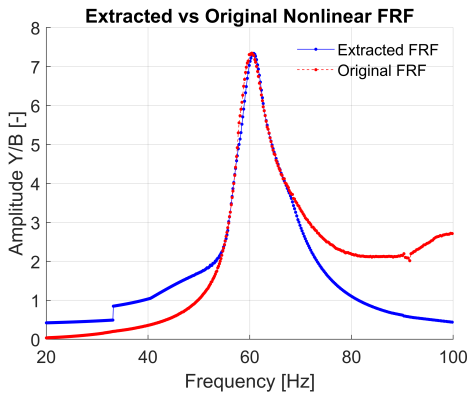

Figure 6.25: S12X FRFs IL CONCERTO

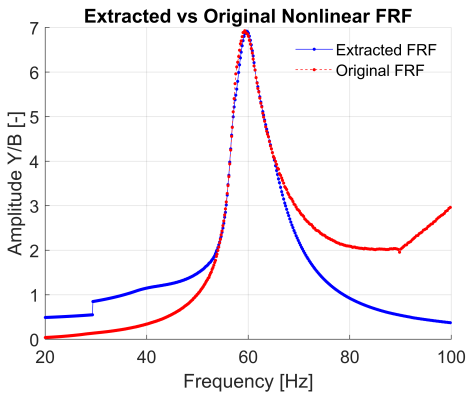

Figure 6.26: S12X FRFs HL CONCERTO

Near the resonance peak, there is a good correlation between the original and the reconstructed nonlinear FRFs across all four excitation levels.

6.1.4.2 Modified Dobson Results

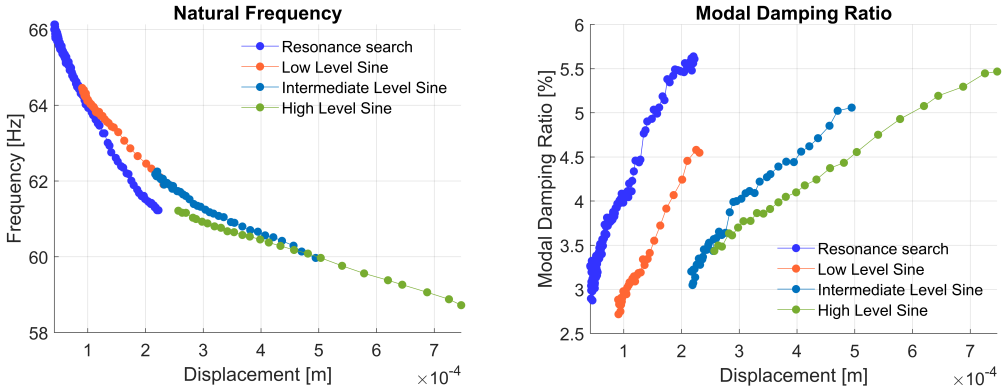

Figure 6.27: S12X Modal parameters Modified Dobson

The natural frequency remains consistent across the three sine excitation levels but shows a mismatch between the resonance search and the low level sine. As for the modal damping ratio, the overall trend appears similar across the different excitation levels, though the slope varies.

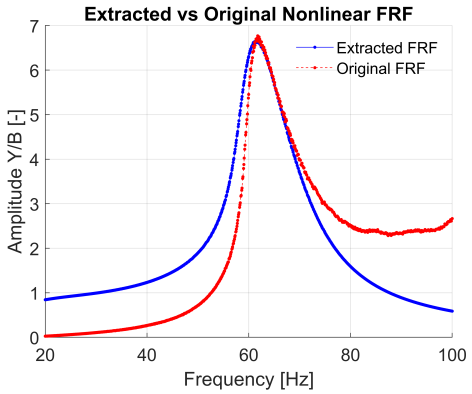

Figure 6.28: S12X FRFs RS Modified Dobson

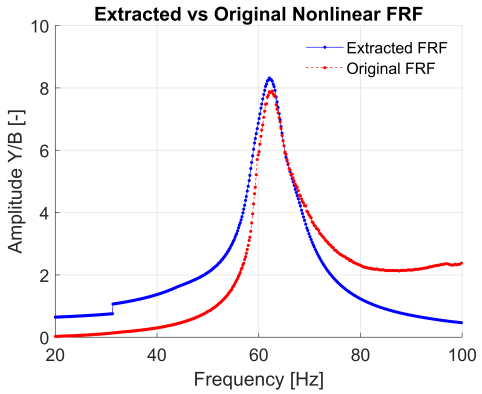

Figure 6.29: S12X FRFs LL Modified Dobson

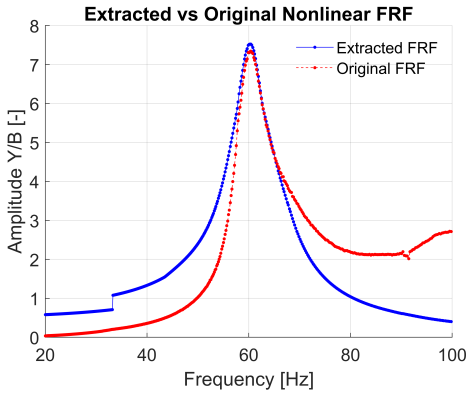

Figure 6.30: S12X FRFs IL Modified Dobson

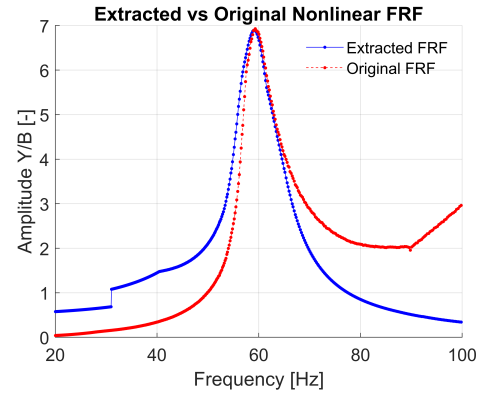

Figure 6.31: S12X FRFs HL Modified Dobson

Near the resonance peak, there is a fairly good correlation between the original and the reconstructed nonlinear FRFs across all four excitation levels.

6.1.5 Sine Y– S15X

6.1.5.1 CONCERTO Results

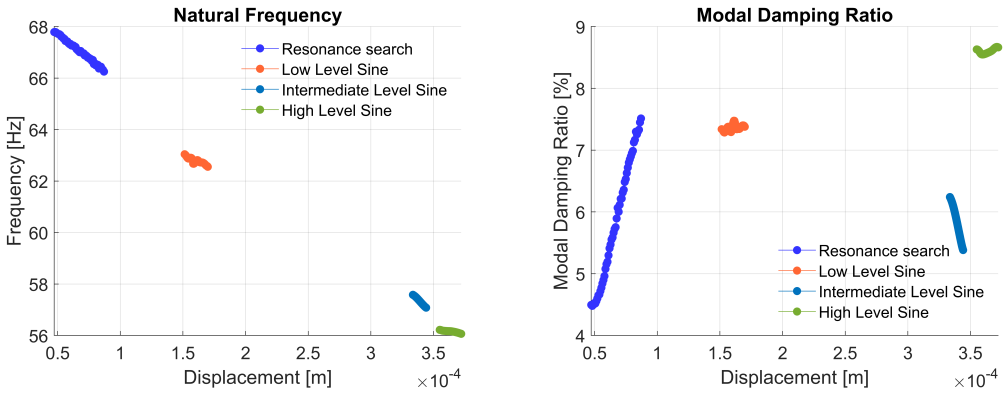

Figure 6.32: S15X Modal parameters CONCERTO

The natural frequency overall trend is quite consistent across the excitation levels. As for the modal damping ratio, no overall trend can be identified.

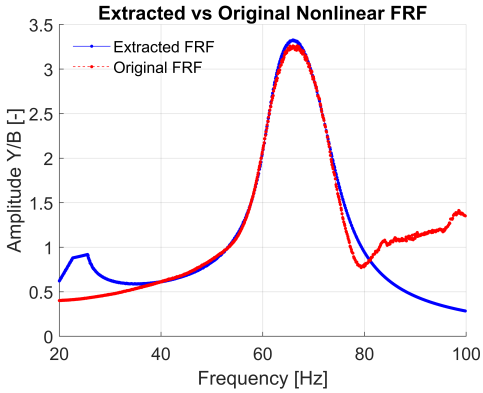

Figure 6.33: S15X FRFs RS CONCERTO

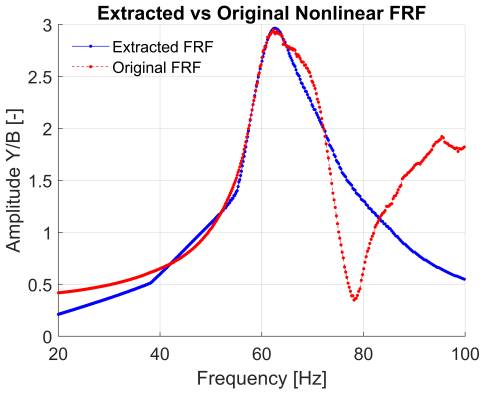

Figure 6.34: S15X FRFs LL CONCERTO

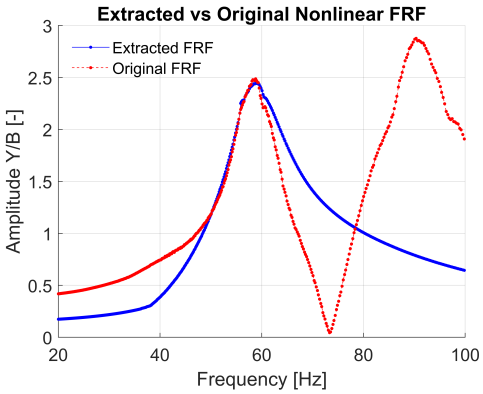

Figure 6.35: S15X FRFs IL CONCERTO

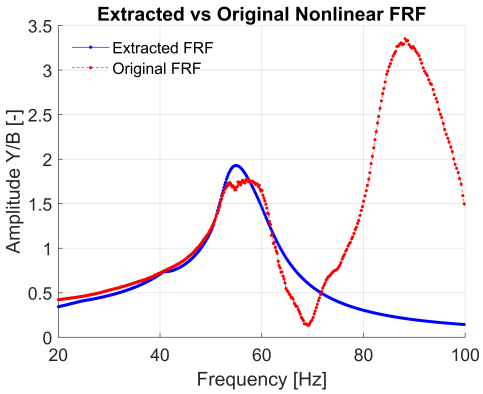

Figure 6.36: S15X FRFs HL CONCERTO

Near the resonance peak, there is a fairly good correlation between the original and the reconstructed nonlinear FRFs across all four excitation levels.

6.1.5.2 Modified Dobson Results

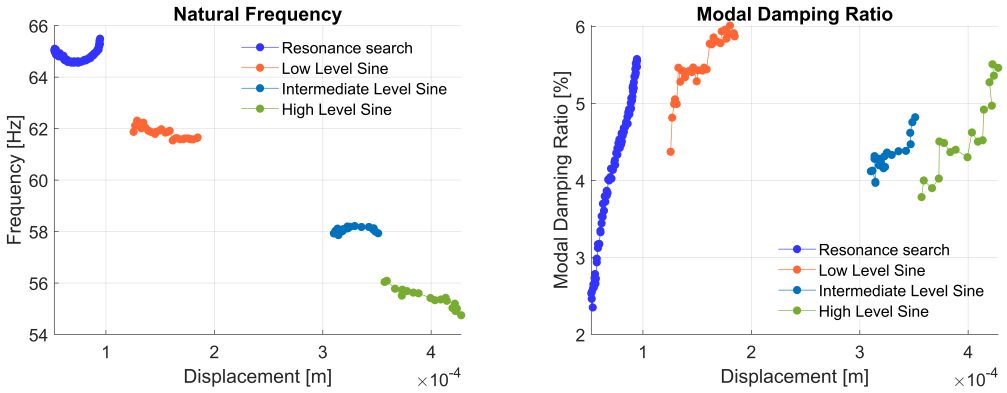

Figure 6.37: S15X Modal parameters Modified Dobson

The natural frequency overall trend is quite consistent across the excitation levels. As for the modal damping ratio, no overall trend can be identified.

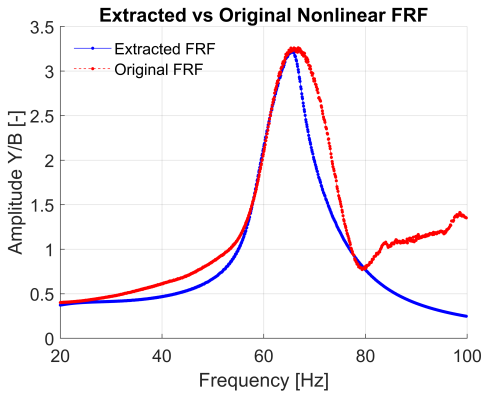

Figure 6.38: S15X FRFs RS Modified Dobson

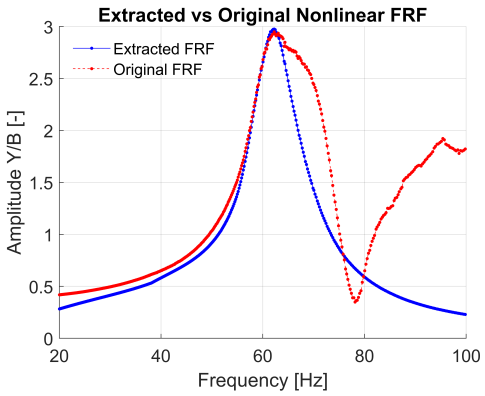

Figure 6.39: S15X FRFs LL Modified Dobson

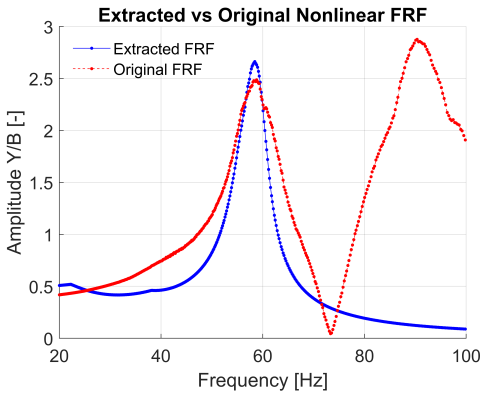

Figure 6.40: S15X FRFs IL Modified Dobson

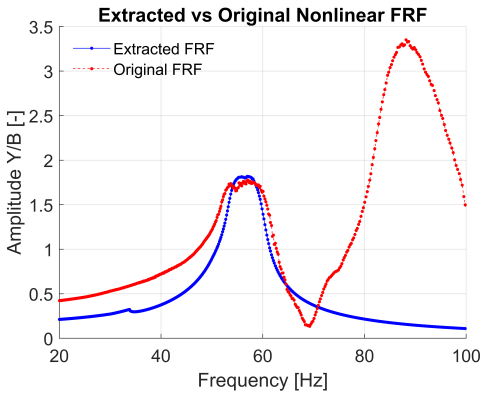

Figure 6.41: S15X FRFs HL Modified Dobson

Near the resonance peak, there is a discrete correlation between the original and the reconstructed nonlinear FRFs across all four excitation levels.

6.1.6 Sine Y– S18Y

6.1.6.1 CONCERTO Results

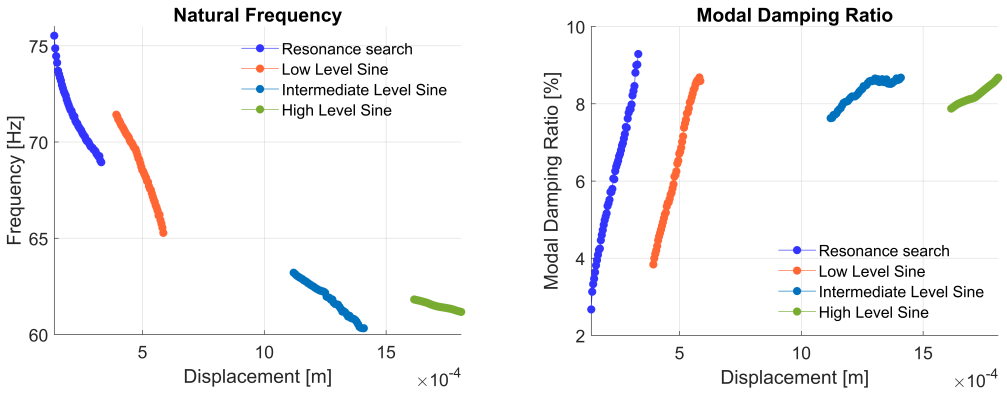

Figure 6.42: S18Y Modal parameters CONCERTO

For the natural frequency and modal damping ratio, the overall trend appears similar across the different excitation levels, though the slope varies.

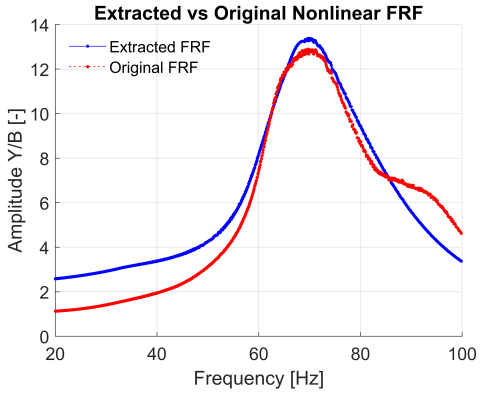

Figure 6.43: S18Y FRFs RS CONCERTO

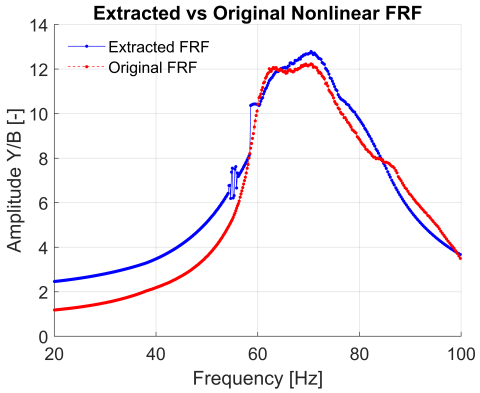

Figure 6.44: S18Y FRFs LL CONCERTO

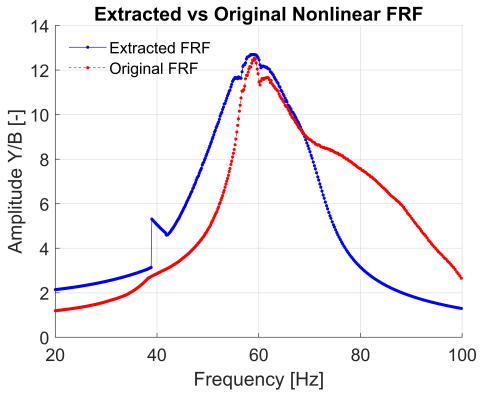

Figure 6.45: S18Y FRFs IL CONCERTO

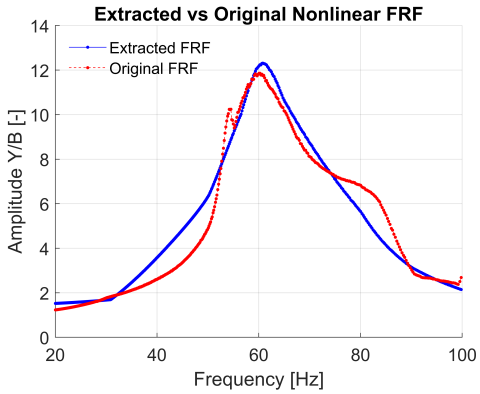

Figure 6.46: S18Y FRFs HL CONCERTO

Near the resonance peak, there is a discrete correlation between the original and the reconstructed nonlinear FRFs across all four excitation levels.

6.1.6.2 Modified Dobson Results

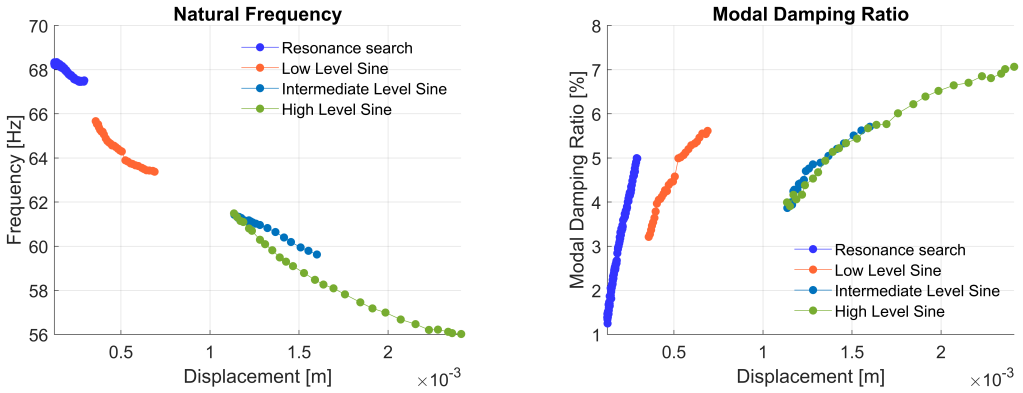

Figure 6.47: S18Y Modal parameters Modified Dobson

The natural frequency remains consistent across the three sine excitation levels but shows a mismatch between the intermediate and high level sine. As for the modal damping ratio, the overall trend appears similar across the different excitation levels, though the slope varies.

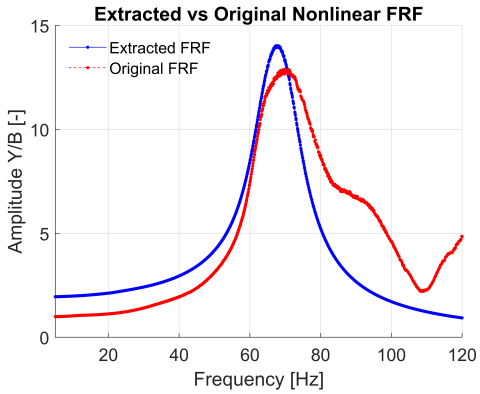

Figure 6.48: S18Y FRFs RS Modified Dobson

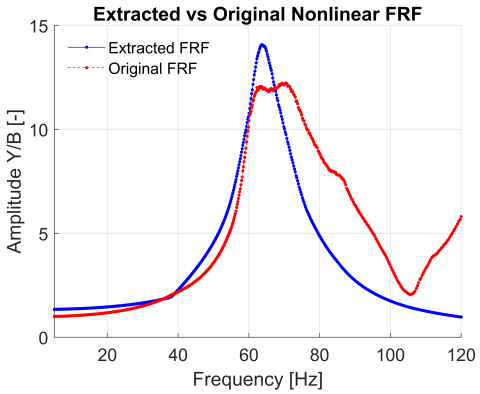

Figure 6.49: S18Y FRFs LL Modified Dobson

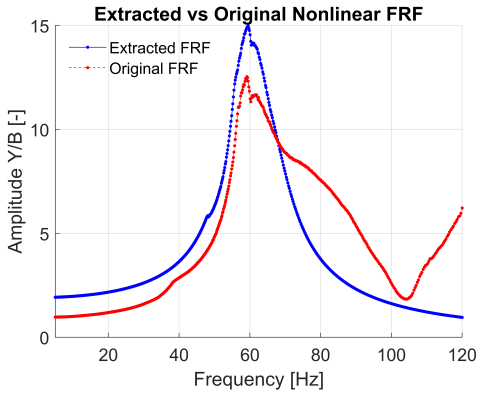

Figure 6.50: S18Y FRFs IL Modified Dobson

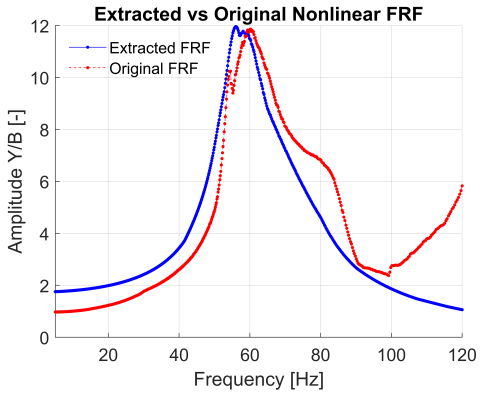

Figure 6.51: S18Y FRFs HL Modified Dobson

Near the resonance peak, there is a discrete correlation between the original and the reconstructed nonlinear FRFs across all four excitation levels, although there is an evident amplitude mismatch for the first three levels.

6.1.7 Sine X– S14X

6.1.7.1 CONCERTO Results

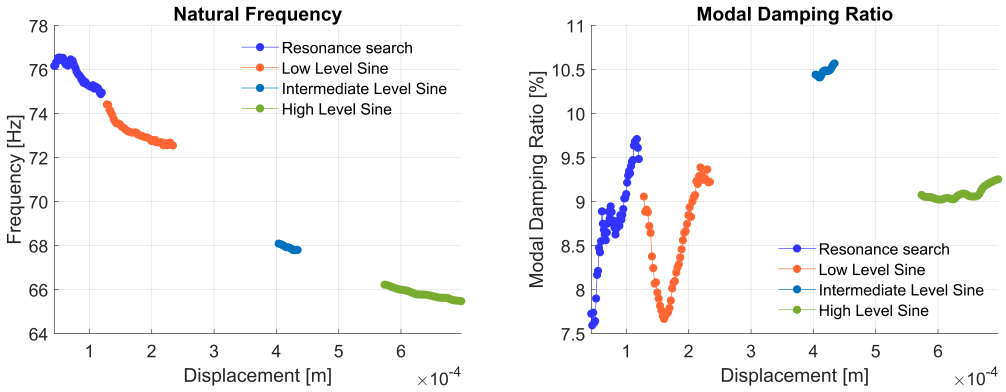

Figure 6.52: S14X Modal parameters CONCERTO

The natural frequency remains consistent across the four sine excitation levels. As for the modal damping ratio, no overall trend can be identified.

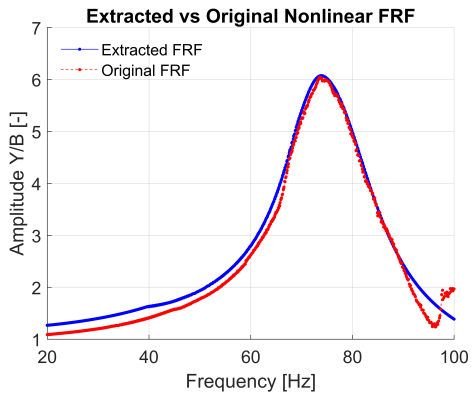

Figure 6.53: S14X FRFs RS CONCERTO

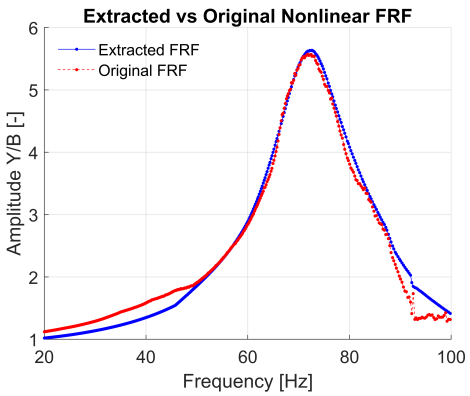

Figure 6.54: S14X FRFs LL CONCERTO

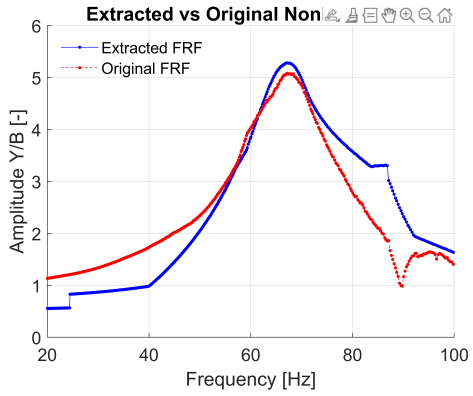

Figure 6.55: S14X FRFs IL CONCERTO

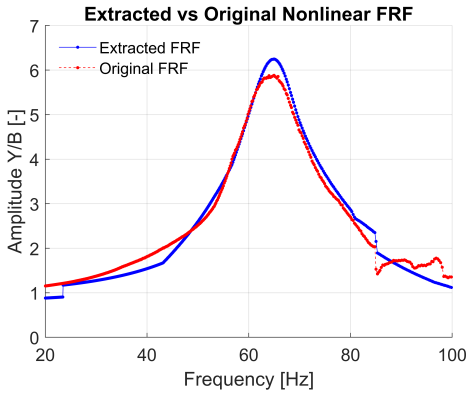

Figure 6.56: S14X FRFs HL CONCERTO

Near the resonance peak, there is a discrete correlation between the original and the reconstructed nonlinear FRFs across all four excitation levels.

6.1.7.2 Modified Dobson Results

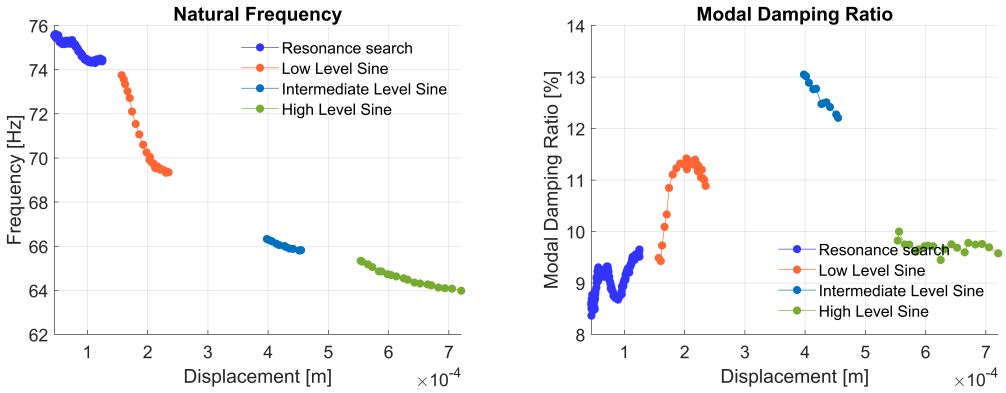

Figure 6.57: S14X Modal parameters Modified Dobson

The natural frequency remains consistent across the four sine excitation levels. As for the modal damping ratio, no overall trend can be identified.

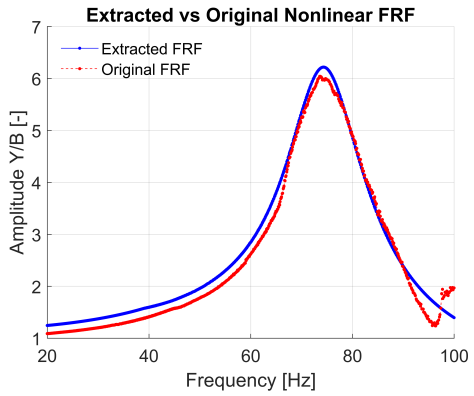

Figure 6.58: S14X FRFs RS Modified Dobson

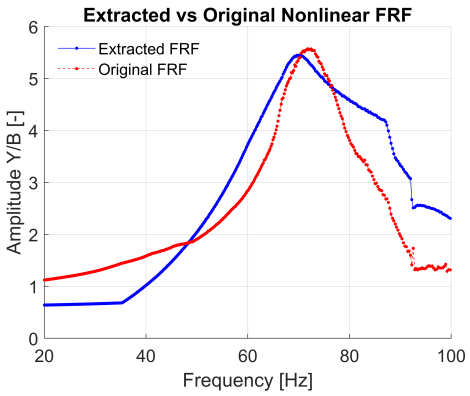

Figure 6.59: S14X FRFs LL Modified Dobson

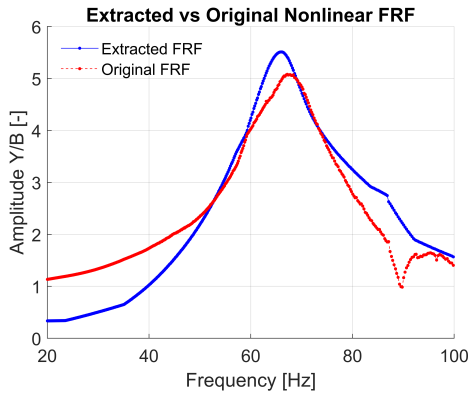

Figure 6.60: S14X FRFs IL Modified Dobson

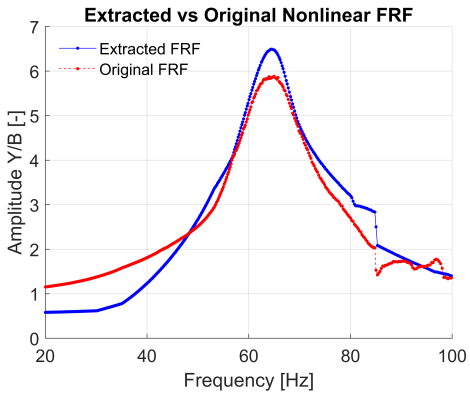

Figure 6.61: S14X FRFs HL Modified Dobson

Near the resonance peak, there is a discrete correlation between the original and the reconstructed nonlinear FRFs across all four excitation levels.

6.2 Comparison between methods

6.2.1 Sine Z – S4Z

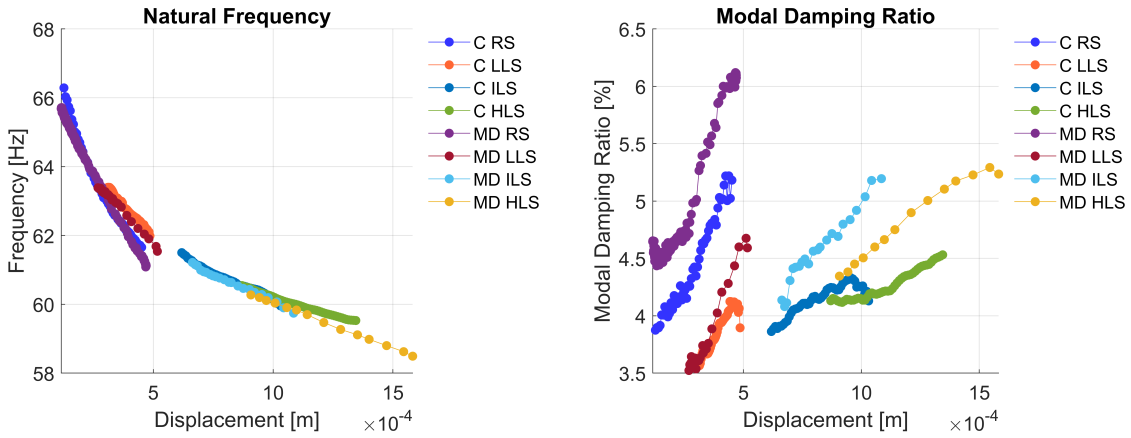

Figure 6.62: S4Z Comparison

The natural frequency is consistent between the two methods. As for the modal damping ratio, it tends to be higher for the Modified Dobson method.

6.2.2 Sine Z – S8Y

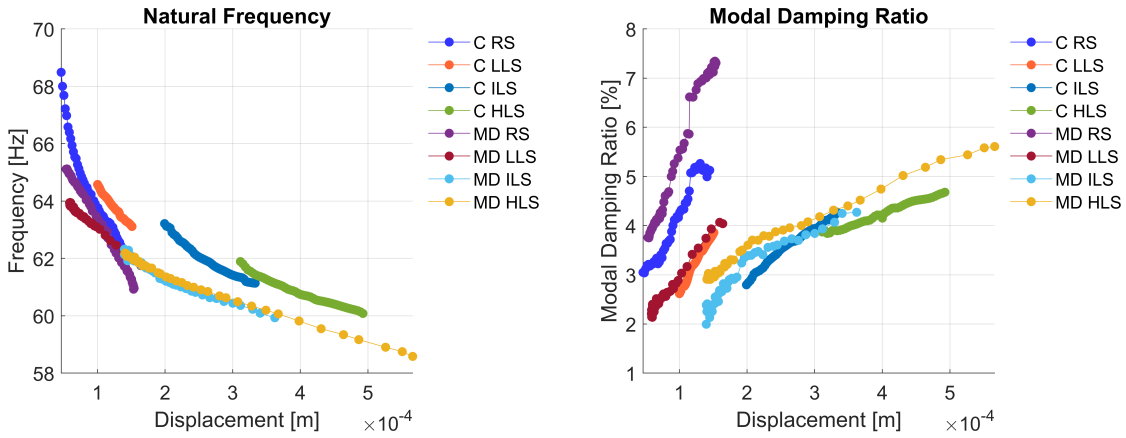

Figure 6.63: S8Y Comparison

The CONCERTO method yielded higher values for the natural frequency. As for the modal damping ratio, it is quite consistent between the two methods.

6.2.3 Sine Z – S12X

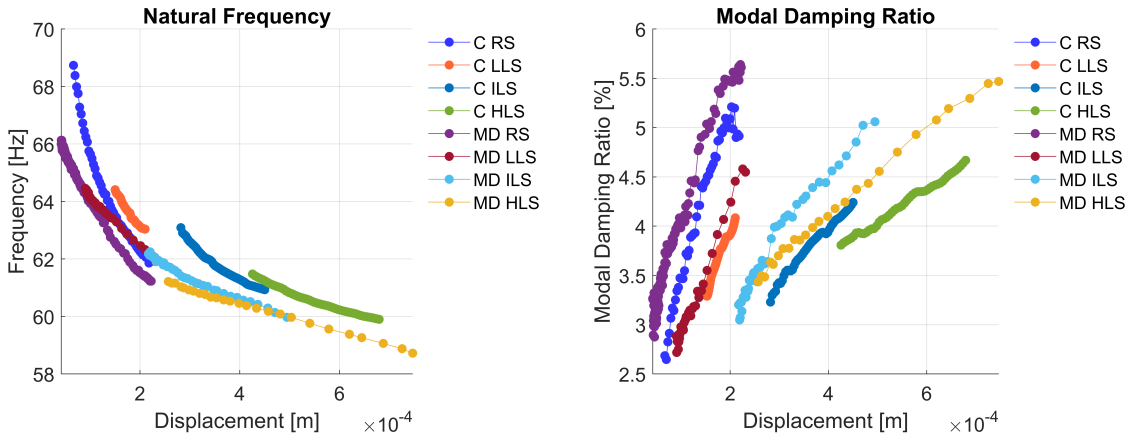

Figure 6.64: S12X Comparison

The natural frequency tends to be higher for the CONCERTO method. As for the modal damping ratio, it is quite consistent between the two methods.

6.2.4 Sine Y – S15X

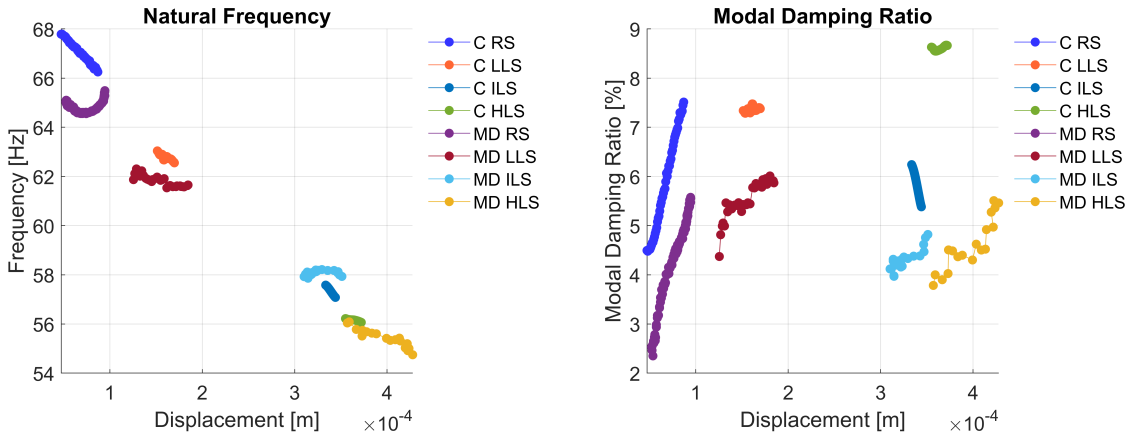

Figure 6.65: S15X Comparison

The natural frequency is quite consistent between the two methods, especially for the higher levels of excitation. As for the modal damping ratio, it is quite different for the two methods.

6.2.5 Sine Y – S18Y

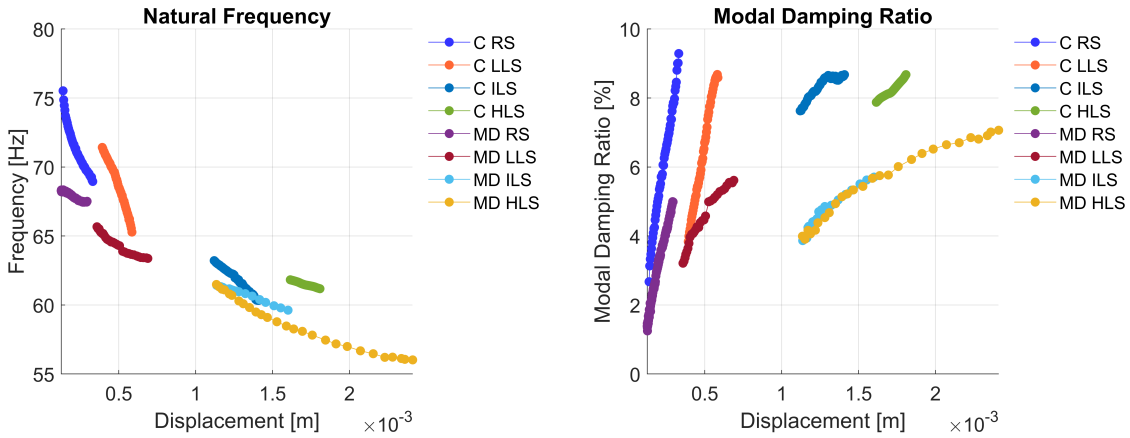

Figure 6.66: S18Y Comparison

The natural frequency and the modal damping ratio both tend to be higher for the CONCERTO method.

6.2.6 Sine X – S14X

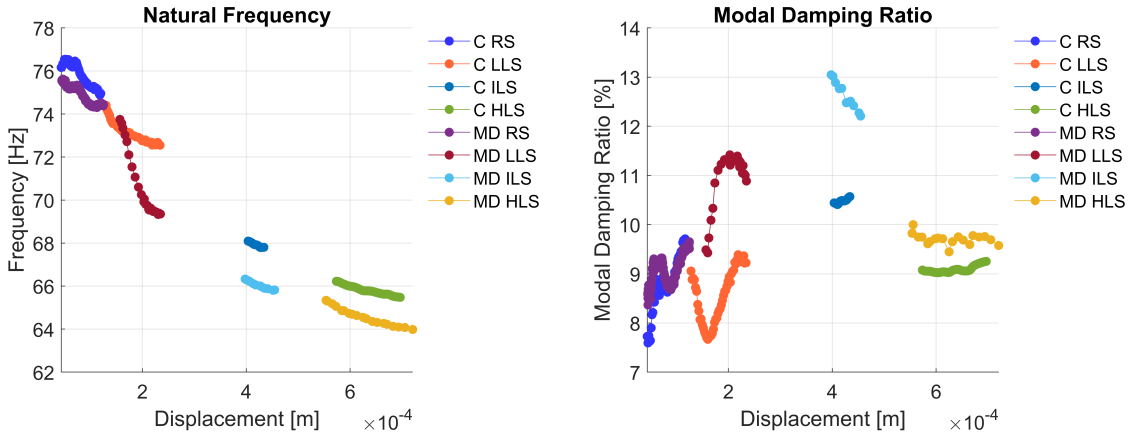

Figure 6.67: S14X Comparison

The natural frequency tends to be higher for the CONCERTO method. As for the modal damping ratio, it tends to be higher for the Modified Dobson method.

7 Frequency and amplitude shift prediction

As discussed in Chapter 2, notching the sine input spectrum at resonance frequencies is crucial to prevent excessive amplification caused by the vibration absorber effect.

To effectively implement this notching strategy, it is beneficial to predict the transmissibility at different excitation levels, as this can provide valuable insight into how the system responds under varying load conditions.

In the following sections, the predictive capability of the proposed methods is evaluated by considering one of the previously analyzed sensors.
The data from each of the four excitation levels were used to estimate the system response at the remaining levels. The four levels considered in the analysis are summarized below:

- Resonance Search (RS)
- Low Level Sine (LL)
- Intermediate Level Sine (IL)
- High Level Sine (HL)

A confusion matrix was employed to assess prediction accuracy. The columns indicate the excitation levels used as input for the prediction, whereas the rows represent the target excitation levels being estimated.

To evaluate the discrepancy between analytical and experimental transmissibilities, the FRF RMS error is used. This parameter quantifies the relative difference between the amplitude levels of two FRFs, one derived from the data extracted and the other from experimental data. It is defined as follows:

$$FRF_{RMS\ Error} = 100 \cdot \sqrt{\frac{1}{N}\sum_{i=1}^{N}\left(\frac{|\alpha_R(i)| - |\alpha_P(i)|}{|\alpha_R(i)|}\right)^2}$$

Where:

- $|\alpha_R(\mathrm{i})|$: amplitude of the measured FRF at the i-th frequency point
- $|\alpha_\mathrm{P}(\mathrm{i})|$: amplitude of the predicted FRF at the i-th frequency point
- N: number of samples used

7.1 Sine Z – S4Z

7.1.1 CONCERTO

The table below shows the confusion matrix results for the selected sensor, obtained when the CONCERTO method is applied.

R \ P	RS	LL	IL	HL
RS	7.78	11.31	17.18	19.08
LL	19.27	15.80	14.81	16.55
IL	15.53	13.41	15.23	13.39
HL	24.24	15.58	15.61	11.98

In general, the elements on the main diagonal tend to have lower error values than the off-diagonal elements. However, this trend is not consistent across all cases. In the plots below, the four extreme cases are shown. It is evident that the errors are generally higher in extrapolation cases compared to interpolation cases.

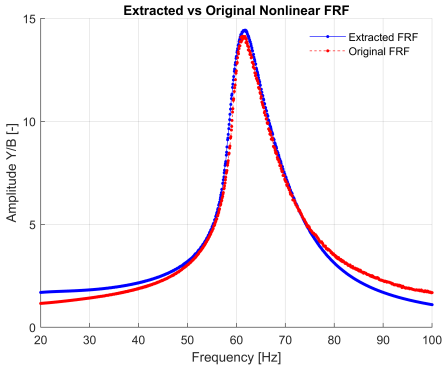

Figure 7.1: CONCERTO – P=1, R=1

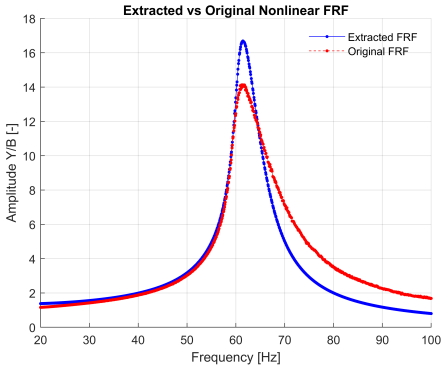

Figure 7.2: CONCERTO – P=4, R=1

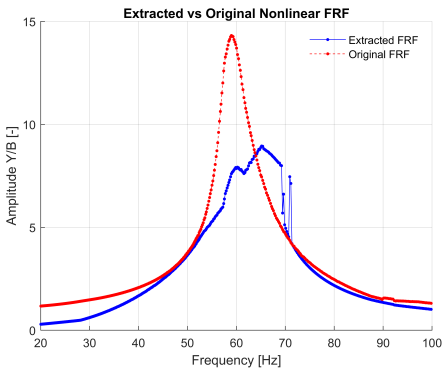

Figure 7.3: CONCERTO – P=1, R=4

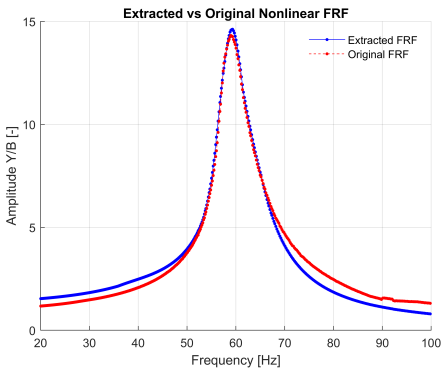

Figure 7.4: CONCERTO – P=4, R=4

7.1.2 Modified Dobson

The table below shows the confusion matrix for the selected sensor when the Modified Dobson method is applied.

R \ P	RS	LL	IL	HL
RS	21.95	20.40	15.33	27.45
LL	19.04	31.36	25.81	22.41
IL	55.26	55.63	29.28	19.22
HL	54.66	77.37	31.91	19.24

In general, the elements on the main diagonal tend to have lower error values than the off-diagonal elements. However, this trend is not consistent across all cases. In the plots below, the four extreme cases are shown. It is evident that the errors are generally higher in extrapolation cases compared to interpolation cases.

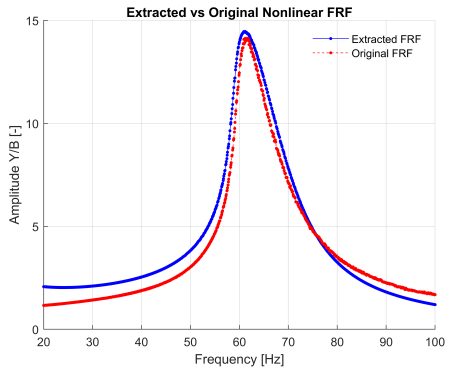

Figure 7.5: Modified Dobson – P=1, R=1

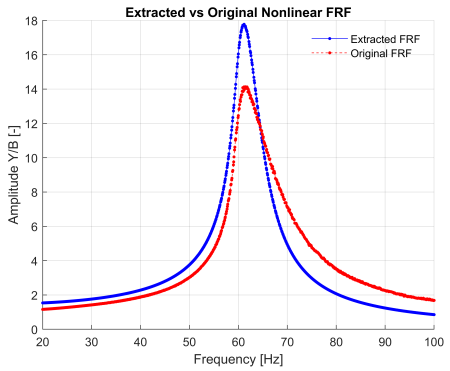

Figure 7.6: Modified Dobson – P=4, R=1

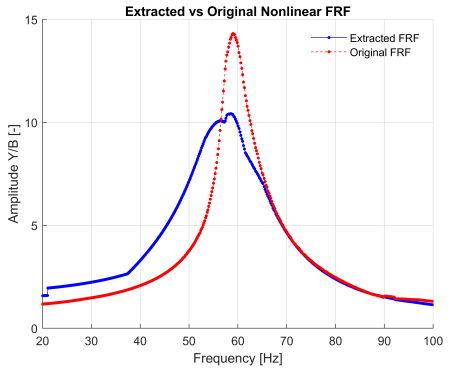

Figure 7.7: Modified Dobson – P=1, R=4

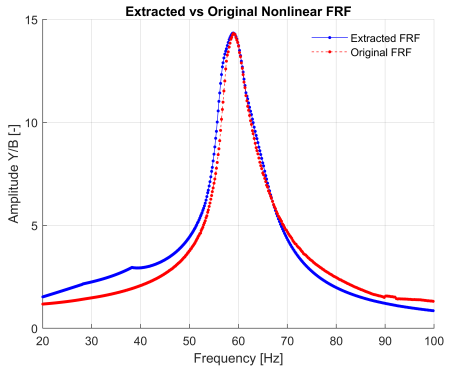

Figure 7.8: Modified Dobson – P=4, R=4

Conclusions

The analysis in this thesis has successfully quantified the influence of nonlinear effects on the dynamic behavior of large deployable antennas, applied directly to test data from the LEOB structure.

A primary result of this work is the detailed characterization of the LEOB's nonlinear dynamics, which demonstrated the structure's clear dependence of its modal parameters on vibration amplitude. The application of the CONCERTO and Modified-Dobson methods enabled the precise measurement of these effects, namely:

- A softening behavior, indicated by a decreasing natural frequency with increasing displacement.
- An increase in modal damping as the response amplitude increases.

The fidelity of this approach was validated by the reconstructed Frequency Response Functions (FRFs), which showed strong agreement with the experimental data, especially in the vicinity of the resonances. This confirms that the single-mode, equivalent linearized models can effectively replicate the system's nonlinear response for given excitation levels.

However, the predictive approach used in this thesis demonstrated significant limitations in accurately forecasting the system's response across different test levels.

Future work should therefore focus on enhancing the ability to predict transmissibilities. A promising path for this would be to implement more advanced methodologies, such as the specific nonlinear Finite Element (FE) model updating techniques detailed by [9]. These methods build upon the general framework of model updating, for which [10] provide a foundational reference, could lead to a more robust predictive capability.

References

[1] B. Duan, Y. Zhang and J. Du, Large Deployable Satellite Antennas - Design Theory, Methods and Applications, Springer, 2020.

[2] L. Ljung, System Identification Theory for the user, Second Edition ed., Prentice Hall, 1999.

[3] K. Worden and G. R. Tomlison, Nonlinearity in Structural Dynamics, Institute of Physics, 2001.

[4] G. Kerschen, "Past, present and future of nonlinear system identification," *Mechanical Systems and Signal Processing,* Vols. 20, Issue 3, pp. 505-592, 2006.

[5] D. J. Ewins, Modal Testing, Research Studies Press, 2000.

[6] D. E. A. Carrella, "Identifying and quantifying structural nonlinearities in engineering applications from measured frequency response functions," *Mechanical Systems and Signal Processing,* vol. 25, pp. 1011-1027, 2011.

[7] A. Carrella, D. J. Ewins and L. Harper, "Using Transmissibility measurements for Nonlinear Identification In: Modal Analysis Topics, Volume 3. Conference Proceedings of the Society for Experimental Mechanics Series," 2011.

[8] D. Di Maio, "A novel analysis method for calculating nonlinear Frequency Response Functions," *Journal of Structural Dynamics,* no. 3, pp. 30-57, 2025.

[9] B. C. Owens, "Nonlinear Finite Element Model Updating Part II: Implementation and Simulation," Albuquerque, 2016.

[10] M. I. Friswell and J. E. Mottershead, Finite element model updating in structural dynamics, Springer, 1995.

[11] E. Standard, ECSS-E-HB-32-26A: Spacecraft mechanical loads analysis handbook, 2013.